Università degli studi "Roma Tre"

Dottorato di Ricerca in Scienze della Materia,
Nanotecnologie e Sistemi Complessi

-

XXX Ciclo

Role of the atmospheric adsorbates in the surface conductivity of hydrogen-terminated diamond

Ph.D. Candidate: *Valerio Serpente*

Tutor: *Alessandro Ruocco*
Co-Tutor: *Stefano Iacobucci*

Coordinator: *Fabio Bruni*

Contents

Introduction

The continuous developments in the production of synthetic diamond, achieved during the twentieth century, have allowed the use of diamond as a material for high technological application. In fact, the combination of its peculiar properties, such as high thermal conductivity, chemical inertness, optical transparency (from UV to IR), high Young's modulus, high support of electric field before breakdown, corrosion resistance and biocompatibility, make diamond a unique material, useful in a variety of different context (such as cutting tool application[1], biosensors[2] and radiation dosimeters[3]).
Among the various properties, one of the most curious and controversial characteristic is the p-type surface conductivity of diamond when it is terminated in hydrogen and successively exposed to air. Actually, the hydrogen termination of diamond, i.e. the saturation of surface bonds with hydrogen atoms, is relatively simple to obtain (it is, for example, a typical feature for synthetic diamond produced with chemical vapour deposition techniques but it is also realizable with specific techniques), as well as the exposure to air is simple and intuitive, so that hydrogen-terminated diamond has been already used for a wide variety of applications, such as, for example, as a p-type semiconducting layer in the metal-semiconductor field effect transistors (MESFETs)[4, 5], for solution-gate field effect transistors (SGFET) used as chemical sensors[6] and in high power/high frequencies electronic devices[7].
Historically, surface conductivity of diamond was discovered at the ends of 1980s but, since in the early years it has been treated as a mere curiosity, the interpretation of this surface conductivity has requested long time and only in 2000[8] it has been partially explained. The mechanism of conductivity is based on two step, involving the negative electron affinity and the surface transfer doping. Differently for other terminations, in fact, the saturation of the surface dangling bonds with hydrogen induces the so-called negative elec-

tron affinity, that is a particular condition in which the minimum of conduction band lies above the vacuum level, favouring the electrons transfer that is then realized by the surface transfer doping: when the lowest unoccupied orbitals of an adsorbate specie lies near the maximum of the valence band of diamond the electron transfer takes place; the successive rearrangement of diamond bands leaves an hole accumulation layer at the surface.
Despite the mechanism of surface conductivity is reasonably clear, more difficulties have been encountered to individuate which molecules, or group of molecules, are responsible of conduction: in this sense few attempts have been done during the years but the conductive species are still unknown. There are evidences that oxygen related species may have a significant role in conduction but the absence in literature of an elemental analysis for the conductive sample prevent any further consideration that can be useful in order to improve both the stability of the adsorbate (conductive) layer and the overall performance of the devices based on hydrogen-terminated diamond.
One critical point in the study of surface conductivity of hydrogenated diamond and, consequently, in the individuation of the conductive species, can be found in the poor effort done to correlate the macroscopic effects, such as the variation of conducibility of diamond upon air exposure or in different temperature/pressure conditions, and the microscopic effects, such as the adsorption/desorption effects or variation in morphology: our approach in that sense is to combine the two aspects, studying at the same time the macroscopic behaviour, using, in particular, resistance measurements, and the microscopic behaviour, where electron spectroscopies such as the X-ray Photoemission spectroscopy (XPS) and the Electron Energy Loss Spectroscopy (EELS) are particularly suited to the task, due to their well known surface sensitivity.
In this framework, we focused our attention on three main aspect that we consider fundamental in the knowledge of hydrogen-terminated diamond:

- the study of sample preparation and how it can affect the surface morphology, and conductive properties;
- the study of surface conductivity of samples and its homogeneity;
- the explanation of the role of oxygen in the conduction mechanism, done through the elemental analysis of the surface.

The work here presented is divided into four Chapters: in the first chapter the main properties of diamond are highlighted, together with a more detailed picture of the mechanism of surface conductivity for the hydrogen terminated diamond; moreover, a detailed description of previous literature concerning spectroscopic measurements is summarized: the works presented are at the basis of our analysis.
Chapter Two is dedicated to the description of theoretical aspects of the spectroscopic technique used for this work of thesis, that are, as said, XPS and EELS. Part of the chapter is dedicated to the description of the experimental apparatuses used in this work.
In Chapter Three the effects of sample preparation on surface order are discussed in terms of the electron diffraction patterns, taken for different prepared sample. The surface order is also discussed after an annealing of the sample, that is the typical method used to desorb the airborne species from the surface. Since in the investigation we used commercially available samples, the variation of their morphology, depending on the quality of the samples used, is then discussed in terms of Atomic-Force Microscopy (AFM) images.
Lastly, the end of Chapter Three is dedicated to the conductive properties of the sample used, investigated with resistance measurements as a function of temperature and pressure and to evaluate the sample homogeneity, studied with an innovative approach that combines resistance and spectroscopic measurements.
Finally, Chapter Four is dedicated to the spectroscopic analysis we performed on our hydrogen-terminated diamond, done with XPS measurements: with the aim to get more information about the adsorbates species on diamond surface and to highlight the role of oxygen in the conduction mechanism, the investigation involved diamond samples in different conductivity states and exposures we will compare exposure to air and to atomic. The second part of the chapter is dedicated to the investigation of C-H stretching mode, with the aim to get more information about the effects of the annealing treatment.

It has to be noted that the contribution of the Ph.D. candidate in this work of thesis concerned, together with the data analysis for the various measurements showed in Chapter Three and Four, also the aspects regarding preparation (discussing and proposing improvement/modification in the preparation

processes), resistance measurements (designing and implementing the four-probe measurements setup and performing measurements) and spectroscopic measurements (designing and implementing the line for introduction and dissociation of oxygen and performing both XPS and EELS measurements).

Chapter 1 Diamond and its properties

Diamond is known to be one of the most precious gemstone from long time: its history began six thousands years ago, when first diamond crystals were extracted from kimberlite in deposits located mainly in India. Today natural diamonds are mined in several places all around the world but principally Africa, South America and Australia.
In the last years diamond has come out of its usual field, jewelery, attracting the attention of researchers because of its unique combination of chemical, physical and mechanical properties, suitable for several application in different fields. Although diamond is well known for its hardness (10^4 g cm^{-2}, known also to be the hardest material in the Mohs scale), there are also other interesting properties[9] such as its high Young modulus, its low coefficient of friction, the exceptional wear resistance (some of the most interesting properties of diamond are presented in Table 1.1) and, moreover, its thermal conductivity, that is the highest of any material known, reaching the value of 2200 W m^{-1} K^{-1} at room temperature, five times better than copper, fifteen times better than silicon: the combination of high thermal conductivity and hardness makes diamond very suitable for cutting tool applications.

For what concern the structural characteristics, diamond is one of the (metastable) allotropic form of carbon: carbon atoms are bonded in a tetrahedral sp^3 configuration where each bond form an angle of 109° with others, arranged in a particular face-centered cubic crystal lattice (also known as diamond lattice) with a base at $(\frac{1}{4},\frac{1}{4},\frac{1}{4})$. The lattice constant for diamond is $a_0 = 3.567$ Å and can depend on impurities concentrations, isotope content[10] and also temperature.
Related to lattice constant, chemical bonds of carbon in diamonds are characterized by a length of 1.57 Å (small if compared with silicon's bond length of

Property	Value
Lattice parameter	3.57 Å
Mechanical hardness	up to 10^4 g cm^{-2}
Dielectric constant	5.7
Thermal conductivity	2200 W m^{-1} K^{-1}
Young Modulus	1143 Gpa
Bandgap	5.45 eV (indirect)
Work function	4.81 eV
Ionization energy	13 eV
Intrinsic electrical resistivity	$> 10^5$ Ω cm
Breakdown electric field	$> 10^7$ V cm^{-1}
Electron mobility	1800 cm^2 V^{-1} s^{-1}
Hole mobility	1200 cm^2 V^{-1} s^{-1}
Optical trasmission	$220 \leq \lambda \leq 2500$ nm; $\lambda \geq 6000$ nm
Atomic number	6

Table 1.1: *Main characteristics of natural diamond [9].*

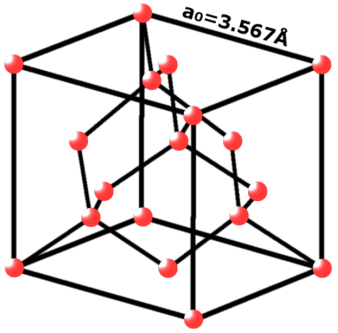

Figure 1.1: *The crystalline lattice of diamond.*

2.34 Å) and a bond energy of 711 KJ mol^{-1}; the atomic density is 1.76×10^{23} atoms cm^{-3}, while diamond's density is 3.52 g cm^{-3}: these parameters are responsible of the above mentioned thermal conductivity and hardness.
Moreover, diamond has interesting properties from the electronic point of view: it is a so-called wide bandgap semiconductor and its bandgap is the wider among all the semiconductors, being an (indirect) gap of 5.45 eV, as sketched in Fig. 1.2: The valence bands in diamond have their maxima at the Gamma point in the Brillouin zone, and the minimum in the first conduction band at k = 0.76 $Å^{-1}$ of the zone boundary in the ⟨001⟩ directions. Finally, the spin-orbit splitting at the maximum of the valence band is particularly small, about 12 meV[1].

One of the consequences of the peculiar wide bandgap is the high support to

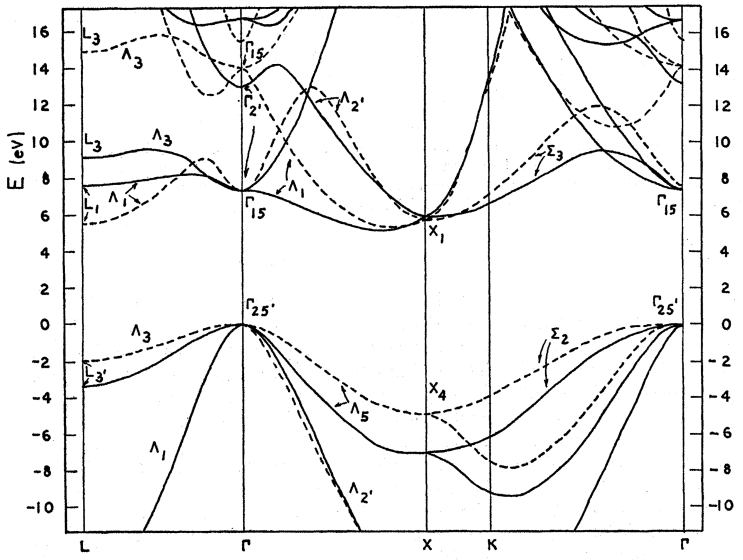

Figure 1.2: *Band structure of diamond, as presented in [11].*

the electric field before breakdown (typical values are around 10 MV cm^{-1}): it was demonstrated that Schottky diodes based on diamond are capable of operating at voltages in excess of 10 kV and at higher temperatures than other semiconductor materials[9]. The combination of thermal and electronic properties makes diamond also interesting for high power electronic device applications.
In order to complete the electronic properties, peculiar characteristics of dia-

mond are the high resistivity (up to $10^{15}\Omega$cm), high carrier mobility of 1800 $cm^2V^{-1}s^{-1}$ for electrons and 1200 $cm^2V^{-1}s^{-1}$ for holes (but for single-crystal synthetic diamond are reported electron and hole mobilities of about 4500 $cm^2V^{-1}s^{-1}$ and 3800 $cm^2V^{-1}s^{-1}$, respectively) and low dielectric constant of 5.7.
Finally, one does not forget the peculiar properties of diamond of chemical inertness and bio-compatibility that, combined with its electronics properties makes it a good candidate for electrochemical and biological applications[12].

For what concern the production of synthetic diamond, the typical methods used are two: the Hot Pressure Hot Temperature (HPHT) that, as the name suggests, replicate the natural condition of diamond production: inside a belt press, capable of producing pressure on the order of 10 GPa and temperatures above 2000°C, is inserted a pyrophyllite container in which graphite is dissolved within molten nickel, cobalt or iron[13]. These metals have the dual purpose of acting both as solvents for graphite and catalysts of the reaction, accelerating the conversion into diamond.
The second method is the Chemical Vapor Deposition (CVD) in which diamond is produced by the deposition of particular chemical species onto a solid surface starting from a gas-phase in non-equilibrium just above the deposition substrate; the non-equilibrium is reached just by activating the species in gas[14]. Different gas mixtures can be used to produce diamond but in case of diamond production they typically include hydrogen: it is well-known, in fact, that atomic hydrogen etches sp^2 graphitic carbon many times faster than sp^3 diamond-like carbon, preventing the deposition of graphite by removing it and favouring the diamond growth. Moreover, the highly reactive hydrogen atoms are used to bond quickly any dangling bond in excess on the surface, leaving the surface of CVD diamond uniformly terminated. The hydrogen surface termination of diamond has non-secondary consequences that will be showed later.

1.1 Classification of diamond

During the years great effort was made to classify diamond, using several experimental techniques. First classification was made during 1930s, when colourless

diamond was divided into two groups, on the basis of difference in transparency in the UV (10-400nm) and infra-red (700nm-1000μm): while one group of diamonds were opaque in UV region and absorbed strongly in the infra-red zone the latter showed high transmittance in UV regions. The two groups were respectively called Type I and Type II diamonds. Later it was discovered that these differences were correlated with the presence of nitrogen impurities (nitrogen is one of the most present impurity in diamond).
Nowadays we have a more detailed classification of diamond (indipendent from the natural or synthetic origin), that, depending on nitrogen impurities is classified into:

- **Type I diamond**: the Type I diamond has nitrogen impurities in concentration over 5 part per million (with typical concentration between 100 and 3000 ppm), enough to be detected by an infra-red spectrometer. On the basis of how nitrogen is aggregated into the carbon lattice Type I diamond can be subdivided into three more sub categories: The most common configuration involves two nitrogen atoms adjacent each other (Type IaA) diamond or rather four nitrogen atoms that symmetrically surround a vacancy (Type IaB diamond). A third configuration (Type Ib diamond) involves isolated single nitrogen atoms that have substituted carbon atoms in the lattice; typically these impurities are called single substitutional.

- **Type II diamond**: in this case the nitrogen impurities are up to 5 parts per million and, hard to recognize from infra-red spectra. Also in this case there are two subcategories: while Type IIa diamond has no other impurities recognizable (making these diamonds *the purest of pures*), type IIb diamond has evident boron inclusion (the other typical impurity in diamond) that are thought to be isolated single atoms that replace carbon atoms.

About the 98% of natural diamond is Type I, while typically synthetic diamond is type IIa; the entire classification of diamond is presented in Fig. 1.3.

1.2 Hydrogen termination in diamond: surface conductivity

As mentioned CVD diamond is naturally terminated with hydrogen, nonetheless the hydrogen termination gives peculiar properties to diamond.

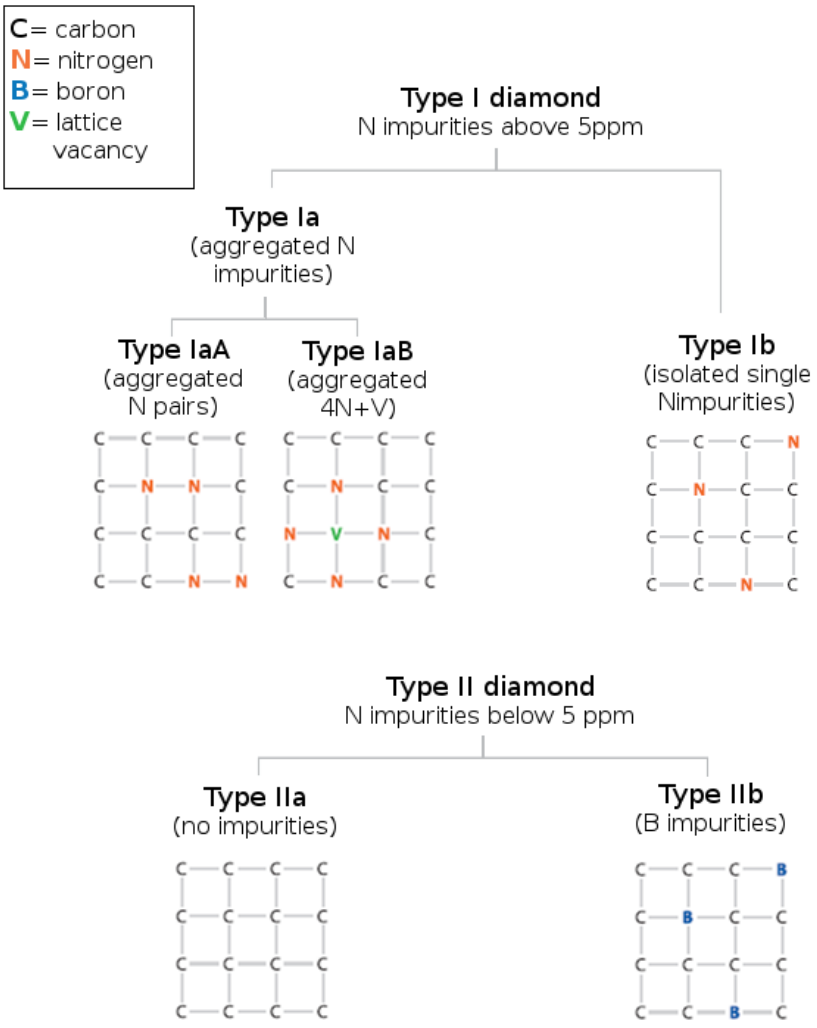

Figure 1.3: *Modern classification of diamond, based on impurity presence.*

For what concern surface arrangement, taking into account the (100) surface as an example, the hydrogen termination of diamond is characterized by single bonds between carbon and hydrogen atoms (in bare surface, instead, dangling bonds are saturated by forming double bonds between carbon atoms). From the energetic point of view, and differently from the other termination of diamonds, one of the most peculiar feature of hydrogen terminated diamond is the negative electron affinity (NEA), that describe the situation in which the conduction band is above the vacuum level; thus, once promoted in the conduction band, electrons do not experience a potential barrier and are free to leave the sample.

The NEA properties of the hydrogen-terminated diamond is crucial in the explanation of the surface conductivity of diamond: first works reporting the surface conductivity in diamond appeared in 1989 when Landstrass and Ravi[15, 16] found an high conductivity for CVD diamond exposed to hydrogen plasma, ten orders of magnitude respect the intrinsic value (10^{-6} versus 10^{-16} $\Omega^{-1}\text{cm}^{-1}$). The conductivity was soon correlated with the hydrogen at the surface or just below, in the subsurface region, with two different experiments by Grot and Gildenblat in 1990 and in 1991[17, 18]: these experiments in fact showed clearly that a mild annealing at 300°C in air or an oxidation of the surface could remove this surface conductivity. These works pointed also out the fact that hydrogen atoms might be implanted for several tens of nanometers into the diamond: this observation is relevant in the interpretation of spectroscopic measurements, shown below.

During the 1990s physical quantities related to the surface conductivity were determined by Hall measurements, pointing out the temperature dependence: sheet conductivity $\sigma_{\square}$ of hydrogen-terminated diamond was measured to be of the order of 10^{-4} to 10^{-5} Ω^{-1} for different sample quality (single-crystal, polycristalline and nanocrystalline) while the areal density of the p-type carriers was found to range between 10^{12} and 10^{13} cm^{-2} and to be hardly temperature dependent between 400 and 120 K[19]. Despite of the great effort made to measure these macroscopic quantities, the microscopic mechanism responsible of the enhanced surface sensitivity of the hydrogen-terminated diamond was still unclear.

In 1996 Shirafugi and Sugino[20], combining XPS and Kelvin-probe measurements suggested the idea of an electron transfer from diamond to surface

acceptors-like surface state with a concomitant band bending at the surface and the subsequent creation of a hole accumulation layer. It was initially assumed that hydrogen itself would form particular, as yet unspecified, acceptor-like defects[19], though the nature of these hydrogen induced acceptors could, not be substantiated. Instead, Ri and colleagues demonstrated that the surface conductivity depends sensitively on the kind of atmosphere in which the diamond sample is kept[21, 22].

Finally, in 2000 Maier and colleagues provided the keystone experiment that revealed the role of hydrogen termination and atmospheric condition and how surface conductivity can be generated[8]. Maier placed a hydrogen-terminated diamond sample (with a surface conductivity of $10^{-4}\Omega^{-1}$) sample in Ultra-High Vacuum (UHV) conditions. One half of diamond was bombarded with electrons in order to remove the hydrogen termination from that side. Then, the two halves of sample were annealed: at this stage also the other half of sample (still hydrogen-terminated) showed no conductance, with values below $10^{-10}\Omega^{-1}$ and no variation until the sample was maintained in UHV conditions. Once the sample was exposed to air the hydrogenated side of the sample rapidly increased its conductance by four orders of magnitude in the first twenty minutes, reaching the saturation value of $2 \times 10^{-5}\ \Omega^{-1}$ in three days. In the same conditions, the non-hydrogenated side of the sample did not show any increase in surface conductance (the comparison is sketched in Fig. 1.4). The conclusion drawn by Maier and colleagues was that hydrogen termination of diamond is a necessary but not sufficient condition to achieve the surface conductivity and that airborne species adsorbed on the surface has a significant importance in conduction.

To explain the mechanism of conduction Maier developed the so-called surface transfer doping model: differently respect to the classical doping, in which dopants are incorporated in the semiconductor lattice, the surface transfer doping takes place when there is exchange of electrons between an intrinsic semiconductor on the one side and an electron acceptor, placed at the other side of the surface, which possesses unoccupied molecular orbitals. In particular, if the energetically lowest unoccupied orbital (LUMO) is close to the valence band maximum (VBM) of the semiconductor, electrons will transfer from the semiconductor to the surface acceptor. As a result negative charges will be localized on the surface acceptors, leaving behind holes in the semiconductor

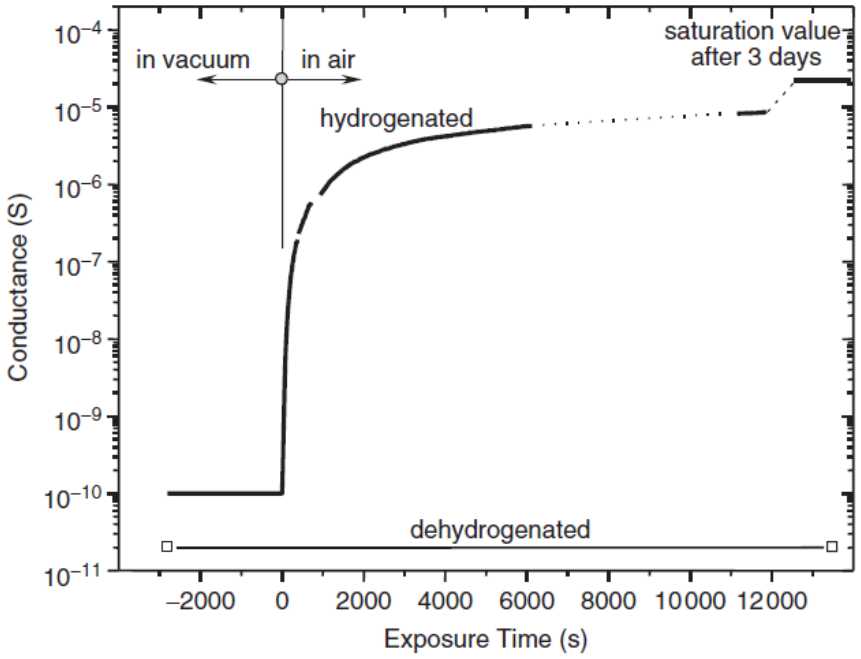

Figure 1.4: *Surface conductance of hydrogenated and non-hydrogenated diamond in ultrahigh vacuum and during exposure to air, as riadapted from [8].*

valence band: the electrostatic potential estabilished by charge separation will confine holes in perpendicular direction, letting them be free to move parallel to surface. This physical charge separation leads to a space-charge layer with associated upward band bending toward diamond surface; at thermodynamic equilibrium the Fermi level of surface adsorbates will be aligned with the Fermi energy of diamond, as presented in Fig. 1.5.

In principle, the surface adsorbate responsible of conductivity in diamond

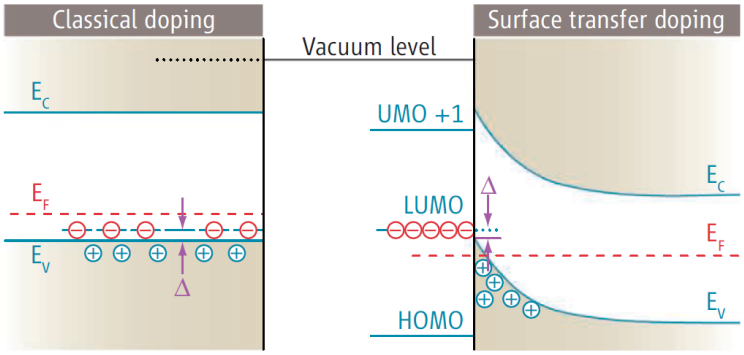

Figure 1.5: *Comparison between classical doping (on the left) and p-type surface transfer doping (on the right), as proposed by Maier and colleagues[8] to explain surface conductivity in hydrogen-terminated diamond.*

can have any form, e.g. can be isolated molecules, solid adsorbates, solvated species, with the only request to have LUMO (acceptor) level near the VBM of diamond. This requirement can be translated in terms of electron affinity: the electron affinity of diamond (1.3 eV) sets the lower limit for the electron affinity of the adsorbated specie, χ_{ad}, to be 4.2 eV ($\chi_{ad} = E_g - 1.3$, where E_g is the energy gap) or higher. Electron affinities of common atmospheric molecules (such ad N_2, O_2, CO_2, H_2O etc.) does not exceed 2.3 eV; for this reason Maier suggested the presence of solvated ions species within a thin aqueous layer as surface acceptors. Among various possibilities, the H_3O^+/H_2 redox couple was proposed by Maier as the electron acceptor because of its chemical potential when referred to the vacuum level, that matches the ionization energy of the perfectly hydrogen-terminated diamond surface (4.2 eV). There is evidence, however, that other redox couples might actually be active when these ideal conditions are not met (such as $O_3/O_2 + OH^-$)[23]. Moreover, there are evidences that oxygen of diamond seems to be very relevant in surface conduction,

as proposed in two different works.
In Kubovic and Kasu's work [24] the hydrogen-terminated diamond was first kept in a N_2 atmosphere and then exposed for one hour to several gases, in particular including high oxidant species such as O_3, NO_2 and SO_2; the hole-sheet concentration (p_s) was measured during the exposition (as showed in Fig. 1.6). While an exposition to main components of air does not change significantly

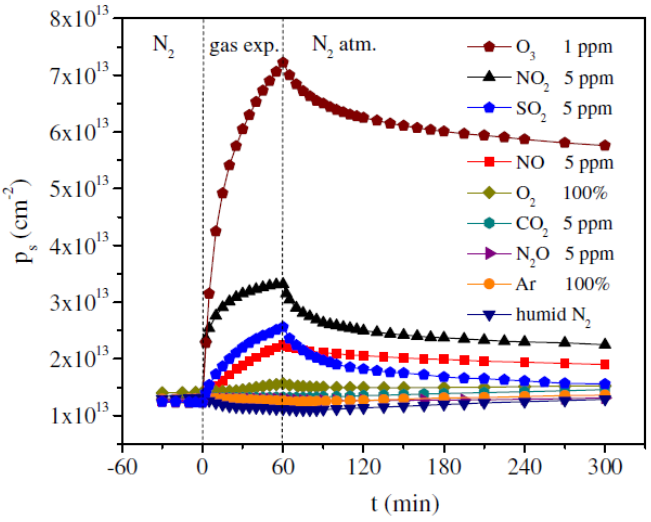

Figure 1.6: *Change of hole sheet concentration during 1h exposure to different gases[24]. Oxidant gases such as ozone, sulphur dioxide and nitrogen dioxide seems to be more effective respect to the other gases.*

(such as carbon dioxide) the hole sheet concentration values, which remained stable around 1×10^{13} cm^{-2}, the exposition to highly oxidizing species, such as sulfur dioxide, nitrogen dioxide and in particular to ozone, seems to increase several times (up to 7×10^{13} cm^{-2}) the hole sheet concentration. This work was then extended by H. Sato [25], measuring the time evolution of both hole-sheet concentration and mobility for the specific O_3 and NO_2 cases. In this case, the hole sheet concentration was monitored during desorption in vacuum after exposion of 1ppm NO_2 and O_3. As can be seen in Fig. 1.7, after 240h of desorption the slowly decreasing of p_s for the two gases is almost the same, clearly suggesting that remaining adsorbed species on diamond surface had to be the same for both two gases and that the species should be composed of oxygen, which is the unique common element. To explain this behaviour, Sato

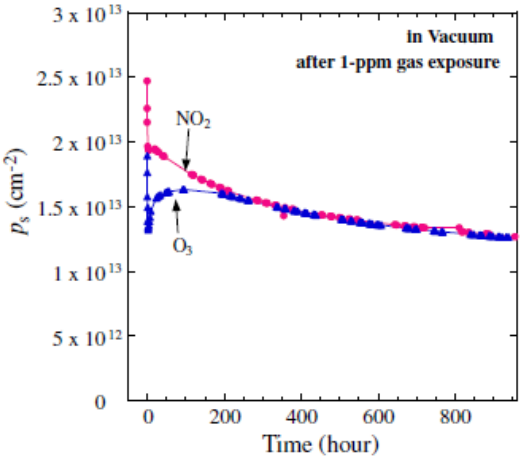

Figure 1.7: *Evolution of hole sheet concentration during desorption, after exposure to NO_2 and O_3. After 240 h of desorption the behavior of p_s is the same[25].*

proposed an alternative mechanism of adsorption respect to Maier, with no presence of a wetting layer (Fig. 1.8).
Taking as example NO_2, molecules steal electrons from the diamond, so the NO_2 molecules are negatively ionized while positive holes are left on the diamond surface; thus the positive holes in diamond are spatially separated from negatively-ionized NO_2 molecules. Soon, extra NO_2 molecules on the surface start to migrate until the surface coverage of NO_2 molecules on the H-terminated surface reaches the monolayer coverage and the the adsorption of NO_2 molecules stops. In this state, the time evolution of p_s shows a saturating behavior.

Regarding the desorption, Sato has been proposed that proceeds in two steps: as mentioned before the similar behaviour in the hole sheet concentration for both NO_2 and O_3 suggests that O_2 molecules are the residual adsorbed species, because it is the unique common element between the two gases. Sato proposed that first step of the process could be the decomposition of NO_2 into O_2 and N_2 with the latter molecules that desorb into the vapour phase and negatively ionized O_2 molecules are left on the H-terminated surface. Then the second step is the slow desorption of O_2 molecules from the surface due to the recombination of the O_2 ions and the holes in the diamond, because the recombination requires tunnelling of electrons from the O_2 ions to the diamond

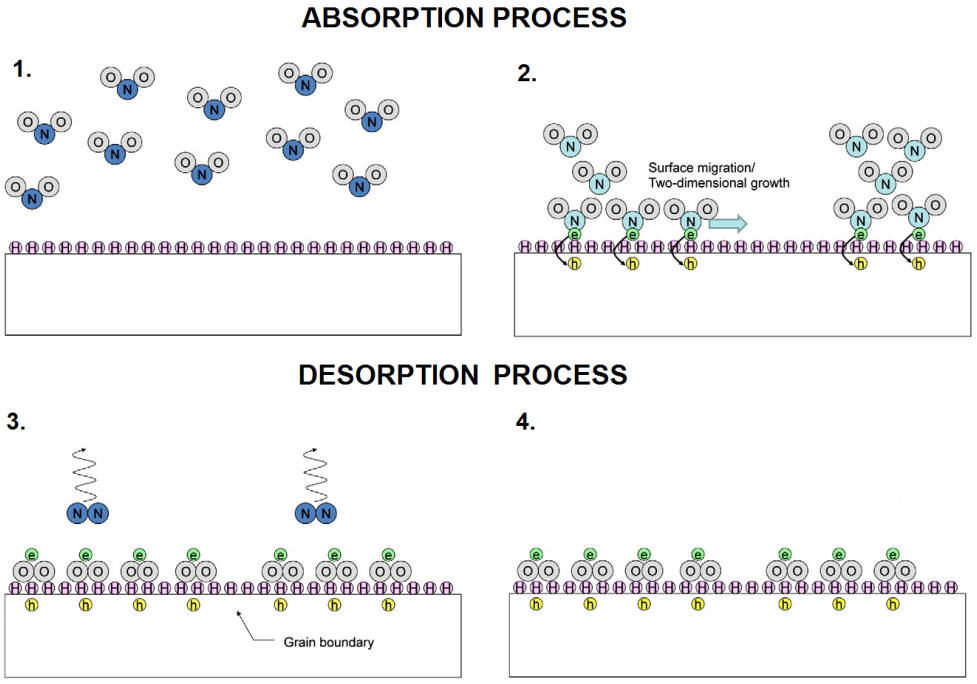

Figure 1.8: *Proposed model of N_2O absorption and desorption on hydrogen-terminated diamond. Picture readapted from[25].*

lattice with a time scale of weeks, making this surface stable for weeks.
Both the possible presence of a wet layer, with the particular reaction proposed by Maier and coworkers, and the role of oxygen in the mechanism of conduction in hydrogen-terminated diamond, as proposed by Sato and coworkers, still remain unclear (and not fully verified), thus still under investigation.

1.3 Spectroscopic measurements on hydrogen-terminated diamond

A typical issue opened in the years of investigation on hydrogen-terminated diamond is the poor effort made to combine measurements concerning macroscopic aspect, as the electric measurements do, and microscopic aspect on the sample, well studied by spectroscopic analysis. These, although present in literature, rarely come into contact with their macroscopic counterpart and only in few cases electrical and spectroscopic measurements are performed together[24]. We believe instead that the combination of the two type of measurements can clarify the questions opened during these years of study on the hydrogen-terminated diamond.
In this section we are going to discuss previous spectroscopic measurements performed on hydrogen-terminated diamond, focusing mainly on three techniques: Low Energy Electron Diffraction (LEED), X-Ray Photoemission Spectroscopy (XPS) and Electron Energy Loss Spectroscopy (EELS). These techniques, in fact, give complementary information on the microscopic behaviour of the samples. As said in the precedent section, hydrogen-terminated surface and bare surface of diamond are characterized by different bond configuration. This, in principle does not affect LEED patterns taken for the two termination: taking into account the (100) surfaces, in fact, the two termination are both characterized by a 2×1 reconstruction of the surface. Instead, oxygen-terminated (100) diamond surface are characterized by a 1×1 reconstruction[26] (the three LEED patterns are showed in Fig.1.9). Air exposure of the hydrogen-terminated samples does not affect LEED patterns[27], while roughness can be effective to induce different reconstruction[28].

EELS measurements can complete LEED information because of its surface sensitivity: actually we can divide the EELS measurements as such, where typical features studied are interband transition or plasmon losses, from the vibra-

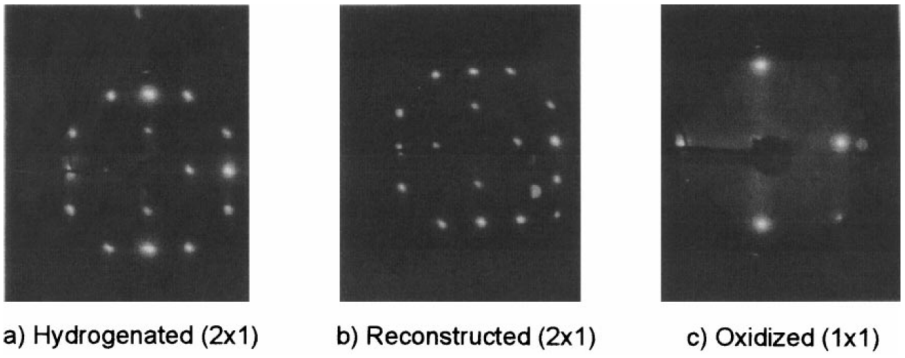

Figure 1.9: *LEED pattern for (a) hydrogenated (b) reconstructed (c) oxidized C(100) surface. Picture taken from[26].*

tional contribute, typical studied with the so-called High Resolution Energy Loss (HREELS). The Energy Loss spectrum of diamond has typical feature (Fig.1.10) at 14 eV (due to an interband transition from valence to conduction band[29]), at 23 (surface plasmon loss) and 33 eV (bulk plasmon loss)[29, 30]. In some cases a bump at 6.5 eV has been observed, and it has been related to the $\pi\pi^*$ transition for samples that have graphitic residuals, while a structure at 10 eV is typically associated to the presence of Oxygen on surface[30].

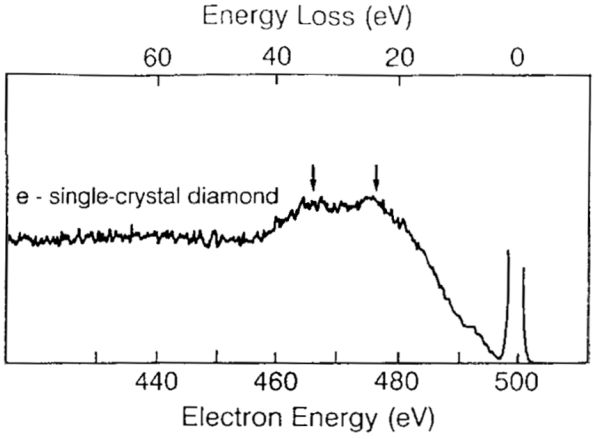

Figure 1.10: *EELS spectrum for single crystal diamond. Typical plasmon structures of diamond at 23 and 33 eV are clarly visible. Picture riadapted from [30].*

More interesting, from the point of view of surface termination, is the loss region between 0 and 5 eV (Fig. 1.11). In bare diamond samples this region is characterized by the presence of a large feature, starting roughly at 2eV of energy loss, that has been related to a surface fully terminated with C=C dimers, as the (100) surface is[26]. This feature is removed with hydrogen-termination of the surface, thus the 0-5 ev loss region for the hydrogenated diamond samples is characterized by the presence of a gap. In some papers the presence of dangling bond has been related to the presence of a background contribute in the 0-5 eV region[30].

Even in the study of vibrational mode it is possible to find structures related

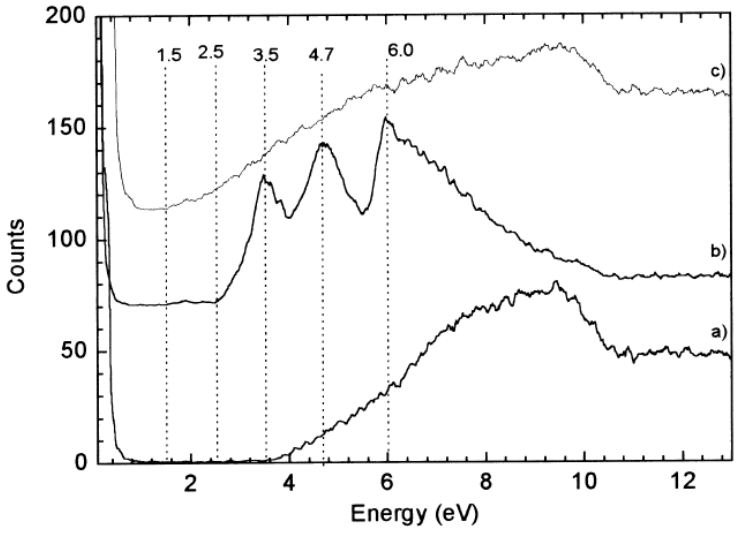

Figure 1.11: *Energy loss spectra for (a) hydrogenated (b) oxidized (c) reconstructed C(100) surface in the 0-12eV loss region[26].*

to the surface termination. For the hydrogen-terminated samples, benchmark features are located at 1220 cm^{-1}(0.302 eV), with repetition at 2440(0.302) and 3660(0.446) cm^{-1}(eV), that have been attributed to a mix of δ(C-H) and ν(C-C) lattice vibrations and their first and second overtones, while a feature at 2920(0.360) cm^{-1}(eV) is attributed to ν(C-H) stretching mode[31] (a typical HREELS spectrum is presented in Fig.1.12); oxidation of the surface can induce additional features at 970 (0.120), 1570(0.194), 1765(0.218) and 3540(0.438)cm^{-1}(eV), attributed respectively to ν(C–O–C) and δ(O–H), to quinone ν(C=O) or ν(C=C) mode, to the carbonyl stretch and to ν(O–H)[26].

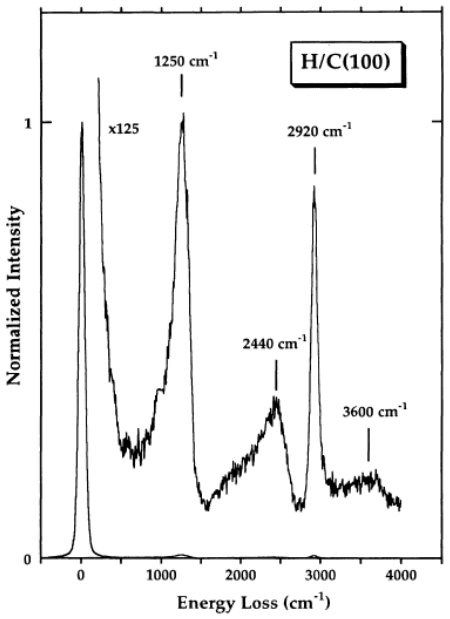

Figure 1.12: *typical HREELS spectrum for (100) surface of hydrogen terminated diamond. Picture taken from [31].*

In principle it is possible to determine the angle of C-H bond respect to the surface but, as suggested by Thoms and Butler[31], studying the evolution of intensity of elastic peak and of 1250, 2449 and 2920 cm^{-1} loss peaks as a function of collection angle in off-specular condition, within the frame of the dipole approximation for the quasi-elastic scattering [32]. However, a significative contribution of impact scattering, can affect the study of these losses, even for smooth surfaces and, moreover, in specular condition.

Finally, the XPS technique has been devoted mainly on the study of C1s core level for hydrogen-terminated sample. Historically, first measurements on hydrogen-terminated diamond and relative deconvolution were performed on (111) surface [33–35] and then on (100) surface[36]. In both the two surfaces C1s core-level showed, in addition to the dominant bulk C 1s line, some tailing toward higher binding energy, interpreted in different in different ways as one or more separate components[33]. A resolutive experiment, able to explain explain with more detail this bump at high binding energy, was performed by Graupner and coworkers[37]. Using two different hydrogen-terminated sam-

ples, characterized by different surface orientations (respectively, (100) and the (111) orientation), Graupner studied samples using two different photon energies, 305 and 325eV, in order to enhance bulk and surface behaviour, respectively.

The samples were first studied after a hydrogen-plasma treatment and the deconvolution of C1s spectra showed clearly the presence of two components: the two components are called respectively S_A and B in Fig. 1.13 and the shift between the two components was different for the two surfaces: +0.5 eV for the (100) and +0.7 eV for (111) surfaces;.

The contribution of S_A component relative to the total C1s emission increases

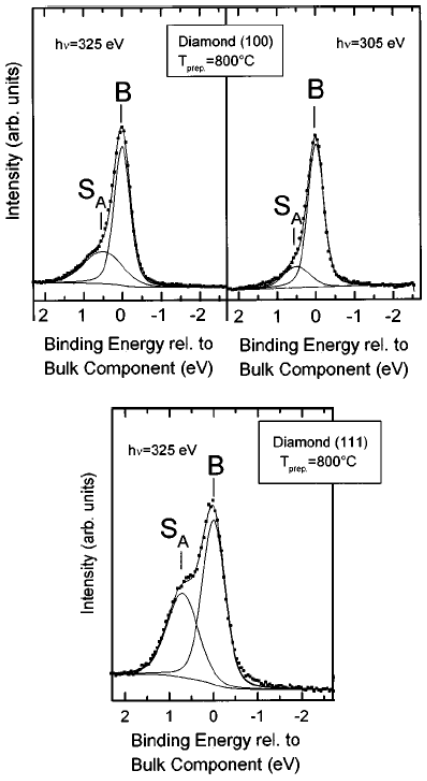

Figure 1.13: *C1s photoemission spectra for (100) and (111) hydrogen-terminated surfaces. Picture readapted from [37].*

for *surface sensitive* measurements, proving the surface behaviour of this feature: Graupner and colleagues have attributed this surface component to the to emission from adsorbed hydrocarbons, as confirmed by a mild annealing at 700°C where the S_A components disappeared (Fig.1.14).

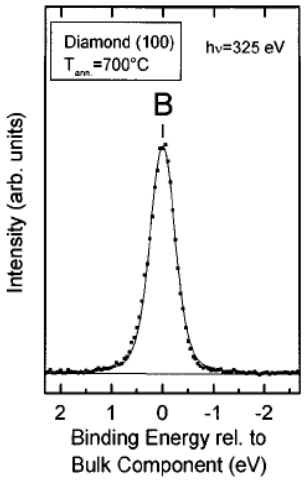

Figure 1.14: *C1s photoemission spectra for (100) hydrogen-terminated surfaces after a mild annealing at 700°C for 10 minutes. Spectrum is characterized by a single (B) peak attributed to bulk carbon. Picture taken from [37].*

Then, the samples were annealed at 1050° for 10 minutes: the relative spectra is depicted in Fig. 1.15.

This time a component toward lower binding energy appeared (indicated as S_C

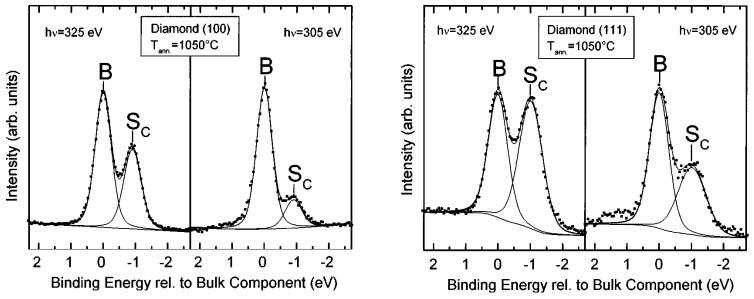

Figure 1.15: *C1s photoemission spectra for (100) and (111) hydrogen-terminated surfaces after an annealing at 1050°C for 10 minutes. Spectra are characterized by surface component (S_C) attribuited to hydrogen-free surface carbon. Picture taken from [37].*

in figure), shifted by -0.9eV for (100) surface and by -1.02eV for (111) surface. Again, the increase in the ratio between the S_C and B components using the

surface sensitive photelectrons confirms the surface nature of S_C, associated to surface carbons which have lost hydrogen (bonded as monohydride) during annealing.
Although the deconvolution performed by Graupner was accepted and used for successive works (such as in [38, 39]), recently an alternative interpretation of the C1s was proposed by Schenk and coworkers[40].

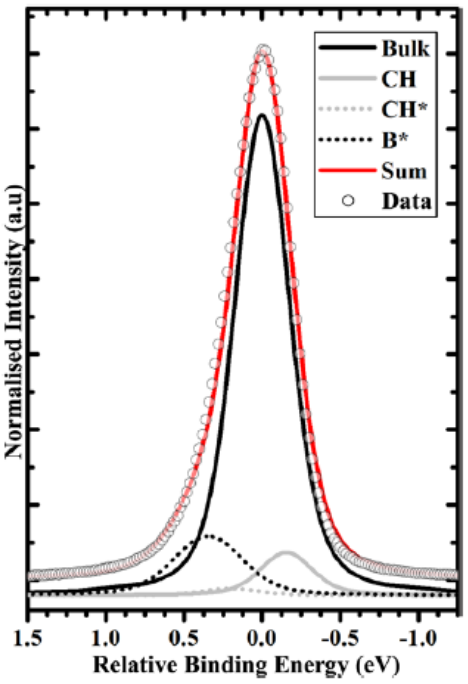

Component	Chemical shift (eV)[a]	Gaussian FWHM (eV)[b]	Assignment	Relative intensity[c]
B	0	0.31 ± 0.02	Bulk carbon	73.7%
B*	+0.36	0.40 ± 0.05	Sub-surface carbon layers	11.1%
CH	−0.16	0.30 ± 0.02	Hydrogen terminated carbon	13.0%
CH*	+0.20	0.30 ± 0.02	Vibrational loss from CH bond	2.2%

[a] Chemical shifts are calculated relative to the bulk component B, with a ±0.05 eV uncertainty.
[b] Values for Gaussian FWHM are averages of the values used for fitting all datasets measured on S1 and S2.
[c] Determined relative to the total C1s intensity.

Figure 1.16: *C1s spectra and its fit, as proposed by Schenk and coworkers[40]. Components used for the fit, their assignation and position respect to the bulk peak are presented in the table below the picture.*

This deconvolution, presented in Fig.1.16, has the following assignation:

- B is the Bulk related peak;
- CH and CH* are peaks related to the surface carbon atoms bonded with hydrogen atoms. CH peaks is located 0.15 eV towards lower binding energies with respect to B peaks, while CH* takes into account energy loss processes and is placed 0.20 eV from B peak towards higher binding energies
- B* peaks is related to subsurface carbons

This different deconvolution of C1s peak and the relative assignation of the peaks is related to some observation done by Schenk and coworkers:

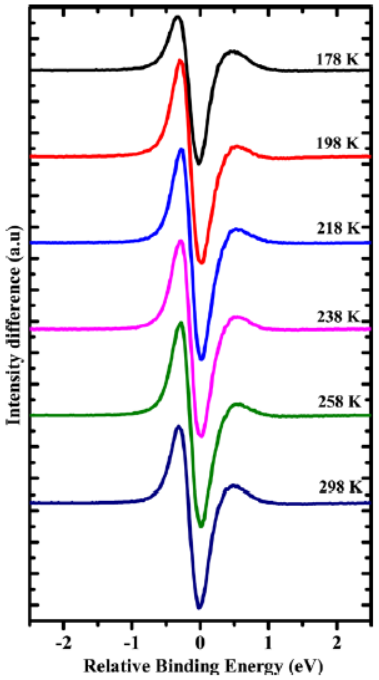

Figure 1.17: *Difference spectra between C1s core level acquired using photon energy of 350 eV (surface sensitive) and 850 eV (bulk sensitive); the zero represents the position of C1s maximum. Picture taken from [40].*

1. from the subtraction of the C1s spectra taken in surface sensitive regime (hν=350 eV) and bulk sensitive regime (hν=850 eV) they individuated

three bumps (Fig.1.17, where the subtraction has been repeated as a function of temperature): one of the three bumps was located near the zero that represents the C1s peak maximum) and was attributed to bulk carbon atoms. The two positive bumps, one located at higher and the other at lower binding energies respect to zero, were attributed to surface components;

2. they takes into account Pauling electronegativity for hydrogen (2.1) that is lower than the Pauling electronegativity for carbon (2.5) which tipically produces a chemical shifts toward lower binding energies;

3. the combination of initial and final state effects can justify the presence of a subsurface components in the higher binding energy zone near the bulk component.

Further analysis done as a function of temperature, moreover, confirm the presence of a peak, related to surface carbon atoms not bonded with hydrogen, placed at 0.8 eV towards lower binding energies with respect to bulk peak. Despite the two deconvolutions are done for hydrogen-terminated diamond in both cases the sample was first annealed, giving poor information about airborne adsorbates contribution.
However, it is well known that when surface transfer doping is established the effect of upward band bending is highlighted by a rigid energy shift of peaks in the photoemission spectra[25, 39, 41, 42].
Moreover, the contribution of hydrogen in XPS analysis is limited, in both cases, to the first layers of sample and no contribution from hydrogen as impurity in the sample has been observed.

Chapter 2 Experimental methods and setup

In the following chapter we are going to highlight, initially, the basic concepts of the electronic spectroscopies used for this work of thesis, that are the photoelectron spectroscopy and the electron energy loss spectroscopy. Then, the discussion will be moved on the experimental apparatuses used for preparation of samples and for spectroscopic and electrical characterization used for this thesis work. Different systems have been used: hydrogenation and electric measurements of diamonds films have been performed at the DiaTHEMA (Diamond, Thermal & Harsh Environment Materials & Applications) laboratory, in the Istituto di Struttura della Materia (ISM) of the Consiglio Nazionale della Ricerca (CNR), while the apparatus for spectroscopic measurements is situated in the LASEC (Laboratorio di Spettroscopie e Correlazione) laboratory of Università degli Studi Roma Tre.

2.1 Experimental methods

2.1.1 Photoemission spectroscopy

The quantity of molecules adsorbed on on a surface is a fundamental parameter for this work; the sensibility of core level photoemission in determine different atomic species and different bond configuration for the same species with its nanometric sensibility allows this kind of calculation; for this reasons in the following sections we first describe the basic theory of photoemission spectroscopy, highlighting its surface properties, and then we describe a model to calculate the fraction of surface covered by adsorbates.
In its essential aspects[43], the photoemission consists in the emission of elec-

trons from a surface when this is impinged by electromagnetic radiation. For the energy conservation any photoemitted electron will have a kinetic energy related to the photon energy and by the structural characteristic of the sample, following the relation:

$$E_k = h\nu - E_B - \phi, \tag{2.1}$$

where E_B is the energy of the electron in its initial state (the so-called binding energy) and ϕ is the work function of the sample.
A rigorous approach to the study of phomoemission from solids requires a quantum description of the process in which an electron, in a electronic occupied state of the solid, is excited by the photon, escapes from solid and then reaches the detector, all in a single step. However, the photoemission process is typically divided in a less-accurate but more simpler three-step process, that are:

1. optical excitation of an electron from an initial to a final electronic state, still into the lattice;

2. propagation of excited electron to the solid surface;

3. emission of electron from solid to vacuum passing through the solid surface.

The three-step assumption permits to factorize the three contributes in the determination of emitted electron current.

The optical excitation of an electron can be treated in terms of quantum mechanics as a perturbation between the photon and the electronic cloud of the solid. The total hamiltonian of the system is obtained by minimal substitution[44] and it is:

$$H = H_0 + H_\gamma, \tag{2.2}$$

where

$$H_0 = \frac{p^2}{2m} + V(\mathbf{r}) \tag{2.3}$$

is the unperturbed term and

$$H_\gamma = -i\frac{e\hbar}{mc}\mathbf{A}\cdot\nabla \tag{2.4}$$

is the perturbation term caused by the radiation-matter interaction ($\mathbf{A}$ is the potential vector).

So the probability of a transition from a initial state $|i,k\rangle$ to a final state $|f,k\rangle$ can be obtained in the time-dependent perturbation theory by the Fermi's Golden Rule:

$$W_{fi} = \frac{2\pi}{\hbar}|M_{fi}|^2\delta\left(E_f(\mathbf{k}) - E_i(\mathbf{k}) - \hbar\omega\right) \tag{2.5}$$

with

$$M_{fi} = \langle f,k|H_\gamma|i,k\rangle. \tag{2.6}$$

The δ describes the energy conservation passing from the state $E_i(\mathbf{k})$ to the state $E_f(\mathbf{k})$.
The electron current density for this step, for electrons with energy E and internal momentum (respect to the sample) can be described by the relation:

$$I^{int}(E,\hbar\omega,\mathbf{k}) \propto \sum_{fi}|M_{fi}|^2 f(E_i)\delta(E_f(\mathbf{k}) - E_i(\mathbf{k}) - \hbar\omega). \tag{2.7}$$

The main effect of the electrons propagation in the solid, the second step described above, is the scattering of electrons with the atoms in the solids, with the loss of any information about the electrons initial state. These scattered electrons contributes to the secondary electrons background typically present in the photoemission spectra. The propagation of electrons can be described by the probability $D(E,k)$ that electrons, moving to the surface do not experience scattering events. This probability is proportional to the mean free path:

$$D(E,k) \propto \lambda(E,k). \tag{2.8}$$

As can be seen in fig. 2.1, for typical photoemission energies the mean free path is limited to few monolayers, that are roughly between 5 and 30 Å. Thus, the main effect is that the informations from a photoemission experiment are limited in depth on the first layers of the solids, near to the surface.

As said, the transition of a photoelectron through the surface, can be treated as the scattering of a Bloch electron wave from the surface-atom potential with translational symmetry parallel (but not normal) to the surface. Because of the 2D translational symmetry, the transmission of the electron through the surface into the vacuum requires conservation of its wave-component parallel to the surface:

$$\mathbf{k}_\parallel^{ext} = \mathbf{k}_\parallel + \mathbf{G}_\parallel, \tag{2.9}$$

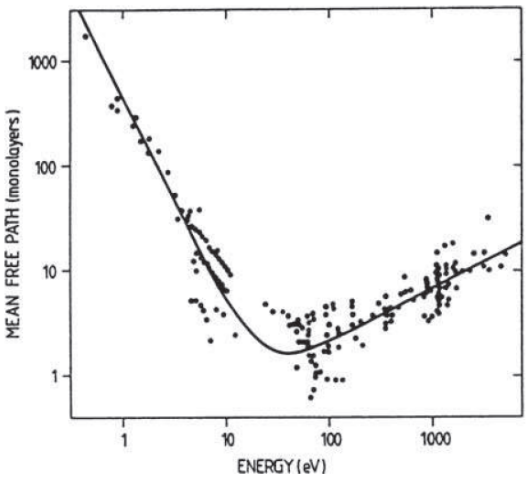

Figure 2.1: *Mean Free path of electrons. Picture taken from [45].*

where $\mathbf{k}$ and $\mathbf{k}^{ext}$ are, respectively, the wave vector inside and outside the solid. The factor of electron current relative of the third step can be described by the transmission coefficient

$$T(E, \mathbf{k})\delta(k_{\|} + G_{\|} - k_{\|}^{ext}), \tag{2.10}$$

where $T(E, \mathbf{k})$ is zero for electrons with $k_{\perp}^{ext} < 0$.
Combining (2.7), (2.8) and (2.10) the photoelectron current escaping form the solid can be written as:

$$I^{ext}\left(E; \hbar\omega, k_{\|}^{ext}\right) = I^{int}\left(E; \hbar\omega, \mathbf{k}\right) D(E, \mathbf{k}) T(E, \mathbf{k})\delta(k_{\|} + G_{\|} - k_{\|}^{ext}). \tag{2.11}$$

2.1.2 Photoemission products

In order to understand correctly the features appearing in a photoemission spectrum we recall again the expression for the probability W_{fi} of transition from an initial state $|i, k\rangle = |i\rangle$ to a final state $|f, k\rangle = |f\rangle$: that the photon wavelength is much larger with respect to the system dimensions, it is possible to use the dipole approximation, in which $e^{(i\mathbf{k}\cdot\mathbf{r})} \simeq 1$ and the transition matrix-element can be expressed as a dipolar overlap integral between initial and final state:

$$W_{fi} \propto \frac{2\pi}{\hbar}|\langle f|r|i\rangle|^2 \delta\left(E_f(k) - E_i(k) - \hbar\omega\right). \tag{2.12}$$

The main issue, at this point, is to find the correct way to represent the initial and final states: for example in an atom that have the form of the

product of radial terms and spherical harmonics, so that $\phi_{n,j,m}(r,\theta,\varphi) = R_{n,l}(r)Y_{l,m}(\theta,\varphi)$, molecule often are approximated via a linear combination of atomic orbitals (LCAO) [44]; finally, in solids they are expressed in terms of Bloch functions[46].
assuming a strong *one-electron* behavior for the photoemission process a convenient choice for the initial state results to be the product of k-th *active* electron wave function ϕ_k and a N-1 electron residual due to the other *passive* electrons, represented by $\Phi^k_{i,R}(N-1)$:

$$|i\rangle = C|\phi_k\rangle|\psi^k_{i,R}(N-1)\rangle, \tag{2.13}$$

where C is an operator that antisymmetrizes properly the wave function. In a similar way the final state can be represented as the product between the wavefunction of the photoemitted electron, $\phi_{f,Ekin}$ and a N-1 electron residual $\Phi^k_{f,R}(N-1)$, so that:

$$|f\rangle = C|\phi_{k,Ekin}\rangle|\psi^k_{f,R}(N-1)\rangle. \tag{2.14}$$

Assuming now that the photoemission process is quicker than the relaxation time of residual electrons (assumption often called sudden approximation) the matrix element can be decomposed into the product of a one-electron matrix element (called the dipole term) and the overlap integral between N-1 electrons residual wavefunctions in the initial and final states (the monopole term):

$$\langle f|r|i\rangle = \langle\phi_{k,Ekin}|r|\phi_k\rangle\langle\psi^k_{f,R}(N-1)|\psi^k_{i,R}(N-1)\rangle, \tag{2.15}$$

At this stage it is possible to assume that the residual N-1 electrons are not going to relax. This case is termed as frozen orbital, the natural framework of the Koopmans' theorem, based on the assumption that the one-electron orbitals in the initial state are the same of the final one; in other words that the hamiltonian describing the system both in the initial and final states is the same, implying the presence of a single core hole in the k-th sublevel. Because of the orthonormality of the residual wavefunctions $\Psi(N-1)$ the matrix element is reduced to the dipole electron term. The expected photoemission spectrum in this case is characterized by a single peak, called Koopmans' or adiabatic peak.
For a more detailed description relaxation effect of the ionic residuals after the photoemission have to be included. In this case the Hamiltonian describing the

initial state is no more the one describing the final state too. Such behavior is due to the reorganization of the N-1 remaining electrons, with a consequent change in the electron potential, after the electron ejection via photoemission. In that case the initial ionic residual wavefunction can be projected on more than one final (N-1)-state, giving access to the so-called satellite structures (also called shake-up, shake-off, ore correlation peaks, depending on their nature) beside the adiabatic peak.

2.1.3 Chemical shift

The investigation of molecules or solids could be not focused in absolute binding energy of a core level, but in the change in binding energy between two different chemical forms of the same atom. This energy difference is called chemical shift.
To explain chemical shift we will discuss the simple case presented byin [47] of the lithium 1s core level in metal and in lithium oxide, shown in fig.2.2. As represented in figure, in metallic lithium the 2s electrons form a band, so

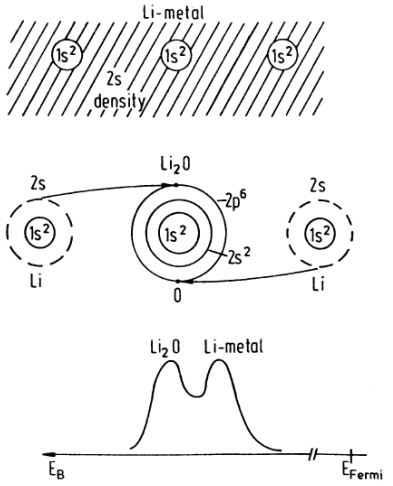

Figure 2.2: *schematic drawing of electron configuration for metallic lithium and lithium oxide and relative PES spectra. Picture taken from [47].*

their wavefunction are located only partially at the site of a particular lithium atom. On the contrary in lithium oxide the 2s electron of lithium are totally donated to the 2p shell of oxygen, so in this case 2s electron of lithium have no part of its wavefunction near the lithium atom. Formally this situation can

be interpreted in simple way in terms of different coulomb interaction as done in the charge-potential model [48]: in this model the ionization energy E_i of a particular level in a atom depends on the potential generated by the electrons in the valence band and electrons of the surrounding atoms, so that E_i can be described with the relation:

$$E_i = E_i^0 + kq_i + \sum \frac{q_i}{r_{ij}}, \quad (i \neq j) \tag{2.16}$$

where E_i^0 is the reference binding energy (in absence of chemical shift), kq_i is the contribution of valence band electrons and q_i/r_{ij} represents the potential generated by the surrounding atoms. In this picture we are describing the atom as a sphere surrounded by a kq_i charge distributed over a radius r_v due to valence band electrons: the potential inside the sphere is kqi/r_v and any charge variation Δq_i will induce a potential variation in the sphere, that will be reflected also in the deepest electronic levels. For example, if the number of electrons increases then $\Delta q_i < 0$ and there will be a decreasing in the binding energy; instead, taking in account the average radius, if r_v is increased (maintaining q_i fixed) then the quantity $\Delta q_i/r_v$ will decrease.
Taking into account this framework in lithium oxide the 1s electrons feel a stronger Coulomb interaction than in metallic lithium; at the same time the 1s electrons of metallic lithium are also screened through the 2s valence electrons. The result is that the binding energy of Li1s level is larger in lithium oxide (and, in fact is 55.6 eV[49])than in metallic lithium (55.0 eV[50]), and a chemical shift will be observable.

2.1.4 Adsorbate coverage estimation

We now describe a model to calculate the fractional adsorbate coverage; this method was first described by C.S. Fadley in[43].
We consider now a photoemission event: the photoelectron peak intensity dN_k (i.e the number of photoemitted electrons) produced after a transition from the subshell k and originating from the volume $dxdydz$ can be written as a product of different terms, including:

- the x-ray flux I_0;
- the number of atoms (or molecules) in the elemental volume, given by

$\rho(x,y,z)dxdydz$, with $\rho(x,y,z)$ density of atoms(molecules) in the sample;

- the differential cross section for k subshell $\frac{d\sigma_k}{d\Omega}$;
- the solid angle acceptance of electron analyzer $\Omega(E_{kin}, \mathbf{k})$ that also defines the effective specimen area A_0;
- the probability of no-loss escape from the solid $T(E_{kin}, \mathbf{k})$;
- the instrumental detection efficiency $D_0(E_{kin})$;

notice that the solid angle acceptance of electron analyzer Ω, the probability of no-loss escape from the solid T and the instrumental detection efficiency D_0 all depends by the kinetic energy of the escaped electron. Taking into account all these terms the differential intensity can be written as:

$$dN_k = I_0\rho(x,y,z)\frac{d\sigma_k}{d\Omega}\Omega(E_{kin},\mathbf{k})T(E_{kin},\mathbf{k})D_0(E_{kin}), \tag{2.17}$$

or, for uniform-density but bounded, specimen:

$$dN_k = I_0\rho(x,y,z)\frac{d\sigma_k}{d\Omega}\Omega(E_{kin},\mathbf{k})\exp\left[\frac{-l}{\Lambda_e(E_{kin})}\right]D_0(E_{kin}), \tag{2.18}$$

where l is the path length to escape from the sample and $\Lambda_e(E_{kin})$ is the inelastic mean free path (IMFP).
With simple assumptions it is easy to integrate eq.(2.18) for a number of cases: considering, in fact, an atomically flat sample and neglecting any effect of single-crystal anisotropies in emission and elastic electron scattering effects, assuming an emission angle θ with respect to the sample surface, it is possible to integrate the precedent relation over the sample volume, that in the limit of semi-infinite sample, can be expressed as:

$$N_k = I_0\Omega_0(E_k)A_0(E_k)D_0(E_k)\rho\frac{d\sigma_k}{d\Omega}\Lambda_e, \tag{2.19}$$

where $E_{kin} = E_k$.
Equation 2.19, however, describes a general case of a photoemission from a clean sample and does not take in account the presence of molecules adsorbed on the sample surface: they can be represented as a non-attenuating layer, because of the negligible thickness, with a fractional monolayer coverage; the

signal of the electrons related to molecules from the overlayer will then generate the peak l, that can be described by the relation:

$$N_l(\theta) = I_0 \Omega_0(E_l) A_0(E_l) D_0(E_l) s' \frac{d\sigma_l}{d\Omega} (\sin\theta)^{-1}, \tag{2.20}$$

and so the overlayer/substrate ratio can be expressed as:

$$\frac{N_l(\theta)}{N_k(\theta)} = \frac{s'}{s} \cdot \frac{\Omega_0(E_l) A_0(E_l) D_0(E_l) (d\sigma_l/d\Omega) d}{\Omega_0(E_k) A_0(E_k) D_0(E_k) (d\sigma_k/d\Omega)(\Lambda_e \sin\theta)}, \tag{2.21}$$

with

- **s'** is the mean surface density of atoms in which peak l originates;
- **s** is the mean surface density of substrate atoms;
- **s'/s** is the fractional monolayer coverage;
- **d** is the mean separation between layers in the substrate.

Thus, inverting the relation it is possible to determine the portion of sample covered by adsorbates:

$$\frac{s'}{s} = \frac{N_l(\theta)}{N_k(\theta)} \cdot \frac{\Omega_0(E_k) A_0(E_k) D_0(E_k) (d\sigma_k/d\Omega)(\Lambda_e \sin\theta)}{\Omega_0(E_l) A_0(E_l) D_0(E_l) (d\sigma_l/d\Omega) d}. \tag{2.22}$$

2.1.5 Electron energy loss spectroscopy

At the basis of electron energy loss spectroscopy (EELS) there are elastic and inelastic electron scattering events used to obtain information on symmetry and geometric arrangement (by elastic process) and on excitation quanta (by inelastic process) of the system investigated so, in simple terms, an energy loss experiment consists to impinge electrons coming from a properly collimated a monochromatized beam on a solid and then study how they interact with it. The energy range of electron beam spans from few meV to KeV, depending on what are the excitations of interest (such as molecular vibration, plasmon, interband or core transition, as presented in Fig.2.3). For these energies, the mean free path of electrons is limited to few Ångstroms: this feature gives to EELS a strong surface behaviour.

Characteristic of inelastic scattering process is the conservation of energy and, if the sample has crystalline order, conservation of the parallel component of

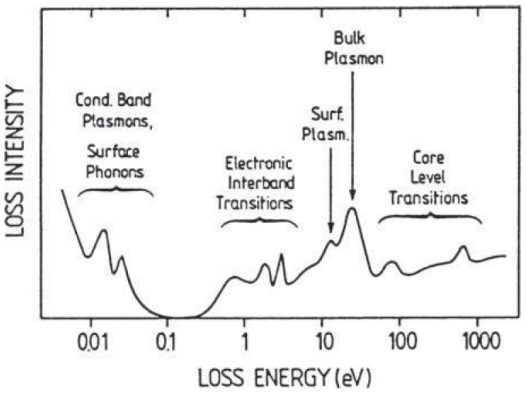

Figure 2.3: *Qualitative overview of the major excitation mechanisms which can contribute to an electron energy loss spectrum over a wide loss energy range. Picture taken from [45].*

momentum respect to the surface (up to a reciprocal lattice vector $\mathbf{G}$). So if ω and q are respectively frequency and momentum of the excitation in the material, the difference between initial and final energy and momentum for the electron are:

$$E_f - E_i = \hbar\omega, \tag{2.23}$$

$$\mathbf{k}_{f,\parallel} - \mathbf{k}_{i,\parallel} = \mathbf{k}_{\parallel} + \mathbf{G}_{\parallel}, \tag{2.24}$$

but for extrapolate more information about excitation properties and nature a more detailed description is needed.

As described by Ibach and Mills in [32], two are the way of interactions of electrons with the atoms and molecules: they, oscillating, produce a small-angle scattering given by the oscillation of electrical dipole momentum (for this reason called dipole scattering). This small-angle scattering distribution is overlapped with a large-angle distribution of inelastically scattered electron; this last regime is called the impact scattering and needs a fully microscopical description of interaction between electrons and substrate.
A complete analysis of electron scattering needs both two scattering contributes but practically the two regimes are typically described separately. Moreover, it has been demonstrated that in certain cases (e.g. in specular conditions) the contribute of impact scattering is negligible.
For this reason we restrict the discussion to the dipole scattering: suppose

to have a scattering event between an electron and a small molecule without taking in account any surface or crystalline structure. The position of each nucleus is $\mathbf{R}_l = \mathbf{R}_l^{(0)} + \mathbf{u}_l$, where $\mathbf{R}_l^{(0)}$ is the equilibrium position and $\mathbf{u}_l$ the vibrational motion around that position. If the electron interacts with the molecule by a 2-body potential we have:

$$V(\mathbf{x}) = \sum_l V_l\left(\mathbf{x} - \mathbf{R}_l\right). \tag{2.25}$$

Using the first Born approximation (i.e. neglecting multiple scattering terms) the matrix element of a scattering event of an electron with wave vector $\mathbf{k}_i$ into a final state $\mathbf{k}_f$ is described by:

$$V(\mathbf{k}) = \int \frac{d^3x}{V}\, e^{i\mathbf{k}\cdot\mathbf{x}}\, V(\mathbf{x}), \tag{2.26}$$

where V is the volume and $\mathbf{k} = \mathbf{k}_i - \mathbf{k}_f$ is the exchanged momentum. Using the (2.25), equation (2.26) can be rewritten as

$$V(\mathbf{k}) = \sum_l V_l\left(\mathbf{k}\right) e^{i\mathbf{k}\cdot\mathbf{R}_l}, \tag{2.27}$$

where $V_l\left(\mathbf{k}\right) = \int \frac{d^3x}{V}\, V_l(\mathbf{x})\, e^{i\mathbf{k}\cdot\mathbf{x}}$ is the Fourier transform of single potential. Now we are going to consider only the first order contribution of potential $V^{(1)}(\mathbf{k})$ in nuclear displacement $\mathbf{u}_l$, that is

$$V^{(1)}(\mathbf{k}) = i\sum_l V_l\left(\mathbf{k}\right) e^{i\mathbf{k}\cdot\mathbf{R}_l^{(0)}}\, \mathbf{k}\cdot\mathbf{u}_l. \tag{2.28}$$

At this stage we impose the dipole approximation: in regime of small scattering angles, i.e. when the condition $|\mathbf{k}|d_0 \ll 1$ is verified, where d_0 is the size of molecules (or, in case of electronic transition, the spatial extension of the orbital involved) the exponential $e^{i\mathbf{k}\cdot\mathbf{R}_l^{(0)}}$ can be set to the unity. Moreover we consider the limit for $|\mathbf{k}| \to 0$ for which we have:

$$\lim_{|\mathbf{k}|\to 0} V_l(\mathbf{k}) = 4\pi\frac{Z_l e^2}{k^2}, \tag{2.29}$$

with Z_l that is the net charge surrounding the l-th nucleus. Finally we have:

$$\begin{aligned} \lim_{|\mathbf{k}|\to 0} V_l^{(1)}(\mathbf{k}) &= i4\pi\frac{\mathbf{k}}{k^2}\sum_l e\; Z_l\mathbf{u}_l \\ &= i4\pi\frac{\mathbf{k}\cdot\mathbf{p}}{k^2}, \end{aligned} \tag{2.30}$$

where $\mathbf{p} = \sum_l e\ Z_l \mathbf{u}_l$ represents the oscillating part of electric dipole of the molecule. In principle, with is picture is possible to describe not only vibrational motion of molecules, but any other excitation of the system, for example electronic transitions, where $\mathbf{p}$ is given by $e\langle\psi_f|x|\psi_i\rangle$, and it is possible to cast the dipole scattering formula in language sufficiently general that the result may be applied to inelastic scattering by fluctuations in the electronic degrees of freedom, as well as the vibrational modes.
In this sense, following the description done by Ibach, Evans and Mills in their works [32, 51, 52], near specular reflection (i.e. with an angle less than $\hbar\omega/2E_0$ where ω is the frequency of the excitation and E_0 is the initial energy of the electron impinging on the sample), the probability amplitude for a scattering event highlights four ways of interaction:

- the electron can approach the surface and then, at some point in the vacuum above the crystal, it may scatter from the fluctuating electric field without ever striking the crystal surface;
- the inelastic scattering of the electron may be preceded or followed by an elastic event;
- finally, the inelastic scattering of the electron takes place between two elastic scattering events.

It is possible to demonstrate that the events in which the inelastic scattering precedes or follows an elastic event are dominant with respect to the other events and that the elastic reflection carries the major amount of exchanged momentum, so that little deviations from specular reflection correspond to little wave vector exchanged in the inelastic process, provided that $\hbar\omega$ is sufficiently smaller than the primary electron energy. Same conclusions have been obtained by Saldin by calculations on ionization of inner shell [53], suggesting that in reflection geometry the inelastic collision is always followed by an elastic scattering. Finally this result has been also been verified experimentally on graphite by Ruocco et al. [54] and by Iacobucci and coworkers[55]. In this context, the cross section carried out by Ibach and Mills by quantum calculation is equivalent, except for a Bose occupation factor n($\hbar\omega$)+1, to the results of dielectric classic theory presented by Lüth [45, section 4.6], because both the description start with the hypothesis that scattering is caused by long-range

potential set by the sample, due to polarization caused by the field of incoming and outgoing electrons. So the cross section for an electron with velocity $\mathbf{v}$, exchanged energy $\hbar\omega$ and exchanged momentum $\mathbf{k}$ is proportional to:

$$\frac{d^2\sigma}{d(\hbar\omega)d\Omega} \propto \frac{m^2e^2|R|^2}{2\pi^3\hbar^4\cos\theta}\frac{v_\perp^4 k_\parallel}{\left[v_\perp^2 k_\parallel^2 + \left(\omega - \mathbf{v}_\parallel\cdot\mathbf{k}_\parallel\right)^2\right]^2}\mathrm{Im}\left\{\frac{-1}{\varepsilon(\omega)+1}\right\}. \tag{2.31}$$

It is possible to recognize three factors: the first presents some constants, such as electron mass and charge, the surface reflectivity R and the emission angle θ, the second is a kinematic factor containing velocity and exchanged momentum components and, finally, the third one is the so-called surface loss function. Note that in the limit of small-angle scattering the momentum dependence is neglected: this means that in specular reflection EELS measurements probes the optical dielectric function, giving the possibility of a direct comparison with optical absorption spectra.
Finally, the surface loss function can be rewritten in terms of real and imaginary part of dielectric function:

$$\mathrm{Im}\left\{\frac{-1}{\varepsilon(\omega)+1}\right\} = \frac{\varepsilon_2(\omega)}{[\varepsilon_1(\omega)+1]^2+\varepsilon_2(\omega)^2}, \tag{2.32}$$

And it is easy to see that is peaked (and so will be the EELS cross section) in correspondence of $\varepsilon_2(\omega)$ maxima, like it happens for optical absorption spectra, but with the advantages to explore a larger portion of reciprocal space (not being limited by the small momentum of the photons), with an higher sensitivity of low adsorbate coverages.

2.2 Experimental setup

2.2.1 Hydrogenation chamber

The chamber devoted to hydrogenation was originally produced by AsteX and is pumped by a combination of rotative and turbomolecular pump so as to obtain a base pressure of 10^{-7} mbar, in order to minimize any possible contamination.
The chamber has a cylindrical shape and it is attached to a microwave generator (2.6 GHz) via a rectangular wave-guide (equipped with three stubs for the control of the reflected power) with a mode converter. Plasma is generated above a substrate (as depicted in Fig. 2.4) where the samples are placed

manually; the distance between the position of the substrate holder and the microwave-transparent quartz window is adjustable (in order to optimize the cylindrical resonant cavity geometry), differently from sample position on the treatment plane, that is adjustable only before the pump system is activated. The substrate table can be heated inductively and in this work it has been used for temperature up to 750°C. The hydrogen gas is admitted to the reactor via stainless steel canulas and its flow rates is adjusted with controllable mass flow meters: an MKS gas rate control unit is used with the possibility of controlling and using various gas systems, though for this work we used it only for hydrogen.

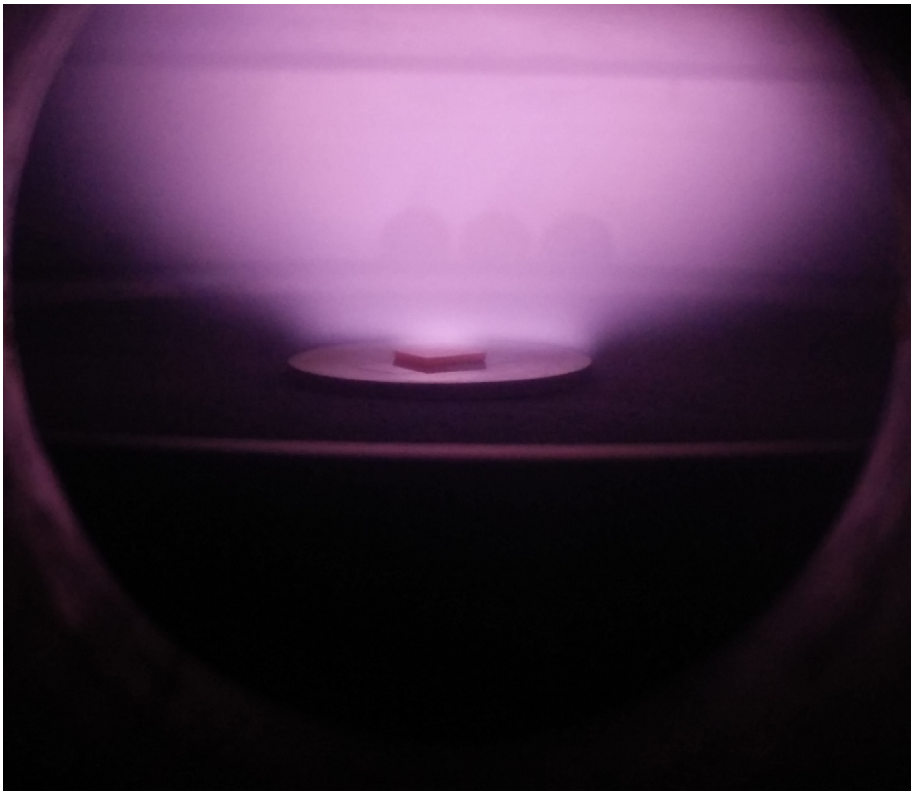

Figure 2.4: *Hydrogenation of diamond sample by exposure to hydrogen plasma.*

2.2.2 Electrical measurements chamber

Electrical measurements has been performed in the VTEC (Vacuum and Temperature Electronic Characterization) chamber (depicted in Fig. 2.5): sample

was mounted onto a floating copper block while two molybdenum clips ensured electrical contact and, at the same time, they fixed the sample in place on the holder. Copper block was mounted on the upper face of a boron nitride block (that provided electric - but not thermal- insulation) and heated by a tantalum filament inserted in this block. All this structures lied on a Macor block, that provided both electrical and thermal insulation of the whole upper structure. Heating is controlled by two thermocouples inside the boron nitride block and on the top of sample holder; upper limit for temperature is 600°C.
The entire heating system is mounted on a five degrees of freedom manipulator since the same setup is used to perform photocurrent emission measurements. VTEC chamber is also equipped with two stages dedicated to thermionic and PETE (photo-enhanced thermoionic emission) measurements.
The chamber is maintained in vacuum (the base pressure is 10^{-7}mbar) by a combination of a scroll and a turbomolecular pump: in this case the vacuum avoids any molecules adsorption on our sample during the resistance measurements; it is therefore possible to perform resistance measurements on both covered and adsorbate-free samples.

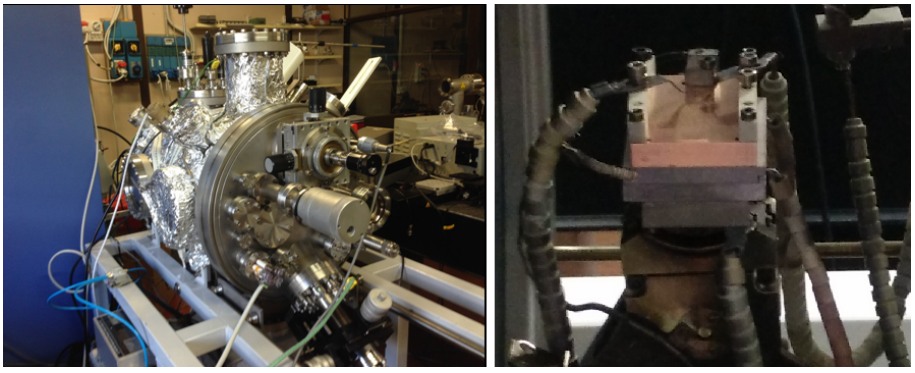

Figure 2.5: *On the left: VTEC (Vacuum and Temperature Electronic Characterization) chamber; on the right: detail of the heating system used for electrical measurements.*

2.2.3 Resistance pattern

Besides the two systems (the apparatus for hydrogenation and the setup for resistance as a function of temperature and pressure) we showed before, we

expressly developed for this work a setup for four-probe resistance measurements (in Van der Pauw configuration) able to perform measurements as a function of position on the sample (in order to obtain a resistance pattern on the sample).
The four-probe setup (presented in Fig.2.6) was mounted on a micrometrically controlled handling system with three degree of freedom (x,y,z). The probes are spaced by a distance of 1mm from each other: two probes were connected to a current generator, the latter ones to a voltmeter. Both the voltmeter and the current generator was controlled remotely with a calculator: for this purpose we specifically developed a control program (written in LabVIEW) able at the same time to acquire data.

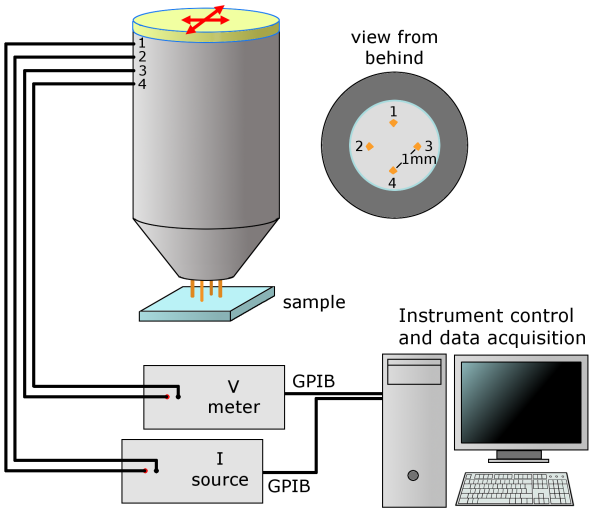

Figure 2.6: *Reproduction of the scattering plane in LASEC experimental chamber, with the arrangement of various sources and analyzers.*

2.2.4 Two- versus Four-point measurements

The four-point probe is commonly used to measure resistance on semiconductor samples. Despite two-point probe measurements can appear simpler to be implemented and performed, conversely the data interpretation is more complicated with respect to the four-point probe method, that does not need any calibration standard and does not depend on the probe-semiconductor con-

tact resistance. In the case of two-point measurements, in fact, the contact serves both for current and voltage probe and the total resistance R_{2pt} given by measurements is describable with the relation[56]:

$$R_{2pt} = R + 2R_w + 2R_c, \tag{2.33}$$

where R is the resistance of the measured sample, R_w is the wire and probe resistance and R_c is the contact resistance. All the three components are temperature dependent. For a non-degenerate semiconductor, R is a decreasing function of temperature as well as the contact resistance R_c (e.g. [57]). Conversely, being the wires and probes usually made of metals, R_w is an increasing function of temperature.

Then, in order to avoid any unwanted contribution with no calibration of the measurement system, the four-probe method is the typical alternative. It works separating the current and the voltage paths by using two probes for current injection and other two probes for voltage measurements, as schematized in Fig. 2.7: in this way, though R_w and R_c are still present on voltage path, the high input impedance of voltmeter makes negligible the current flowing trough them as well as the related voltage drops, resulting in the measurement only of the sample resistance.

Different disposition of the four probes can be used but the typical setup

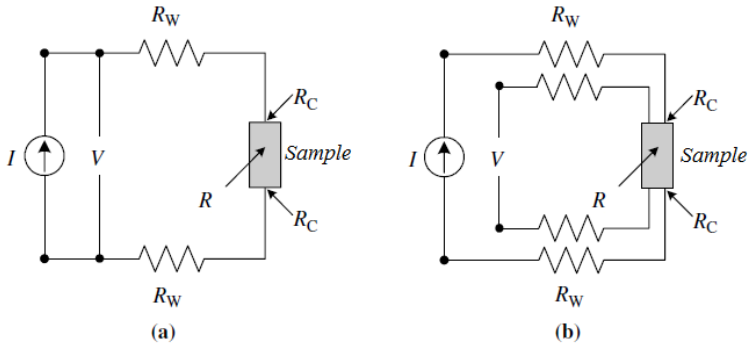

Figure 2.7: *Two-terminal(a) and four-terminal(b) resistance measurement arrangements. Picture readapted from[56].*

involves a linear or square-shaped (the so-called Van der Pauw configuration) arrangement of the probes. Once known the probe geometry, the sheet resistance of the material can be derived directly from the measured resistance

R_{4pt}. For example, both for linear and for Van der Pauw configurations, if the measurement geometry satisfies the conditions of a distance among the probes far larger than the conductive sheet thickness of the material under test and a probe distance smaller than the lateral size of the sample, the sheet resistance $R_{\square}$ is equal to:

$$R_{\square} = \frac{\pi}{\ln 2} R_{4pt}, \tag{2.34}$$

and, if the conductive sheet thickness d of the material is known, also the resistivity can be derived from

$$\rho = R_{\square} d. \tag{2.35}$$

In hydrogenated diamond substrates, the conductive sheet thickness reported

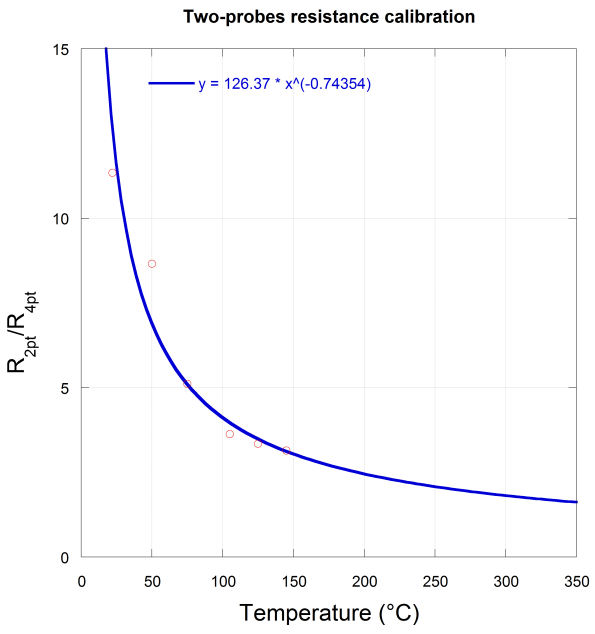

Figure 2.8: *Calibration of two-probes measurements setup. The resistance of a diamond sample has been measured with both two-probe and four-probe setups, as a function of temperature. From the measurements we extrapolated a calibration curve.*

in literature ranges from few to tens of nanometers [19, 21, 58] and the lateral size is quite larger than the probing distance. Although the conditions of a thin and conductive film larger than the probing distance are respected, in the

following we will not derive the resistivity values because we have not got an accurate experimental evaluation of the hole conductive depth.
Since the resistance measurements has been conducted with both two- and four-probes setups, we performed a calibration of two-probes setup in order to maintain the compatibility of the two sets of measurements. The calibration has been performed as a function of temperature: for the same diamond sample we conducted both two-probes and four-probes measurements at the same distance (1mm) between the probes, for temperatures up to 250°C, that is the recommended maximum value achievable by the four-probes setup. From the evolution of the ratio between the measurements performed with the two-probes setup (R_{2pt}) and the measurements performed with the four-probes setup (R_{4pt}) as a function of temperature we then extrapolated a phenomenological calibration curve, shown in Fig. 2.8. The curve has been used to determine the $2R_c+2R_W$ value and thus to correct the two-probes measurements that will be showed in the following chapters. Indeed, with the phenomenological approach shown we can introduce some further aspects regarding the calibration and the evolution of the three resistance values: even at high temperatures R_w is on the order of few to tens of ohms and therefore it is negligible respect to the other resistance values: the resistance measured by the two-probe setup can be attributed only to R_c and R.
Fig. 2.9 shows the extrapolated values of contact resistance as a function of temperature: with respect to the typical evolution shown for doped semiconductors [57], where it decreases when temperature increases, we observed the opposite behaviour in the temperature range studied. The trend can be easily explained. Differently from doped semiconductors, hydrogen-terminated diamond operated with the transfer doping effect performed by the adsorbates. Airborne species, in fact, desorb upon increasing temperature: this leads to an increasingly intrinsic semiconductor, thus altering the contact resistance and its behaviour as a function of temperature.
For the same reason R is hardly temperature dependent and, regarding Fig. 2.8, the particular evolution shown for R_{2pt} and R_{4pt} ratio shown (that is essentially a function of $R_c/R+1$), demonstrates how R is dominant for high temperatures respect to R_c.

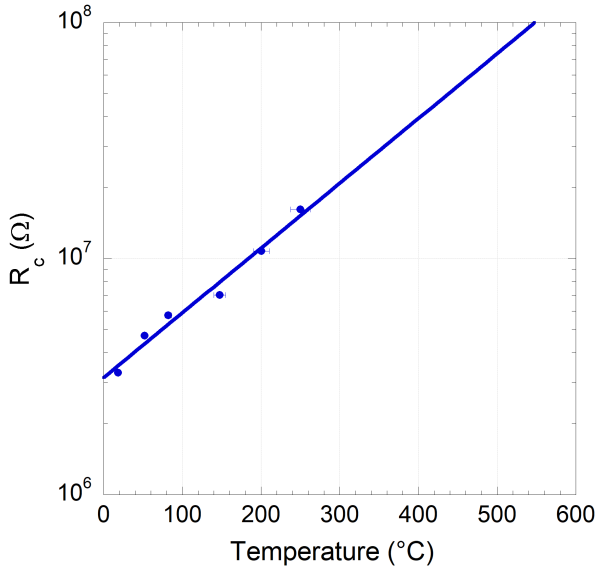

Figure 2.9: *Evolution of contact resistance (R_C) as a function of temperature. Differently for high doped semiconductors[57] the contact resistance increases as temperature increases: we attributed this behaviour to the change in diamond doping that may alter contact resistance.*

2.2.5 Apparatus for electron spectroscopies

The apparatus for spectroscopic measurements is structured into two Ultra-High Vacuum (UHV) chambers in communications. The chambers are devoted to different purpose: one chamber (the preparation chamber) is equipped with a oxygen dissociation system (described in detail later), a MassTorr quadrupole spectrometer and a LEED apparatus. The chamber is also equipped for the introduction of sample in UHV conditions.
The other chamber is devoted to perform measurements (and thus we refer to it as the measurements chamber) and it is equipped with a Alk_α source, an He lamp (not used in this work), an electron gun and a hemispherical analyzer. Regarding the equipment used, the X-Ray source is a Omicron XMR 1000 source in which photons are produced bombarding an aluminium anode with electrons produced by a cathode filament and accelerated toward the anode over a potential of 15 kV. The X-Ray produced are the monochromatized and focused onto the sample with quartz mirrors.
The electron gun is a custom source expressly realized to perform spectroscopic measurements. Electrons are produced by thermoionic emission, selected in energy by a 33mm hemispherical section (similar to the one used for electron detection) and then focused on sample by a three-cylindrical electrodes system. Beam energy used in all experiments is around 100 eV with typical electron current incident on the sample between 30 and 70 pA.
Finally, the electron analyzer consists in three parts:

- a cylindrical electrode that is used as a transport system for the electrons coming from the sample;
- a hemispherical element with a radius of 66mm, opportunely polarized, able to select the electrons as a function of their energy. During the energy scans the hemispherical element has been used in constant Pass Energy mode, in order to have a fixed resolution for each spectrum. Values of Pass Energy tipically used in the various experiments are 2 eV for EELS (achieving a total resolution of 80 meV) and 20-40 eV for XPS (total resolution around 0.35 and 0.45 meV, respectively);
- a Micro-Channel Plate, that acts as a detector for the electrons selected in energy.

For further information of the working details about the three elements and how the pass energy and the radius of the hemispherical element influence the energy resolution we refer to the specific literature[59, 60].

The two chamber are maintained at a base pressure of 10^{-10} mbar and characterized to have a separated pump system (shown in Fig. 2.10), so that the chambers can be separated with a gate valve and maintained in UHV condition independently. Diamond samples are placed on a molybdenum sample

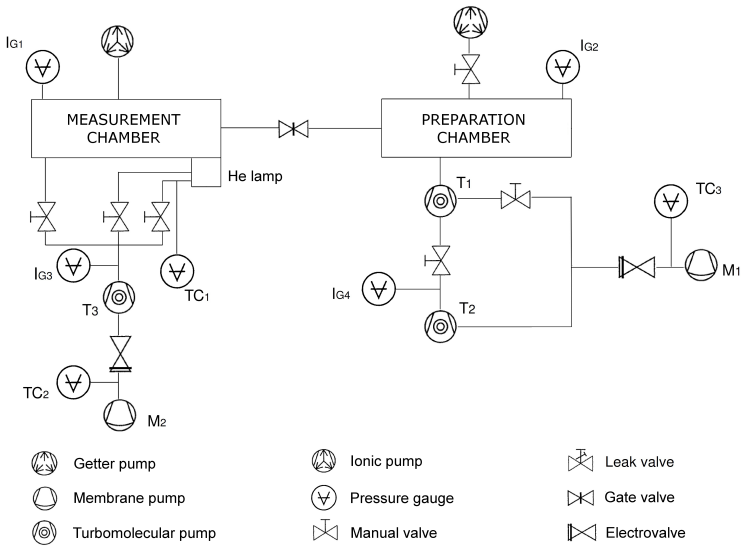

Figure 2.10: *Schematic of pump system for the experimental chamber used to perform spectroscopic measurements.*

holder and are maintained in position with a tantalum mask on which we have grown a gold layer of 200nm: the mask, prepared in this way, has the advantage to act as a charge refiller for diamond when we performed photoemission in insulating conditions.
The sample holder is placed on a manipulator with five degrees of freedom (x,y,z, polar and azimuthal angle) able to move the sample from one chamber to the other. The principal displacement (i.e. the motion from one chamber to another) occurs along the x axis. The sample is transportable along a path of 600 mm, the position can be controlled remotely and is determined with an uncertainty of 0.01 mm. The position of the sample along the y and z axes can be determined with two rotating rules perpendicular to each other and to

the manipulator; they allow movements of 25 mm with an uncertainty of 0.005 mm. For what concern angular movements, the displacement on azimuthal angle is done manually and sample movement is possible, from the position of in which the sample is placed parallel to x axis, for angles ranging from -100 ° to +100°, with an uncertainty of 0.36°. The polar angle, on the other hand, is controlled remotely by calculator. The allowed rotation is 360° with uncertainty of 0.1°.
Finally, the manipulator is equipped with a heating system that allows to heat the samples up to temperatures of 700°C.

2.2.6 Oxygen production

For the production on atomic oxygen we expressly designed and realized a dedicated line able to introduce in chamber molecular oxygen and to dissociate into atomic oxygen by thermal activation; the line is sketched in Fig. 2.11.
Starting from a tank the molecular oxygen is introduced in the preparation chamber in a controlled way, using a leak valve; notice that during this operations the preparation chamber is separated from the measure chamber with a gate valve, in order to limit the quantity of oxygen used. To exclude the contamination of the gas in chamber, prior to start dissociation, we controlled gas composition with the quadrupole mass spectrometer.
The molecular oxygen is then dissociated into atomic oxygen using a hot tungsten filament in order to induce thermal dissociation: during this operation filament is placed at about 10 cm from the hydrogen-terminated sample.
Indeed, one of the main issue of using a filament to dissociate oxygen is, as reported in literature[61, 62], the possible presence of oxide species on the sample surface. Actually, we monitored with XPS spectroscopy the presence of oxide species both after the preliminary tests and after exposure to samples: we found the oxide contents to be below the detection limit in both cases.

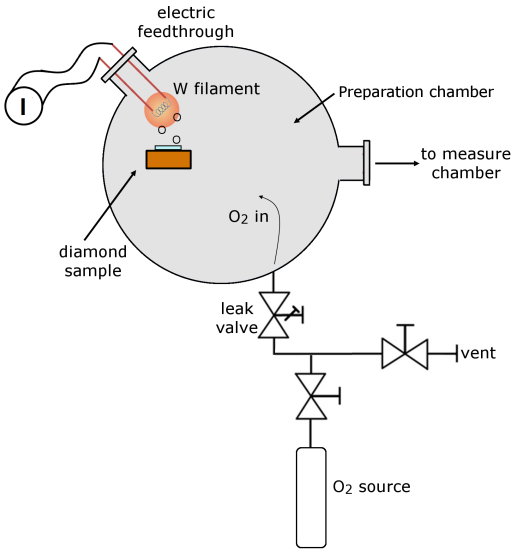

Figure 2.11: *Schematic of the oxygen line used to perform controlled exposure on sample. The line was specifically realized for this work.*

Chapter 3 Sample preparation, morphology and conductive properties

In this chapter we are going to show the investigations performed on hydrogen-terminated diamond samples regarding sample preparation, morphology and conductive properties. The chapter is divided as follows:

- First we introduce the main characteristics of the various sample used and the measurements performed on;
- Then, we discuss the differences in surface morphology for the sample used, investigated comparing AFM measurements;
- Then, we discuss the sample preparation that has been studied by comparing electron diffraction patterns taken for different prepared sample and in different phase of conductivity for the same sample;
- Finally, the attention will be moved on the resistance measurements we performed on samples.

3.1 Sample characteristics

For this work of thesis we used commercial available samples, produced by Element Six. Although all the samples used are ascribable to Type IIa diamonds, according to the classification proposed in Par. 1.1, samples are further divided into two different families, that, following the Element Six notation, are called respectively Standard and Electronic grade. Main differences between grades are described in table 3.1.

A number of samples were used to perform different measurements (all the

	Standard Grade	**Electronic Grade**
Single/Poly crystal	Single crystal	Single crystal
Lateral size	4.6×4.6 mm^2	4.6×4.6 mm^2
Thickness	500μm	500μm
Crystallographic Orientation of Surfaces	{100}	{100}
Surface roughness	< 10 nm	< 5 nm
Nitrogen concentration	< 1 ppm	< 5 ppb
Boron concentration	< 0.05 ppm	< 1 ppb
RT Electrons Mobility	1714 cm^{2}V^{-1}s^{-1}	2145 cm^{2}V^{-1}s^{-1}
RT Holes Mobility	2064 cm^{2}V^{-1}s^{-1}	2430 cm^{2}V^{-1}s^{-1}
Electrons saturation velocity	0.96×10^7 cm/s	0.98×10^7 cm/s
Holes saturation velocity	1.41×10^7 cm/s	1.54×10^7 cm/s

Table 3.1: *Main differences between Standard and Electronic grade diamond samples.*

combination used and measurements performed are summarized in table 3.2): samples are identified by a combination of letters and numbers. The letters indicate the different sample used and in particular the letter A and C identifies two Electronic Grade samples, while the letter B identifies a standard grade sample; the number associated instead indicates how many cycles of hydrogenation the samples have undergone, then with the number one we identify one hydrogenation (and cleaning) treatment, with the number two we identify samples that have undergone two cycles of hydrogenation and so on an so

forth. Not all the measurements performed on every sample will be showed: this chapter (and the next one, dedicated to spectroscopic analysis) will be a compendium of the principal observation taken during the investigation of these sample.

Sample	A1	A2	B1	B2	B3	C1	C2
Type	EG	EG	SG	SG	SG	EG	EG
Preparation	Cold	Cold	Cold	Cold	Hot	Hot	Hot
Electrical Measurements		✓			✓		✓
Resistance Mapping					✓		✓
AFM		✓		✓		✓	
LEED		✓				✓	
Spectroscopic Analysis	✓	✓	✓	✓	✓	✓	✓

Table 3.2: *Summary of the sample used in this work and measures performed on.*

3.2 Differences in morphology between Electronic and Standard Grade samples

As explained in the last section we worked with different commercial available sample, that are known to have different declared characteristics. In particular, samples indicated as Electronic Grade diamond are characterized by a lower roughness ($<$ 5nm) respect to the sample indicated as Standard Grade sample ($<$ 10nm). We investigated the differences in roughness and in surface morphology for the two sample types using AFM. The images, together with the sample height evolution, are presented in Fig.3.1: as can be seen from the figure Electronic Grade samples are characterized by the absence of any particular structure; variations in height are limited and the sample studied showed a roughness even better than declared ($\approx$1 nm).
Standard Grade sample instead is characterized by a pattern of square-shaped structures, with a size of 5$\times$5 μm and a height of 70-80 nm. Over these structures the roughness is $\approx$5 nm, even in this case better than declared.

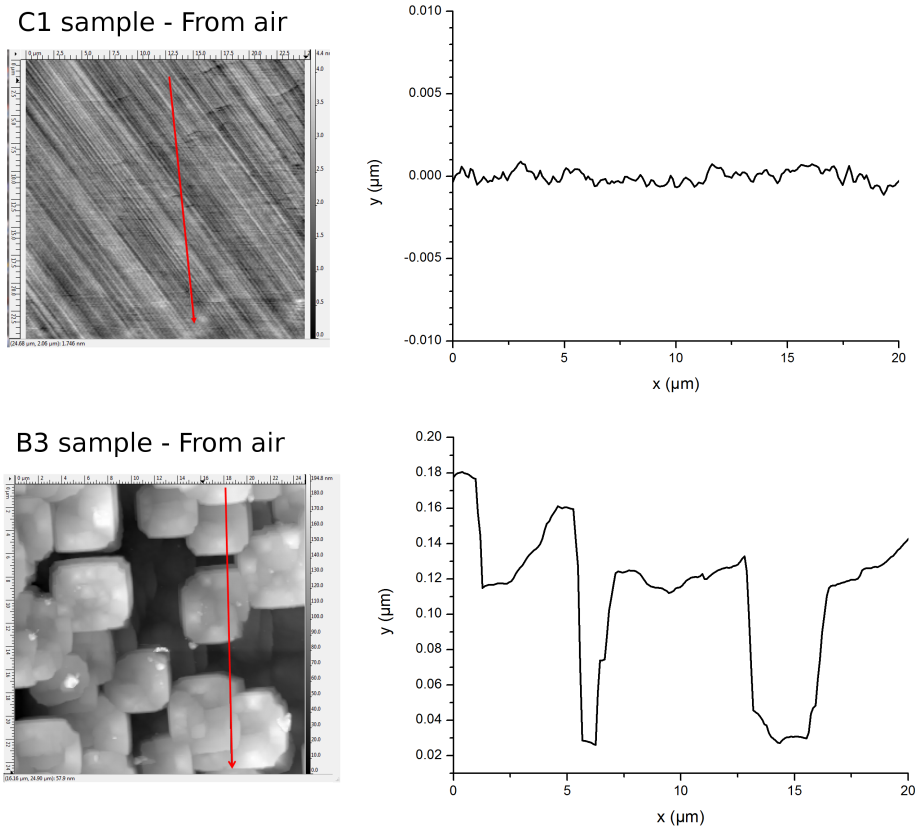

Figure 3.1: *25×25 μm^2 AFM image for an Electronic Grade (upper) and for a Standard Grade (lower) sample and their respective height evolution along the cut indicated in the image. Both samples have been studied in the conductive (from air) state.*

3.3 Electron diffraction patterns and sample preparation

Although the most used technique to hydrogenate diamond sample surface is the exposure to hydrogen plasma, several parameters can be varied during the treatment, including sample temperature, pressure and flow of hydrogen, and the microwave generator power. In particular we focused our attention on the sample temperature during the plasma hydrogenation. We take into account two opposite methods for sample preparation: the two methods, performed on the same sample, both started cleaning the surface with a boiling 1:1:1 solution of HNO_3, H_2SO_4 and $HClO_4$, in order to remove any unknown contaminant on the diamond surface and leaving the surface uniformly oxygen terminated. Then, the sample was exposed to hydrogen plasma: in one case (the "cold" preparation) it was not heated, in the other case (the "hot" preparation) the sample was heated up to 700°C. For hydrogen plasma we used the same working parameters in the two treatments: with a pressure of 40 mbar, and a microwave generator power of 1.2 kW, we exposed the sample for one hour. The two preparation have been studied with LEED and both showed a 2×1-1×2 reconstruction (an example of typical LEED pattern is shown in Fig. 3.2). The 2×1 reconstruction of the (100) surface is typical for hydrogen-terminated sample, differently from oxygen-terminated samples that have a 1x1 reconstruction[26, 28, 63–65]; the double reconstruction, i.e. the presence of a 2×1-1×2 pattern, can be related to the presence of multiple domains that were already seen studying CVD diamond[66].

Moreover, the two treatments have been compared on the basis of diffraction spectra, shown in Fig. 3.3. Referring to the pattern obtained, they are both characterized by more intense peaks at ± 2.43 Å^{-1} and ± 4.93 Å^{-1} and less intense peak at ± 1.23 Å^{-1} and ± 3.68 Å^{-1} (although in the case of cold prepared sample are hardly recognizable). Regarding peak positions, the two patterns are compatible with the 2×1 reconstruction of diamond surface (peak positions for the hot prepared sample and the parallel exchanged momentum for (100) reconstructed surface are compared in table 3.3).

Although the two preparation treatments both showed the 2×1 reconstruction it is also evident from the diffraction pattern that in the case of hot prepared sample the signal/noise ratio is higher than in the case of cold prepared sample: the pattern for the hot prepared sample did not show the characteristic

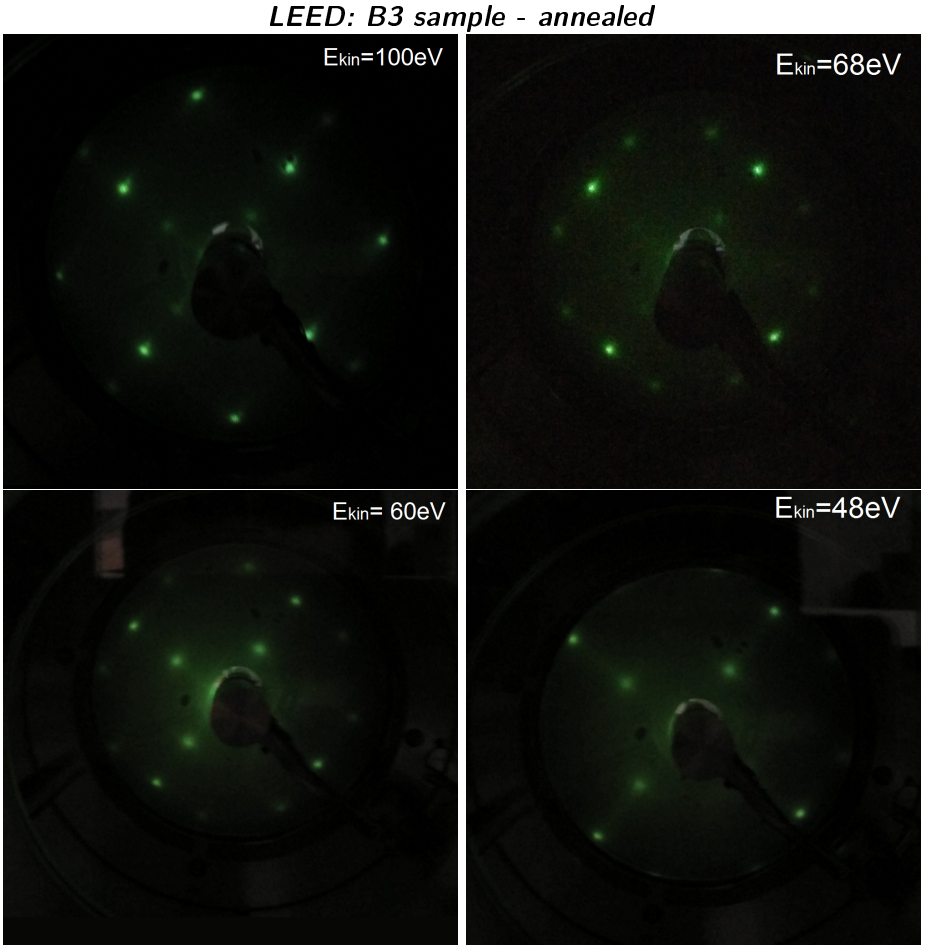

Figure 3.2: *LEED pattern for B3 conductive (i.e. from air) sample. The patterns have been taken at different energies. A 2×1-1×2 pattern can be noticed, revealing the presence of multiple domains on the surface. LEED patterns have been taken on non-conductive (i.e. annealed) sample.*

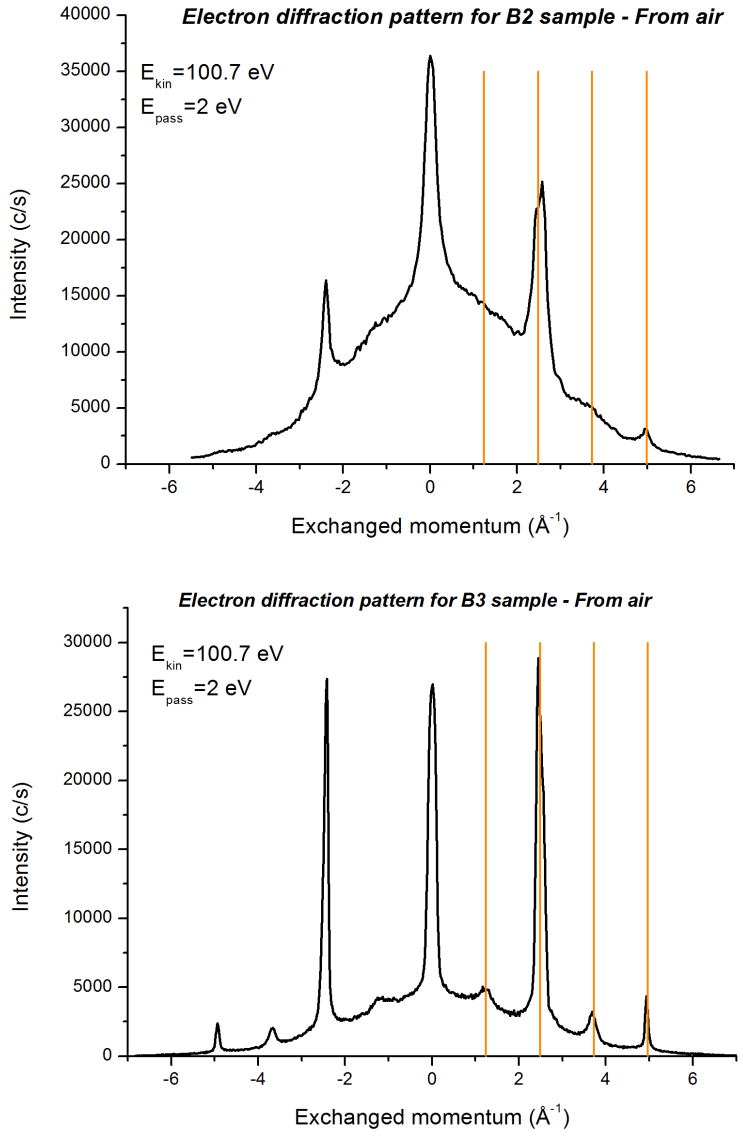

Figure 3.3: *Electron diffraction pattern obtained for two different hydrogen-plasma treatment. Upper image: H-plasma treatment with no sample heating; lower image: H-plasma treatment with sample heated up to 700° C. The orange lines correspond to the values of the exchanged momentum for the (100) reconstructed surface of diamond. The pattern have been taken with a 100 eV electron source on conductive (i.e. exposed to air) sample.*

Peak Position ($Å^{-1}$)	Exchang. moment. for (100) reconstr. surf. ($Å^{-1}$)
± 1.22	1.24
± 2.43	2.49
± 3.68	3.73
± 4.93	4.99

Table 3.3: *Comparison between peak location and the calculated parallel exchanged momentum for (100) diamond reconstructed surface.*

background presented by the pattern for the cold prepared sample while the peak intensities appeared higher; for the hot prepared sample we found also that the diffraction peaks appeared narrower (taking into account the peak at $0Å^{-1}$ we found a FWHM of $0.22Å^{-1}$ for the hot prepared sample and $0.30Å^{-1}$ for the cold prepared sample). We have interpreted these differences in diffraction pattern as a better long range order in the case of hot preparation than in the case of cold preparation.
The attention was then moved on the difference in patterns for the conductive and non-conductive sample: the non-conductive sample was obtained by annealing the surface at 450°C for one hour, in order to remove any conductive adsorbate: this temperature have been chosen because it is high enough to remove adsorbates using short time; nonetheless temperature must be under the desorption temperature of hydrogen that, from previous observations[37] starts at 700°C. The patterns for conductive and non-conductive case are shown in Fig. 3.4. Again, the studied sample is the same for both cases and it was prepared with the hot treatment: main difference between the two patterns is that pattern for the non-conductive case appears better defined, with a signal/noise ratio (i.e. the peak intensity respect to the background) that is improved if compared to the pattern taken from conductive case, while the 2×1 reconstruction remains unchanged, confirming that the temperature used for annealing is not enough to induce hydrogen desorbment from sample surface.
The improvement on the signal/noise ratio found in the pattern, as concluded in the comparison between hot and cold preparation, can be interpreted in terms of better long range order that an annealing of the sample, with removal

of airborne adsorbates and the reorganization of the surface, can induce.
At this stage we can also exclude any degradation of the sample under electron bombardment: this can be related to the current density of the electron gun (on the order of 10^{-11} A mm^{-2}) which can be not high enough to induce desorption of hydrogen from sample.

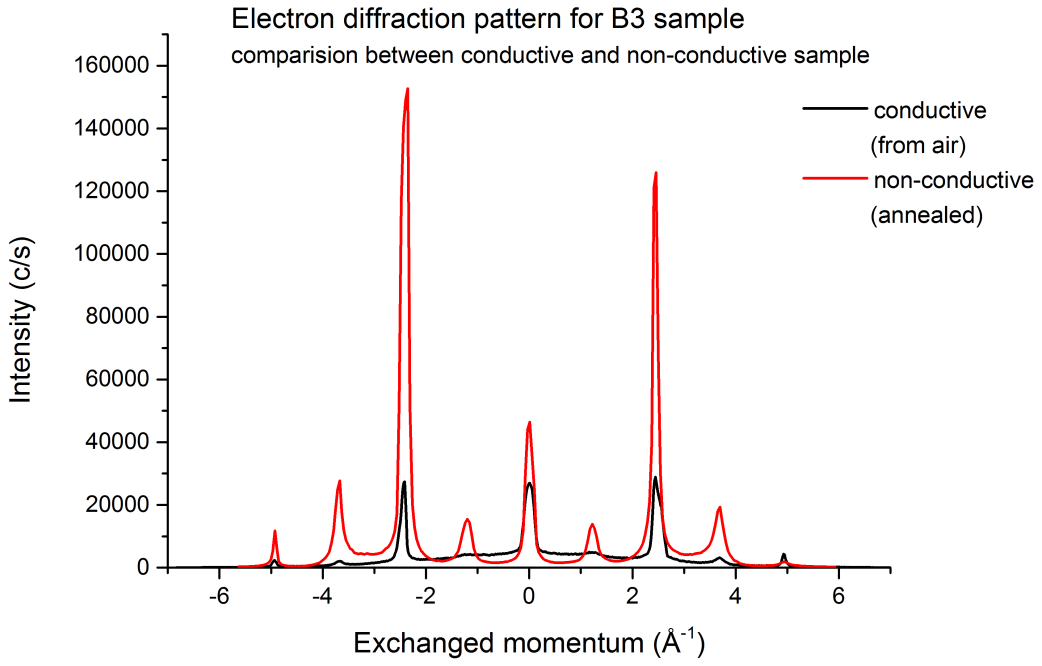

Figure 3.4: *Electron diffraction pattern obtained for conductive and non-conductive sample, prepared with sample heated up to 700°C. The pattern have been taken with a 100 eV electron source.*

3.4 Electric measurements

In this section we are going to show resistance measurement performed on hydrogenated sample. These measurements have been performed by using the two-probe measurements system, which provides the possibility to perform measurements as a function of pressure and temperature, as we have seen in section 2.2.2. The test shown was performed on an electronic grade sample

prepared with the hot preparation: the particular experimental system used to measure the samples provided the possibility to study three distinct conditions:

- Initially it was possible to study the samples as a function of chamber pressure, starting from atmospheric pressure towards base pressure of chamber (10^{-6} mbar);
- then we studied the evolution of resistance as a function of sample temperature up to 600°C. The low pressure in chamber prevented the immediate molecular adsorption on sample surface, allowing us to compare the behaviour of conductive and non-conductive (adsorbate free) sample;
- finally, in the last step we studied the resistance evolution during restoring the atmospheric conditions.

All the three measurement steps are shown in Fig. 3.5.

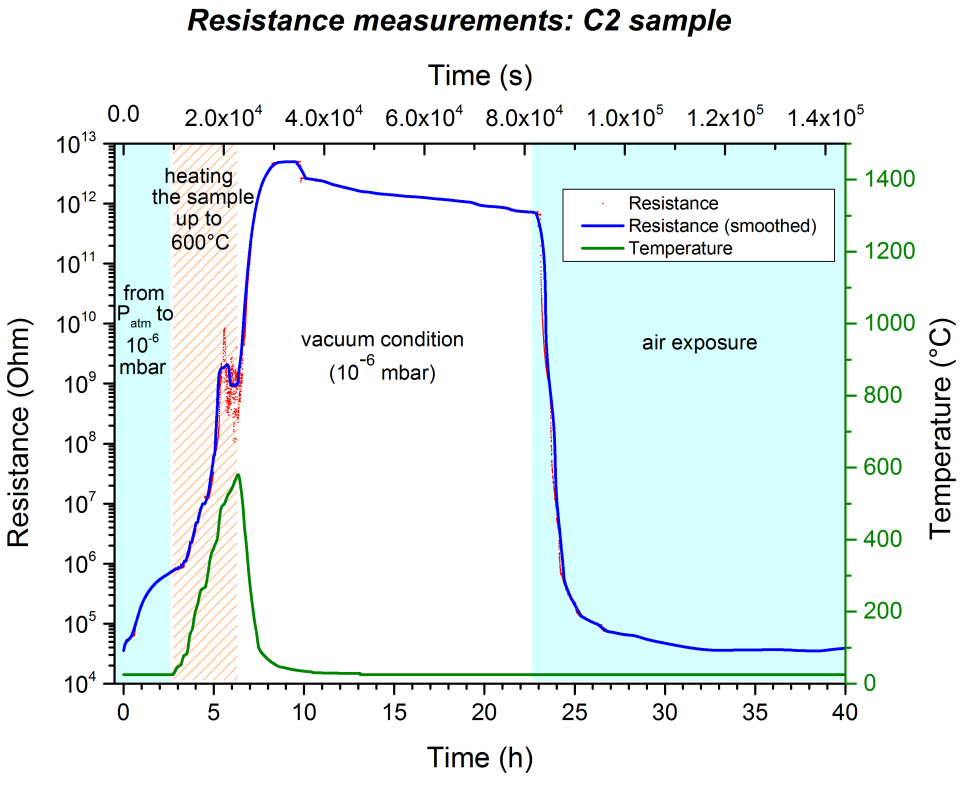

Figure 3.5: *Two point-probe resistance measured for the Electronic grade sample.*

- **From atmospheric pressure to 10^{-6} mbar:**
  The resistance evolution for an electronic grade sample is shown in detail in Fig. 3.6. It is interesting notice that the increasing of resistance accelerated both when the pre-vacuum system and the turbomolecular pump are turned on.
  In this phase the resistance increased by two order of magnitude respect

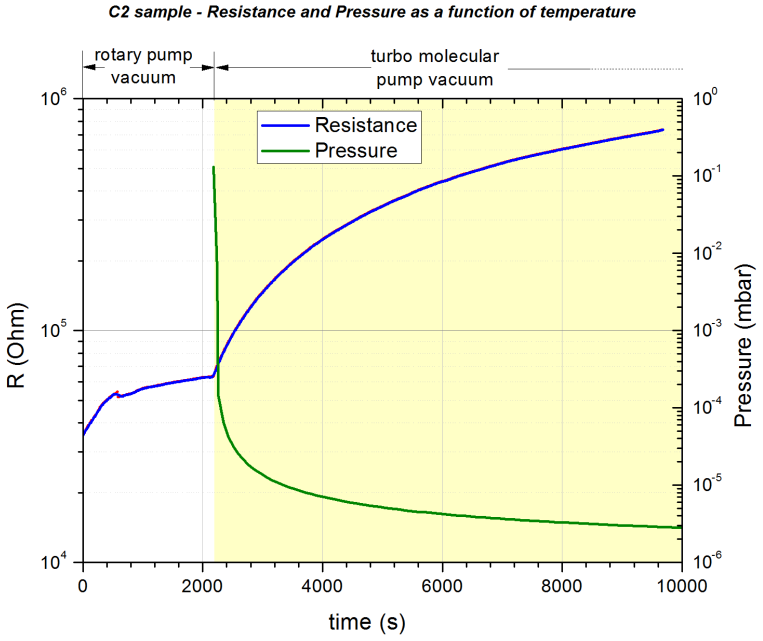

Figure 3.6: *Two point-probe resistance measured for the Electronic grade sample. In this phase the resistance is measured as a function of chamber pressure, from atmospheric conditions to* 10^{-6} *mbar.*

to the sample values measured in atmospheric condition. We believe that the increasing of resistance can be explained as follows: at atmospheric pressure airborne species continuously adsorb and desorb from the hydrogenated surface. The decreasing of the pressure due to the pump system alters this equilibrium, so that the number of desorbed species will be higher than the number of adsorbed species, causing an increase of the resistance.
This increase is observable until the base pressure of the chamber is reached; at that point a new equilibrium situation will prevail; the number of active species, present as residual gases in the chamber, will be

less than at atmospheric pressure and, consequently, the resistance will be higher.

- **Resistance measurements as a function of temperature:**
  After the base pressure in the chamber was reached we performed resistance measurements as a function of temperature, as mentioned, up to 600°C. It can be noticed from Fig. 3.7, in which this phase is shown in detail, that is possible to distinguish two behaviours: initially, and up to about 500°C, resistance increases as temperature increases (behaviour compatible with progressive desorption of atmospheric molecules); resistance increasing is about 3 orders of magnitude respect to the room temperature value.
  Then, beyond 500°C, resistance progressively decreases while temperature increases, falling below 10^9 Ω: the nature of this observation will be discussed later.

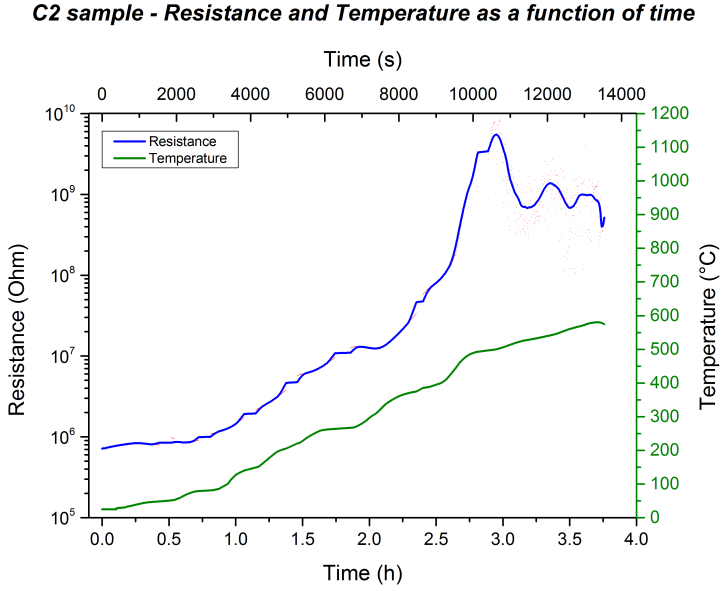

Figure 3.7: *Two point-probe resistance measured for the electronic grade sample. In this phase the resistance is measured as a function of chamber temperature, from room temperature to 600° C.*

- **Restoring atmospheric condition:**
  Once the sample was exposed again to air, its resistance keeled over almost instantly, decreasing down to 10^5 Ω (seven orders of magnitude lower than non-conductive value) in about 2000 seconds (or about 30 minutes) before returning to initial values after approximately 14 hours, with a total difference between conductive and non-conductive state of eight orders of magnitude, greater than the one observed by Maier in his work[8].

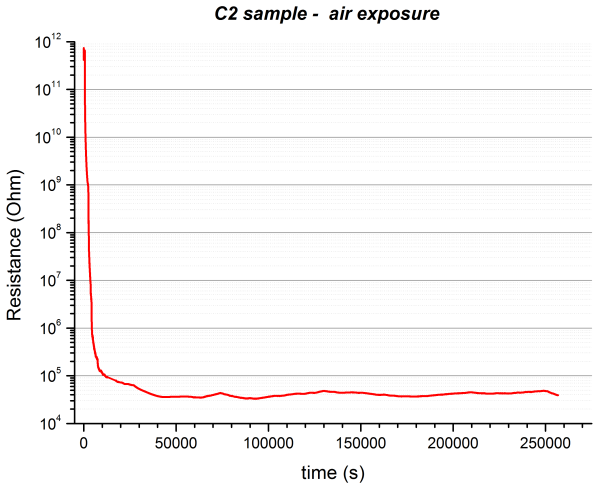

Figure 3.8: *Two point-probe resistance measured for the electronic grade sample. In this phase the resistance is measured while the sample is exposed to air.*

The resistance measurements were similarly performed on a standard grade sample and are presented in Fig. 3.9.
Starting from a value of about 10^6 Ω, one order of magnitude higher respect to the electron grade sample, the general behaviour of resistance appears similar if compared with the electronic grade case. Indeed, some variations are observable: the resistance difference between conductive and non-conductive sample (i.e. sample annealed at at temperature of 600°) appeared less pronounced: in this case the difference measured is about seven orders of magnitude (with the resistance value, for the non-conductive case , of about 10^{13} Ω).
Different is also the resistance behaviour once the atmospheric condition are restored: if in the case of electronic grade sample are necessary 2000s (about

half an hour) to return to the initial value for resistance, in this case, after two hour the resistance is still two orders of magnitude higher than the initial value.

For what concern resistance measurements as a function of temperature we

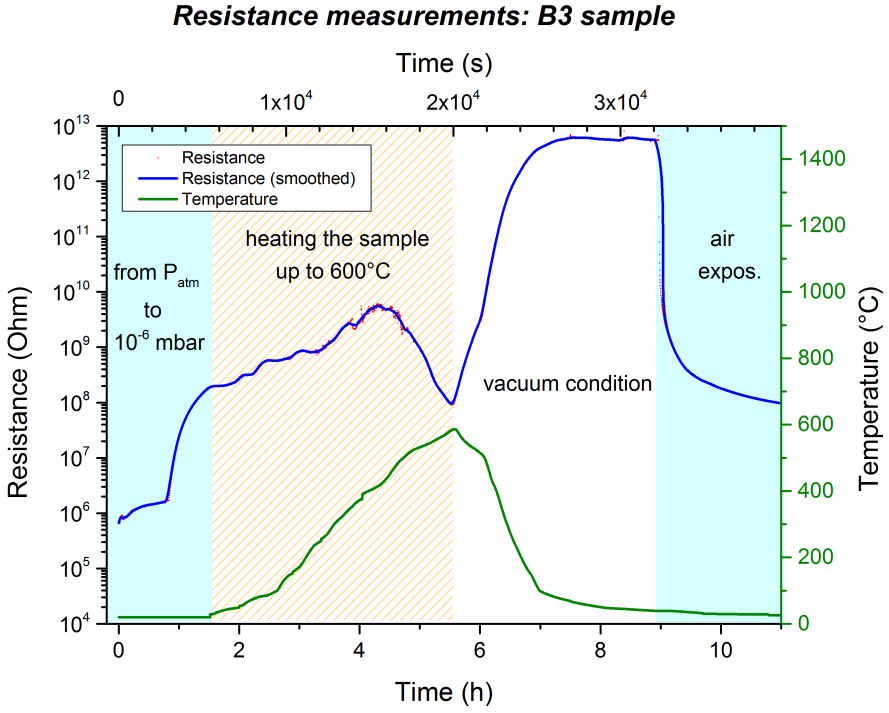

Figure 3.9: *Two point-probe resistance measured for the standard grade sample.*

observe, as in the case of electronic sample, a double behaviour: up to 500°C the resistance showed an increasing as a function of temperature (even in this case correlated to the progressive desorption of active molecules). Beyond 500°C the resistance started to decrease, and the decreasing is even higher respect to the electronic grade case: while the resistance of electronic grade sample decrease from 10^{10} Ω to 10^{9} Ω, in the case of standard grade sample, although starting again from a resistance value of about 10^{10} Ω, the resistance finally reached a value of about 10^{8} Ω.

This behaviour, for both electronic and standard grade samples, can be explained as follows: while initially (i.e. at lower temperature) surface resistance is dominant, the progressive increasing of temperature causes not only the progressive desorption of adsorbates, but also the concomitant decreasing of bulk

resistance, typical for semiconductors, that beyond 500°C becomes dominant. Since the bulk resistance scales as $\exp\{-E_A/KT\}$, where E_A is the activation energy, it is then possible to estimate E_A studying how the resistance varies as a function of temperature. An attempt in that sense was performed for both electronic and standard grade samples, and it is shown in Fig. 3.10.
For both samples the resistance is characterized by two activation energies, though different in values depending on the sample: the fits performed on electronic grade sample gives the values of 0.21 eV and 0.7 eV, while, for the standard grade sample, the activation energies found are 0.15eV and 2.5 eV.
For what concern activation energies of 0.15 and 0.21eV found for the two samples, both can be correlated to the presence of defects, introducing shallow levels[3]; a similar consideration has been carried out for the activation energy of 0.7eV [67]; finally, the activation energy of 2.5 eV can be correlated to an energy state in the middle of the band gap, or to the activation energy for vacancies in type IIb diamond[68]. In all cases, however, further analysis are needed in order to obtain the correct estimation for the activation energies.

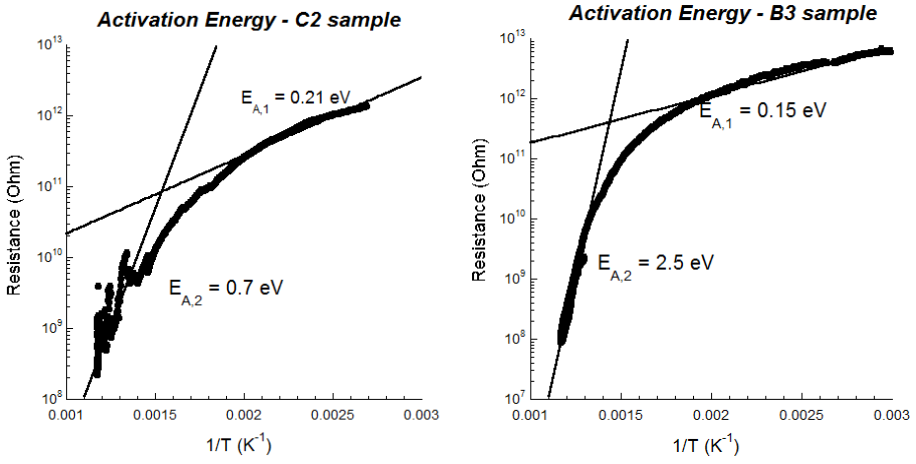

Figure 3.10: *Estimation of activation energy for the electronic grade (upper image) and for the standard grade (lower image) samples, from the evolution of resistance as a function of 1/T. Both samples shows two activation energies.*

3.5 EELS measurements

Once the electrical tests were performed we made further investigation focusing on sample homogeneity, in terms of hydrogen surface terminations, performed using electron energy loss spectroscopy. A typical investigation started probing the sample as function of the position with electron gun and acquiring the elastically scattered electron in specular configuration, in a kind of electron reflectivity measurement: the idea is that zones terminated differently (or with different amount of adsorbates) will have different reflectivity, as in Fig. 3.11 is reported.

From the pattern presented, related to a non-conductive (and so adsorbate-

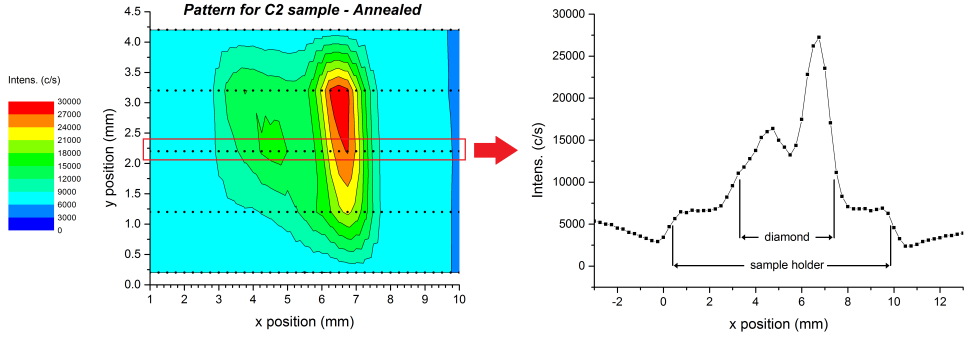

Figure 3.11: *Left image: electron reflectivity pattern, taken by impinging electron on sample surface and acquiring only the elastically scattered electrons. Right image: a detail of a reflectivity scan where is possible to recognize two reflectivity zone of the sample; the taken scan is the one highlighted in red in the upper image. The pattern has been taken on a conductive (i.e. exposed to air) sample.*

free) sample, it is possible to recognize two zones of reflectivity on the sample: the high reflectivity zone has about twice the counts of the area with low reflectivity.

A similar investigation has been performed, on the same sample, using the four-probe resistance method, and it is reported in Fig. 3.12.

Emphasizing that is the first time that spectroscopic and resistance pattern are measured on the same sample, we found that, similar to the electron reflectivity pattern, in the resistance pattern is possible to recognize two zones: the difference between the zone with higher and the zone with lower resistance is roughly of one order of magnitude.

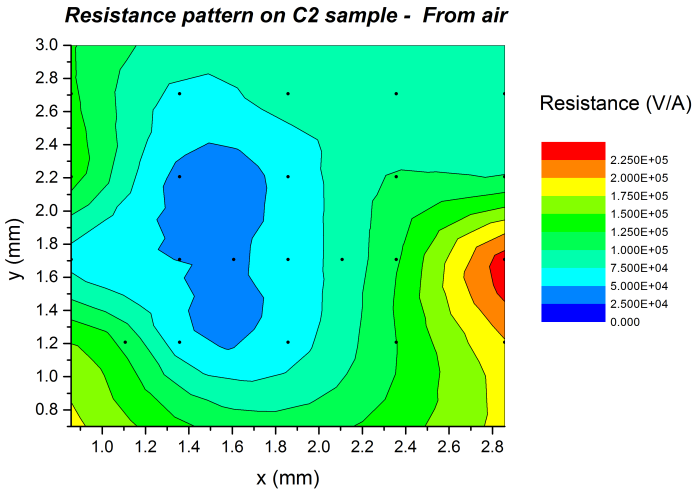

Figure 3.12: *Resistance pattern obtained with four-probe measurements as a function of position on sample.*

Since the orientation of the sample is the same for the two patterns shown in Figs. 3.11 and 3.12, it is possible to notice a correspondence between the number of electron reflected and the value of resistance: the more the electron reflected, the higher the resistance measured.
To explain why the sample is characterized by zones with different electron reflectivity and to understand why these zones showed also different resistance values we then performed EELS measurements; the spectra are presented in Fig. 3.13.

The spectra presented in figure show similar behaviour in the 5-50 eV loss region where, as already described in chapter I, are present typical feature of diamond, located at 14, 23 and 33 eV. These feature are related, respectively, to a transition from valence to conduction band [29], and to surface and bulk plasmons[26, 29, 30, 69, 70].
The main differences in the presented spectra, instead, are located in the 0-5 eV loss region: the spectrum taken in the lower reflective side of the sample is in fact characterized by the presence of a gap in this region, gap that is lost in the spectrum relative in the higher reflective side of the sample.
As remarked in chapter one, the 0-5 eV loss region represent a benchmark for the surface termination of diamond. Previous literature[26] showed, in

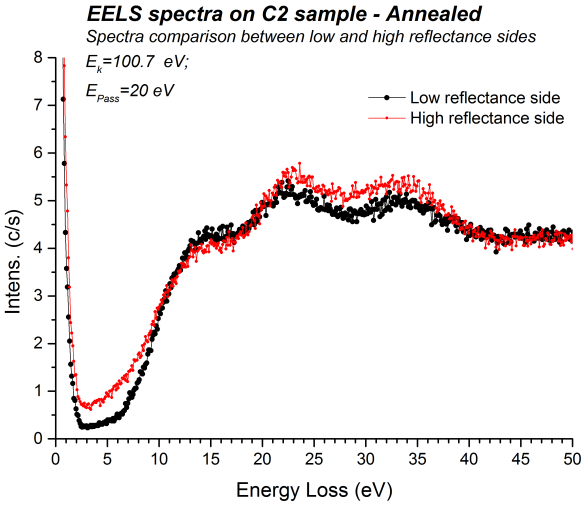

Figure 3.13: *Electron energy loss spectra taken on different zones of the sample, characterized by different electron reflectivity. The spectra have been taken with a source of 100.7 eV and a pass energy of 2 eV.*

fact, that Energy Loss of well-hydrogenated spectra are characterized by the presence of a gap, in this region, while spectra taken for bare surface is characterized by the presence of a large feature (and so no gap is present). By the comparison of spectra shown in Fig. 3.13 and literature we can conclude that spectra taken in the lower reflective side are more similar to the spectra presented in literature for the well hydrogenated surface respect to the spectra taken in the higher reflective zone, that are more similar to the spectra for bare surface, although we are not able to resolve surface state.
This means that with energy loss spectra we are revealing the presence of zones on the sample that are not well hydrogenated or, even, bare.

Summarizing, we compared the electron reflectivity pattern and the resistance pattern: we found that the zones of the sample characterized by lower reflectivity were also characterized by lower resistance; the distribution of these zones was not random but follows a precise gradient (as can be seen in Figs. 3.11 and 3.12).
To justify the differences seen in the electron reflectivity pattern we performed EELS measurements both in the zones of lower and higher reflectivity: by the

comparison of spectra we found that the zones characterized by lower electron reflectivity were also the zones of the sample better hydrogenated (it is then reasonable that zones characterized to be less reflective showed also lower resistance: hydrogenation is a necessary requirement for the surface conduction). A possible explanation about the non-uniform hydrogenation of sample can be related to the sample placement (done manually) during the hydrogenation treatment and the relative position respect to hydrogen plasma. It is possible that sample may not be symmetrically placed under the hydrogen plasma; if it occurs the zones of the samples closer to hydrogen plasma have more chance to be hydrogenated in a better way respect to the further away: this leaves open questions on reliability and reproducibility of samples, but, at the same time, we have proposed a powerful technique to verify hydrogen surface homogeneity.

Chapter 4 Spectroscopic analysis

This chapter is dedicated to the spectroscopic analysis we performed on hydrogenated diamond samples. The chapter is divided as follows:

- First we are going to show X-ray photoemission (XPS) measurements: the investigation involved different conductivity states and different exposures (i.e. to air and to atomic oxygen);
- Then we will move our attention to the investigation of C-H stretching mode, done by Energy Loss (EELS) measurements.

As shown in table 3.2, spectroscopic analysis has been performed on different samples, prepared in different ways: as in the case of the measurements shown in Chapter 3 we will not discuss all the spectra taken for all samples but we will highlight the principal observations taken during the investigation of these samples.

4.1 XPS measurements

In this section we are going to show measurements performed by X-Ray Photoemission Spectroscopy. As said in the introduction of the chapter we performed measurements for different conductivity states: initially we will discuss the data taken for a non-conductive sample, i.e. the sample that has been annealed in order to remove any adsorbate responsible of surface conductivity; the deconvolution of the main core level peaks will be also discussed.
Then, the analysis of XPS spectra will be extended to the air-exposed (conductive) surface and we will compare between the non conductive (annealed) and the non conductive (air exposed) cases. In the last section we will focus on the oxygen-exposed surface, pointing out the differences between the oxygen and the air exposure.

4.1.1 The non-conductive case and spectra deconvolution

In the non-conductive case the active adsorbates, responsible of conduction on diamond surface, are removed by annealing the sample for one hour at a temperature of 450 °C.
The analysis of core level spectra starts from the individuation of the principal signals (and so the principal elements) on the diamond surface. This is typically made by a survey like the one presented in Fig. 4.1. From the survey

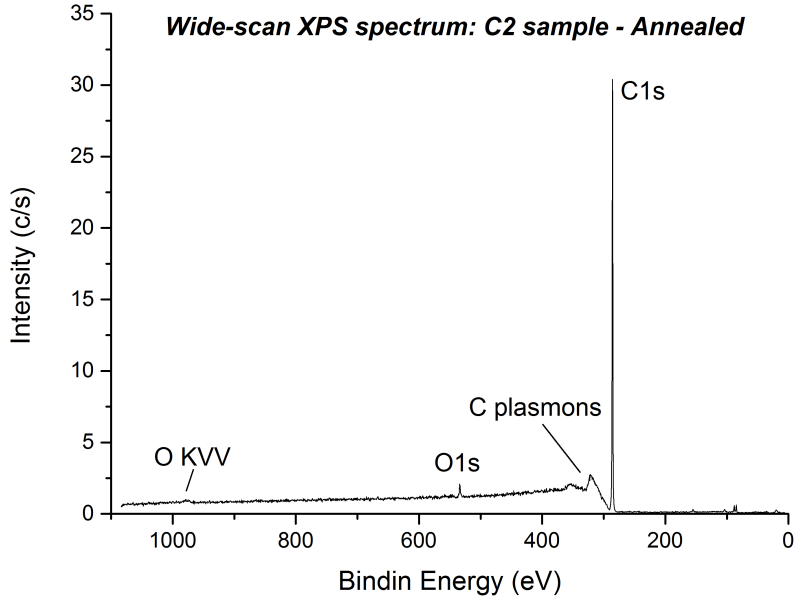

Figure 4.1: *XPS survey on a hydrogen-terminated diamond sample. It is possible to recognize photoemission peaks related to C1s core level (at a binding energy of about 286 eV) and O1s core level (about 530 eV). Spectra have been taken with a $Al_{k\alpha}$ source (1486.7 eV) and a pass Energy of 40 eV. The resolution is 450meV.*

presented it is possible to identify some structures; the most intense are the C1s core level (at a binding energy of about 286 eV), the O1s core level (530eV) while other visible structures are located at 318 and 350 eV, that are assigned to C plasmons[28, 71], and a small bump at 978 eV that we assigned to oxygen KVV Auger.
The presence of oxygen in the spectrum after the annealing treatment was unexpected: the annealing treatment was in fact devoted to remove any adsorbed molecules (in principle the main reasonable source of oxygen in the spectrum)

from the surface. Three are the possible causes that can explain the observation of oxygen: (a) the oxygen is still physisorbed on the surface; (b) oxygen is strongly bonded (i.e. chemisorbed) on diamond surface; (c) Oxygen is present as impurity in the diamond lattice.
We can exclude the case (a) because further annealing treatments (even at higher temperatures) are not effective to decrease the oxygen amount.
Further analysis of spectra, done as a function of collection angle and presented below in section 4.1.2 convinced us of the surface origin of oxygen, excluding the possibility that it is present as impurities in the lattice.
At this stage it is then possible to estimate the fraction of the surface covered by oxygen. Using the Fadley model, presented in Par. 2.1.4, considering an inelastic mean free path of 19 Å[72], the O1s peak as overlayer signal and C1s peak as substrate signal, we calculate a fraction of 33±3% of diamond surface covered by oxygen.
We now move the discussion on C1s and O1s core level spectra, seen in detail: the C1s lineshape is structureless, but a bump is distinguishable towards higher binding energy (like earlier C1s spectra for hydrogen-terminated diamond showed [37]) while the O1s lineshape is characterized by an almost symmetrical structure with a FWHM of 1.5 eV. The two spectra are presented in Figs. 4.2 and 4.3.

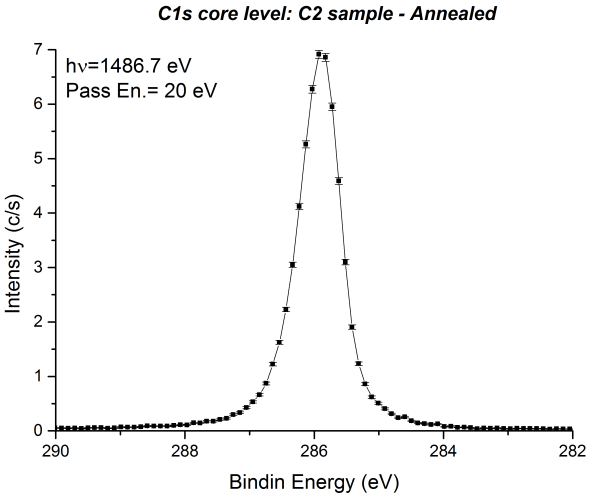

Figure 4.2: *C1s core level for the non-conductive sample. The spectrum has been taken with a $Al_{k\alpha}$ source and a pass energy of 20 eV. The resolution is 350 meV.*

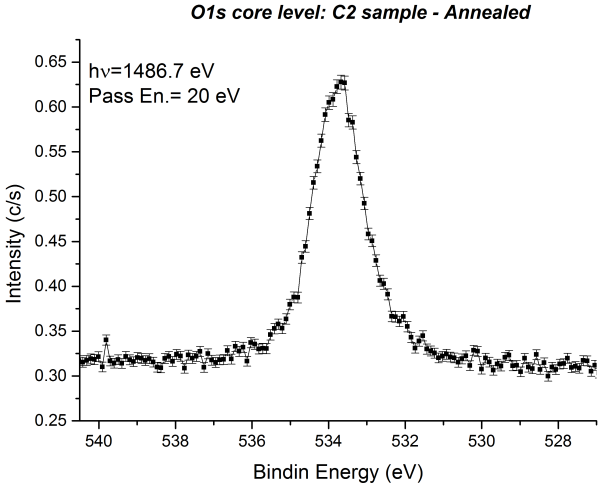

Figure 4.3: *O1s core level for the non-conductive sample. The spectrum has been taken with a $Al_{k\alpha}$ source and a pass energy of 20 eV. The resolution is 350 meV.*

It is clear now that, in order to obtain more significant information from the two core levels, a deconvolution of the lineshapes is needed.
The deconvolution of C1s core level has been done by taking into account previous literature on matter. Previous deconvolution of C1s spectra for hydrogen-terminated diamond, as described in Par. 1.3, presents two variants: in the model proposed by Graupner and coworkers[37], near to the bulk component, a surface component related to hydrogen is shifted by 0.5 eV towards higher binding energies; in the second model, proposed by Schenk and coworkers [40], near to the bulk component, a peak related to the subsurface carbon layer is present, shifted by 0.36 eV towards higher binding energies respect to the bulk component. In this case the component related to hydrogen termination of the surface is shifted, respect to bulk component, by 0.16 eV towards lower binding energy but with our setup we are unable to resolve it. Moreover, previous deconvolutions does not take into account the possible presence of chemisorbed oxygen on diamond surface; in our case, instead, we forcedly introduced oxygen-related component in the fit, relying on previous XPS works on oxygen-terminated diamond[73, 74].
The deconvolution has been done by using Voigt profiles (for which we used a fixed Lorentzian width of 0.15 eV, as done in previous cases [37, 40, 73, 75]) and a Shirley background; the peak assignment is the following:

- C_b peak is correlated to bulk carbon in sp^3 configuration;
- C_c peak is assigned to surface carbon not bonded with hydrogen and defects; as seen in [37] the peak is shifted by -0.9 eV with respect to the bulk component;
- C_{O1} and C_{O2} are related to carbon bonded to oxygen in different ways: C_{O1} is related to single bonded carbon (i.e. C–O, C–OH) and it is shifted by 1.2 eV respect to the bulk component while the C_{O2} peak is related to double bonded carbon (i.e. C=O or O-C-O) and is shifted by 2.5 eV respect to the bulk components.

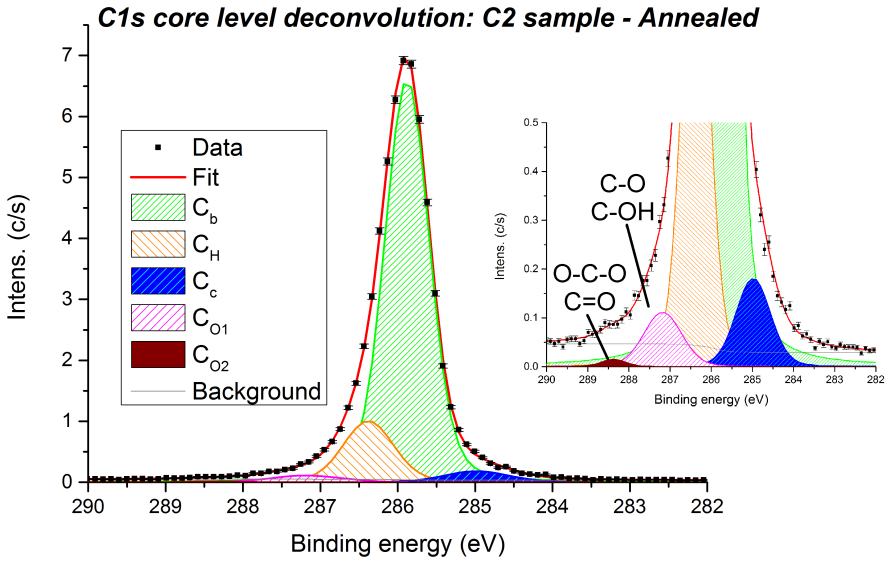

Figure 4.4: *Final deconvolution of C1s core level spectra. The peak are so assigned: C_b is relative to bulk component, C_c is due to surface carbon not bonded with hydrogen and defects, C_H has been assigned to carbon bonded with hydrogen both in the surface and in the subsurface region (the details of assignment can be found in text) C_{O1} and C_{O2} are due to oxygen-bonded carbon (the respective bonds are shown in the insight on the right).*

Fit component	Posit.(eV)	Ampl.	GW	LW
C_b	285.9	5.18	0.59	0.15
C_H	286.4	0.89	0.69	0.15
C_c	285	0.20	0.92	0.15
C_{O1}	287.2	0.14	1.00	0.15
C_{O2}	288.4	0.01	0.66	0.15

Table 4.1: *Fit values of C1s core level spectra for the annealed sample. For every component the position in energy, the amplitude, the gaussian (GW) and the lorentzian (LW) parameter are shown. The lorentzian parameter was fixed at 0.15 eV according to ref.[37].*

A separate discussion is needed for the peak location and relative assignment of the C_H component indicated in Fig. 4.4: in order to assign this component to and hydrogen component as proposed by Graupner or to surface carbon as proposed by Schenk we tested the two models to fit C1s core level with the following method:

1. A component of the fit has been moved in the higher binding energy zone respect to the bulk component with a shift in the range between 0.3 and 1 eV, with a step of 0.05 eV;

2. for each step we calculate:

   - the coverage related to this (unassigned) component. For the estimation we used the Fadley model proposed in Par. 2.1.4, in which we use the unassigned component in the C1s spectra as overlayer signal and the C_b component as substrate signal; we refer to this as H-related coverage;
   - the oxygen coverage. For the estimation we used again the Fadley model, in which we use the sum of oxygen-related component in the C1s spectra as overlayer signal and the C_b component as substrate signal; we refer to this as O-related coverage;

3. the results have been compared on the basis of chi-squared (χ^2) test value, the oxygen estimated coverage (remembering that from the comparison of O1s and C1s peaks we found a fraction of diamond surface covered by oxygen of 33±3%) and the coverage estimated by the C_H component: depending on the model, we expect different values of coverage; for the model proposed by Graupner and coworkers, we in fact expect a coverage that has to be around 70%, considering that hydrogen is located only in the surface region and that a portion of the sample is covered by oxygen; differently for the model proposed by Schenk and coworkers we expect a coverage around 100% because of the subsurface nature of the assignment.

The results are presented in table 4.2, where the χ^2 value is shown in the reduced form.

Shift (eV)	χ^2	H coverage (%)	O coverage (%)	O coverage estim. from O1s (%)
0.300	1.101	443±46	36±4	33±3
0.360	1.123	337±35	34±4	
0.400	1.130	284±29	33±4	
0.450	1.137	229±23	32±3	
0.500	1.150	189±19	31±3	
0.550	1.177	145±15	30±3	
0.600	1.231	115±12	29±3	
0.650	1.334	91±9	28±3	
0.700	1.505	74±8	31±3	
0.750	1.707	72±8	25±3	
0.800	2.045	55±6	24±3	
0.850	2.387	49±6	22±3	
0.900	2.773	45±5	21±3	

Table 4.2: *In table is represented the energy shift value between the bulk component in the fit (C_b) and the unassigned C_H component; for every value a chi-squared value, coverage of unassigned component and oxygen coverage by O-related components in C1s have been calculated. For comparison, we also estimated oxygen coverage using O1s signal.*

As can be seen from the table, the χ^2 value remains acceptably low in the in 0.3-0.6 eV shift region: in this region, however, the estimated coverage results always over the monolayer coverage and it increases if the shift between C_b and C_H is reduced: this does not indicate which of the two models is better than the other and, moreover, estimated coverages for the unassigned component appear to be incompatible with expected values for both proposed model.
There are different ways to interpret this observation: one way is to consider that C_H peaks may contain a contribute from other structures: in some cases, in fact, a peak correlated to surface carbon bonded with OH has been used in the deconvolution of C1s peak[76–78]. This case is discussed in Appendix A: the introduction of another peak does not seem to be fully justified.
More promising, instead, is the explanation suggested by a consideration: actually, the two models do not takes into account the possibility that hydro-

genation of the surface with aggressive techniques (as plasma exposure is) may leave hydrogen atoms not only on the surface of the sample but even deeper, inside the first layers of the diamond lattice.
To support this hypothesis we performed Montecarlo simulation of the hydrogen plasma exposure of diamond surface: we described the exposure as collisions of hydrogen particles accelerated by an (equivalent) potential difference respect to sample surface, in order to evaluate the penetration depth of hydrogen ions. Since hydrogen atoms, in principle, impinge on the surface randomly, we take into account two extreme plasma directions, considering the case of normal implantation and implantation with an angle of 45° of incidence. We also consider different ion energies: according to [79] typical plasma potential does not exceed 800V: thus, we simulated the cases in which the potential difference between plasma and sample surface was 100, 500 and 800V, respectively. The simulations are presented in Figs. 4.5, 4.6 and 4.7.

For what concern plasma direction, at low energies it seems to be not effective in terms of penetration depth: taking as example the simulation for 100V of plasma potential we have a difference of only few angstroms between a diffusion normal respect to the surface or with an angle of 45° respect to the normal (20 and 17 Å, respectively). More differences can be found by increasing the plasma potential: at 500V, in fact, we found a penetration depth of 68 Å for normal implantation and 56 Å for implantation at 45°; at 800V the difference is even more significative (100 vs 80 Å of depth, respectively in the case of normal direction or 45° respect to the normal). We may conclude that the simulations shown suggest the possible diffusion of hydrogen inside diamond crystal; at the same time, however, we have to point out that at this stage we are not able to determine the exact value of the potential difference between hydrogen plasma and sample surface, and where is located in the 0-800V range, for our case: an indication about in this sense may come from the measurements performed as a function of angle, showed later.
Concluding, the calculation of coverage for the hydrogen-related component and the Montecarlo simulation both suggest that C_H component used in fit cannot be related only to a surface component, as proposed by Graupner and coworkers. Thus, two are the possible origin for the component:

- C_H may be related only to carbon atoms bonded with hydrogen (maybe forming hydrocarbon chains, as proposed by Graupner) located in the

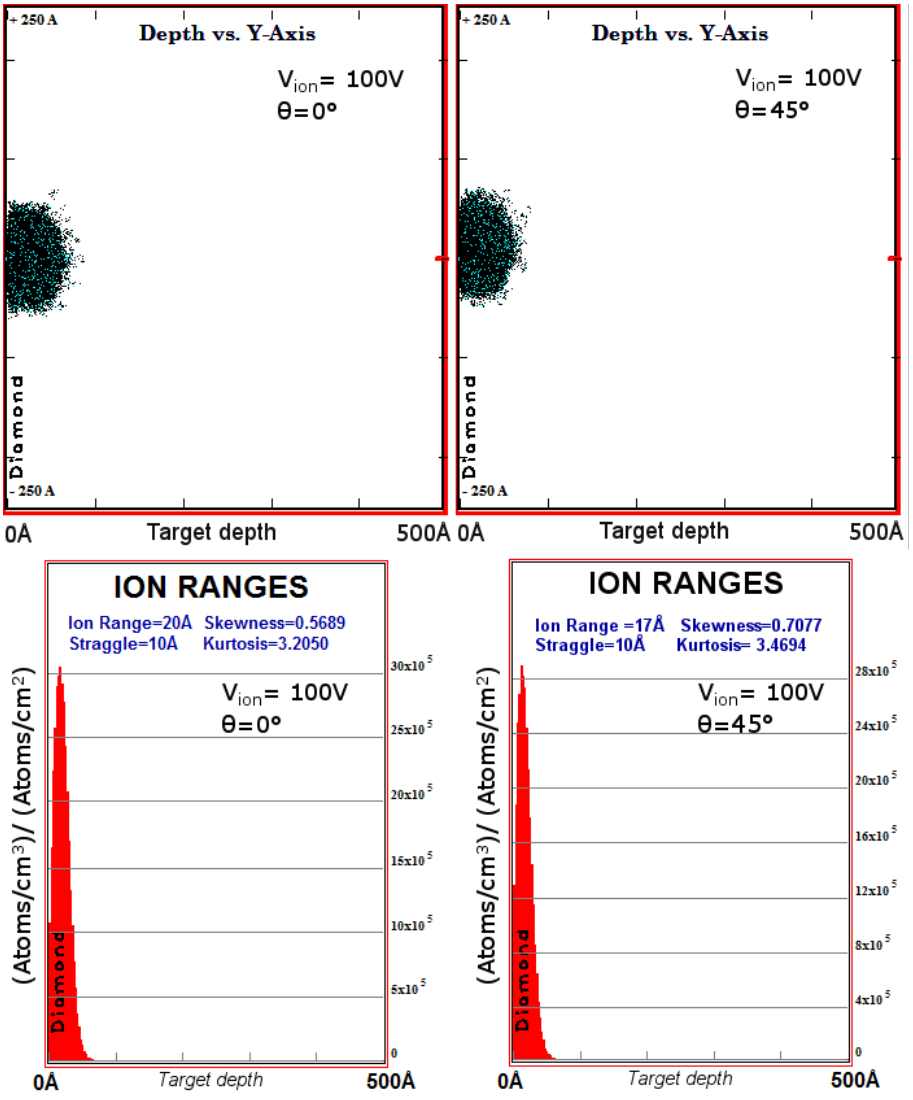

Figure 4.5: *Evaluation of penetration depth for hydrogen atoms on diamond sample during plasma exposure. The simulations take into account different direction of diffusion (0 and 45° respect to the surface normal) and for a plasma potential of 100V.*

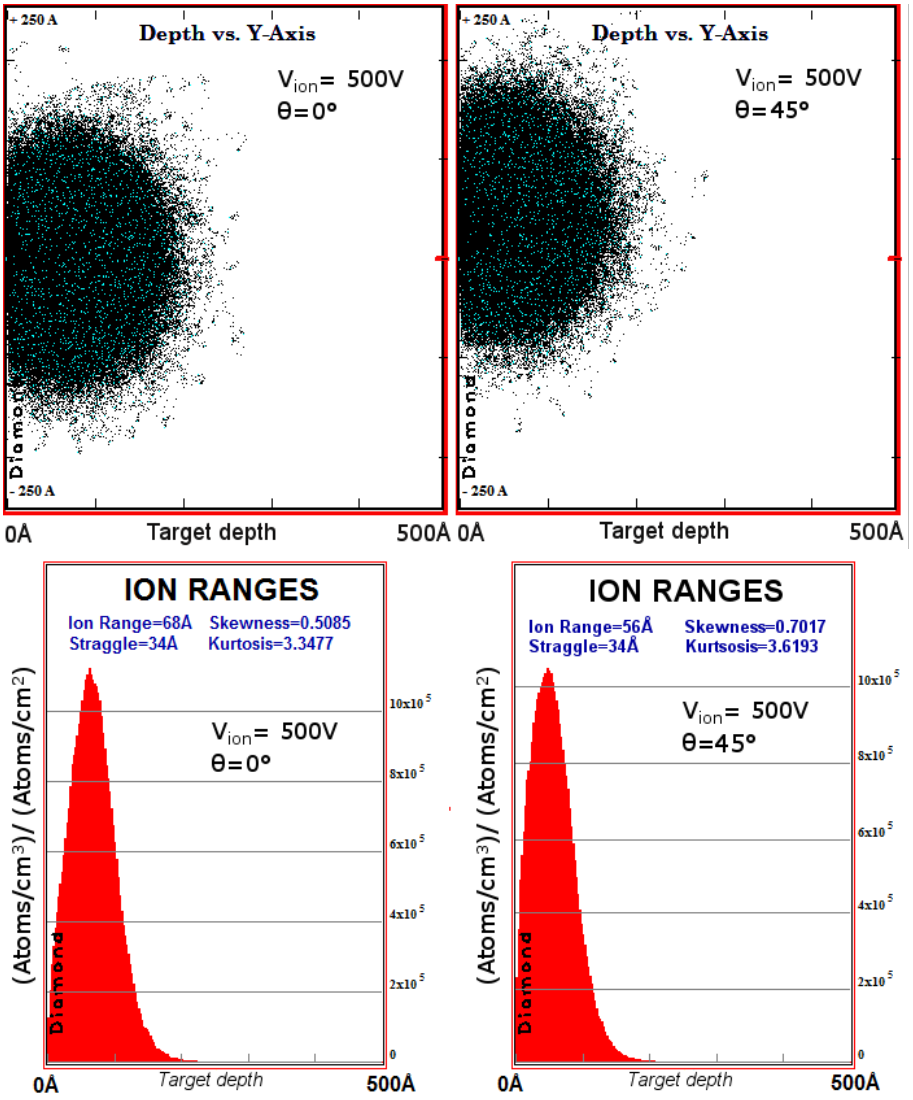

Figure 4.6: *Evaluation of penetration depth for hydrogen atoms on diamond sample during plasma exposure. The simulations take into account different direction of diffusion (0 and 45° respect to the surface normal) and for a plasma potential of 500V.*

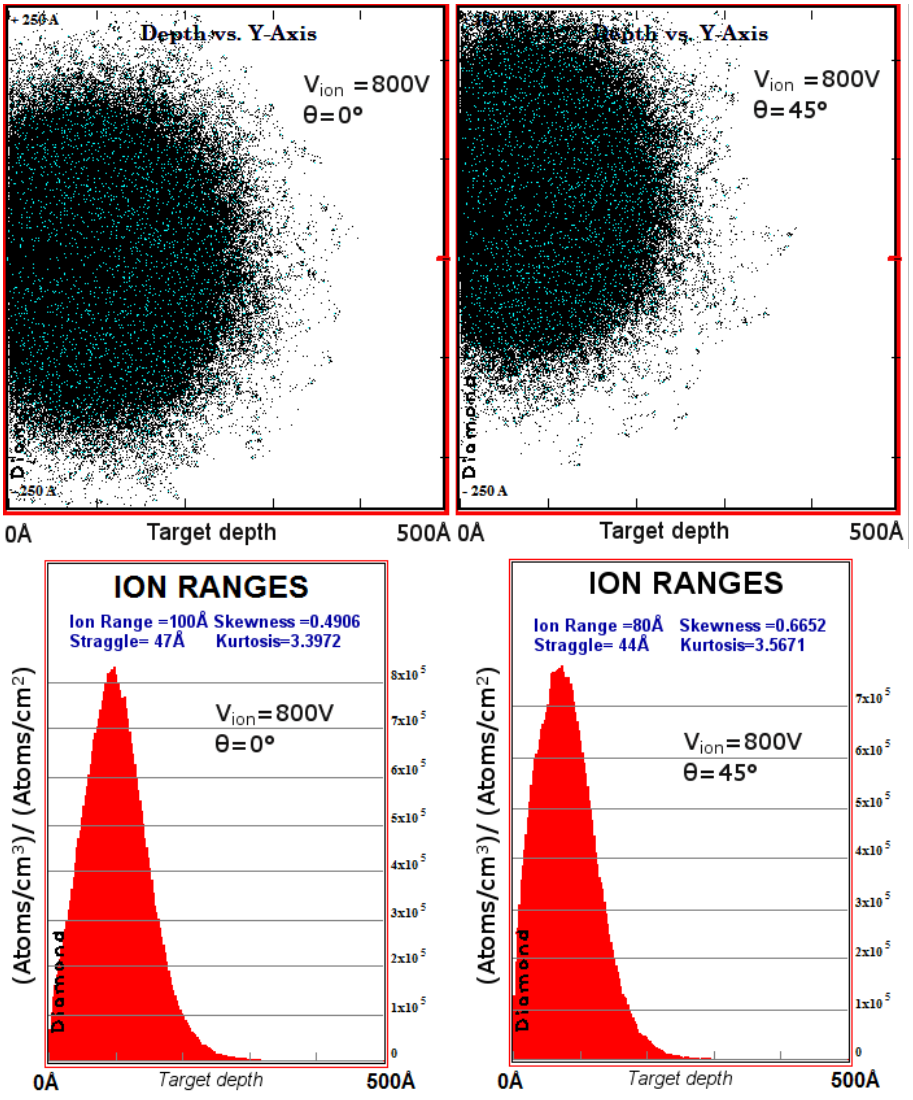

Figure 4.7: *Evaluation of penetration depth for hydrogen atoms on diamond sample during plasma exposure. The simulations take into account different direction of diffusion (0 and 45° respect to the surface normal) and for a plasma potential of 800V.*

subsurface layers of the sample (as proposed by Schenk, even in that case the subsurface layer was composed only by carbon atoms); the number of layers involved may be not limited to the first two in the subsurface region, as Montecarlo simulation showed. Then, a component for carbon atoms bonded with hydrogen at the surface (maybe forming monohydrides, as Graupner suggested) is expected: as, said, Schenk and coworkers proposed that surface component is shifted by 0.16 eV towards lower binding energy respect to bulk component but, with our setup, we are unable to resolve it;

- C_H is the sum of the contribute from the hydrogen atoms bonded with surface carbon atoms and the contribute of hydrogen atoms in the subsurface layers due to hydrogen plasma exposure; even in this case the numbers of layers of subsurface region involved is unknown.

It is clear that further investigation are needed in order to define better the nature of this component. A clarifying option in that sense may be the study of C_H evolution as a function of temperature: as suggested by Graupner and coworkers[37], the desorption temperature is different depending on the hydrogen-carbon bond type. Operatively, we decide to fix this component 0.5 eV towards higher binding energy respect to the bulk component of the fit, according to Graupner measurements, in order to maintain compatibility with precedent literature.
Similarly of what was seen for C1s core level deconvolution, the analysis and the deconvolution of O1s spectrum was performed starting from previous literature on the argument. Unfortunately, only few attempts to deconvolute Oxygen spectra was done[73, 80, 81] and generally the binding energies of the peaks obtained in these cases was compared with the literature for polimeric and organic systems. Because of these limits we have chosen to limit the deconvolution of the oxygen spectrum to four Voigt profiles, as can be seen in an example shown in Fig. 4.8. The four components are so assigned:

- O1 peak is mainly due to Oxygen bonded in C–OH and C–O configuration;

- O2 and O3 peaks are principally due to oxygen bonded in long chains (such as OH–C=O or O–C=O) where the photoemitted electron comes

from the single bonded oxygen (O2) and double bonded oxygen (O3), respectively;

- O4 peak is related to oxygen in H_2O.

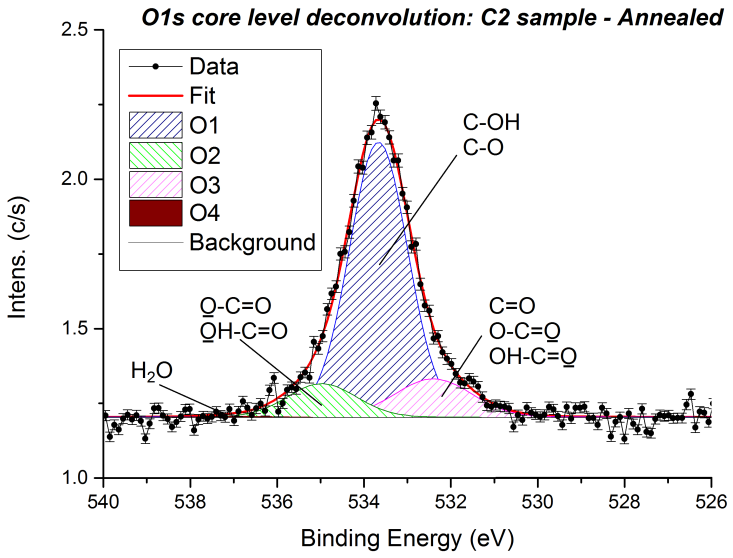

Figure 4.8: *Deconvolution of O1s core level spectra, for the non-conductive (annealed) sample. The details of the deconvolution and peak assignation can be found in text.*

Fit component	Posit.(eV)	Ampl.	GW	LW
O1	533.7	1.62	1.52	0.15
O2	535.0	0.23	1.81	0.15
O3	532.4	0.30	2.01	0.15
O4	536.8	0.01	1.81	0.15

Table 4.3: *Fit values of O1s core level spectra for the annealed sample. For every component the position in energy, the amplitude, the gaussian (GW) and the lorentzian (LW) parameter are shown. The lorentzian parameter was fixed at 0.15 eV according to ref.[37].*

4.1.2 Nature of oxygen in non-conductive sample

As we observed early in the last section, XPS spectrum for the non-conductive case reveals that, even after the annealing of the sample, oxygen is still present. To understand better the nature of this oxygen, and in particular if it is related to impurities inside the diamond or not, we perform XPS measurements as a function of the collecting angle, from normal to grazing collection, with the idea to enhance the signal coming from the surface[1] respect to the one coming from the bulk. For this purpose we perform this measure on the C1s signal that have clearly identifiable surface and bulk components: the results are shown in Fig. 4.9, in which the O-related an the H-related components normalized by the bulk component are presented as a function of the collecting angle. It is evident from

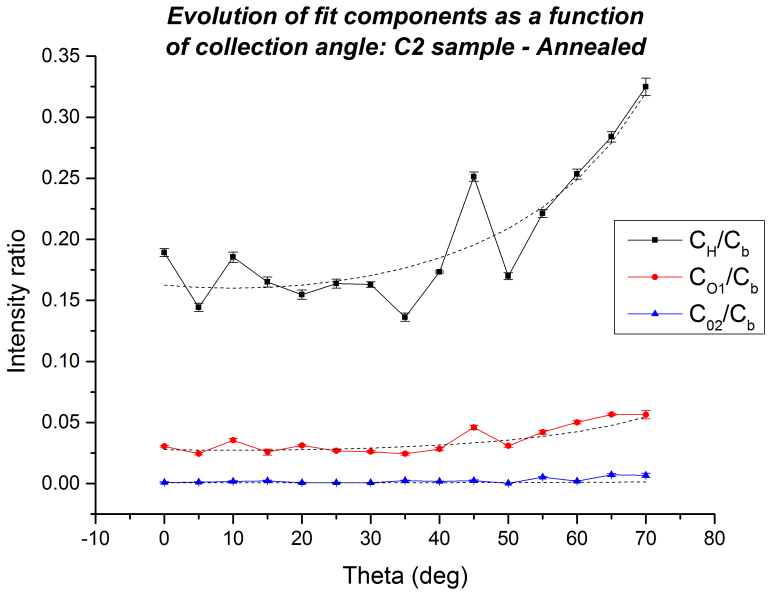

Figure 4.9: *Evolution of fit components ratio respect to the bulk component as a function of the collecting angle for the non-conductive sample. The dotted lines represent the theoretical $1/\sin^2\theta$ trend of the Fadley model[43], as shown in section 2.1.4.*

the figure that both the H-related and the O-related components ratio increases for grazing collection angle respect to the surface, confirming -for the H-related

[1] with *surface signal* we mean even the contribution from subsurface

component- and demonstrating -for the O-related components- the surface nature of the signal. Then, we have to exclude the possibility that this oxygen comes from impurities inside the diamond and, instead, consider the fact that this oxygen is chemisorbed in the surface of the sample: it probably comes from the acid treatment we performed on every sample prior to the hydrogen plasma treatment or, alternatively it can be related to a cleaning issue of hydrogen chamber; however, plasma treatment is not effective to remove it. Lastly, the particular evolution of the H-related component, that confirms its surface nature, may be compared with the Montecarlo simulation showed before: as said we are unable to estimate the correct value for the potential difference between the hydrogen plasma and the diamond surface. This observation, however, suggest the idea that this potential may be very low, even lower than the simulation shown before, and thus the diffusion of hydrogen inside diamond lattice is very limited.

4.1.3 The conductive sample

Once the detail about the non-conductive sample has been discussed we moved our attention on the conductive sample, i.e. the sample in which airborne molecules, that are responsible of conduction, are still adsorbed on. To obtain this condition we exposed the non-conductive sample to air for several days.
As in the case of non-conductive sample, we started with a survey: the features found (as shown in Fig. 4.10) are the same observed for the non-conductive case. The only core level visible are C1s and O1s core level: other elements contained in air (such as nitrogen) gave no detectable feature. We then compared the spectra obtained from conductive and non-conductive sample (depicted in the upper part of Fig. 4.11 for C1s core level and in the lower part for O1s core level): it is evident from the comparison of the core levels that the transition from conductive to non-conductive phase causes a shift in energy: the shift is rigid and its amount is of about 1.2 eV. For similar systems (as in the case of air exposed hydrogenated diamond [27] but also in the case of hydrogenated diamond covered by MoO_3 or by fullerene[41, 42]) the transition from covered to adsorbate-free diamond gives similar values in the shift, and it has been attributed to band bending effects.
More significantly, instead, is the evolution of oxygen peak during the transition to the non-conductive phase: it is worth noting, in fact, the variation

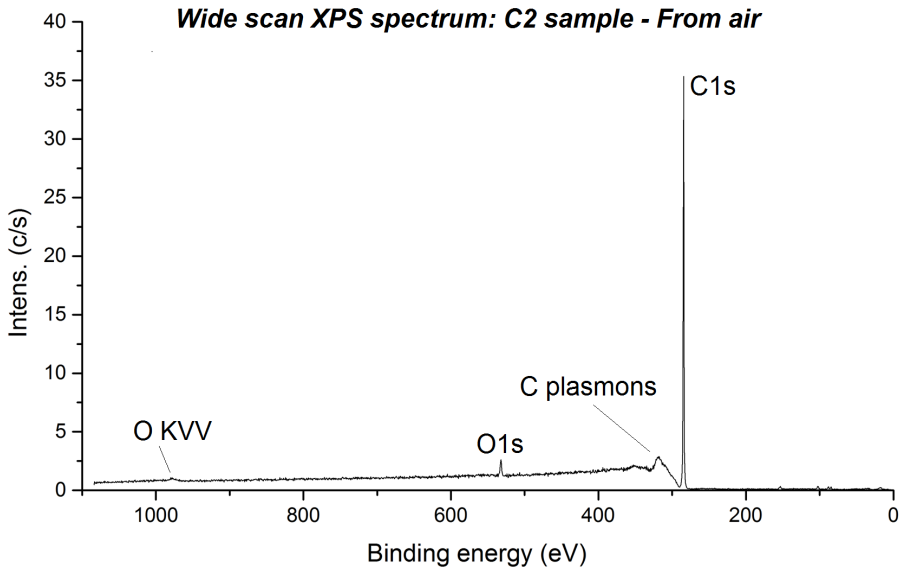

Figure 4.10: *XPS survey on a hydrogen-terminated diamond sample. It is possible to recognize photoemission peaks from C1s core level (at a binding energy of about 286 eV) and O1s core level (about 530eV). Spectrum have been taken with a* $Al_{k\alpha}$ *source (1486.7eV) and a pass Energy of 40 eV. The resolution is 450meV.*

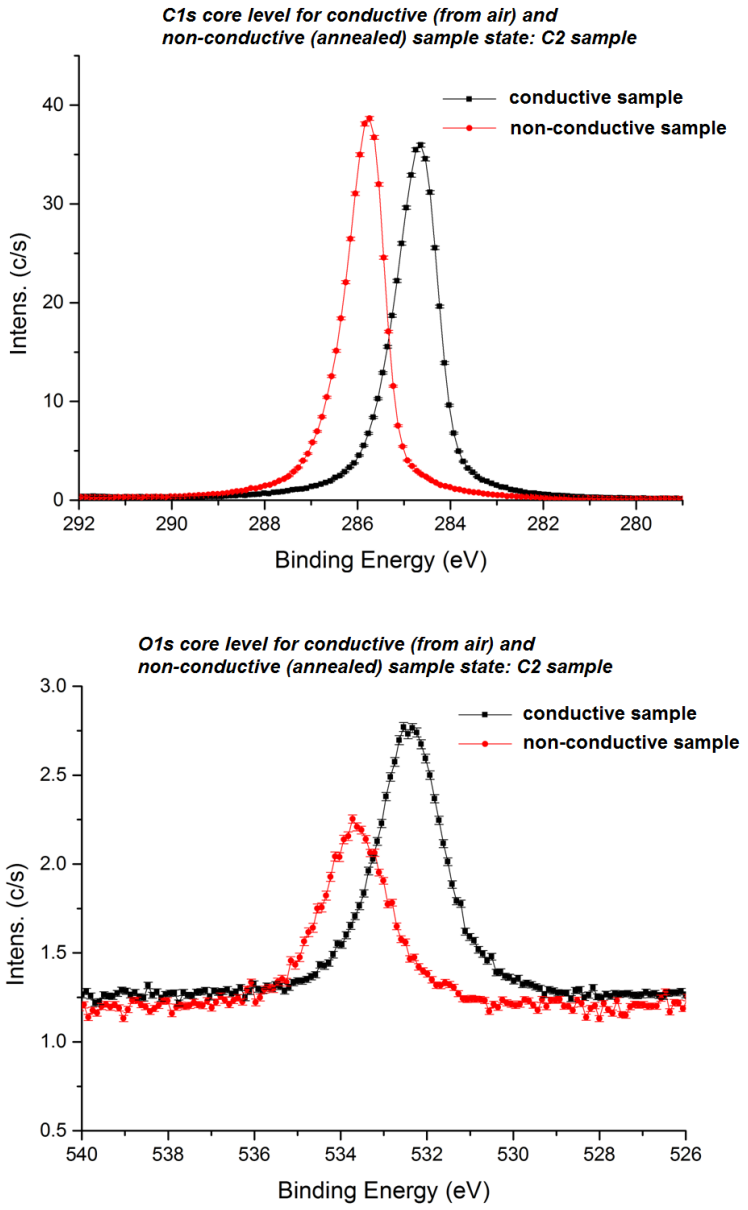

Figure 4.11: *Comparison between conductive (from air) and non-conductive (annealed) sample. Upper: C1s core level, lower: O1s core level. All the spectra have been taken with a $Al_{k\alpha}$ source (1486.7eV) and a pass Energy of 40 eV. The resolution is 450meV.*

in the amount of oxygen from conductive to non-conductive case. As said, all the oxygen present after the annealing of the sample covers 33±3% of the surface. Thus, the oxygen amount found in the conductive (from air) case is the sum of the contribution from oxygen adsorbed even after the annealing, that does not participate in the conduction mechanism, and from oxygen that is lost during the annealing treatment and is instead responsible of the surface conduction: we then refer to the two contributions as *non-active* and *active* oxygen, respectively.
In order to estimate the fraction of active oxygen we properly subtracted the non-active contribute from the oxygen peak in the conductive case (Fig. 4.12) and we found that 41±1% of total oxygen amount in the conductive case was responsible of surface conduction. Consequently we calculate the fraction of

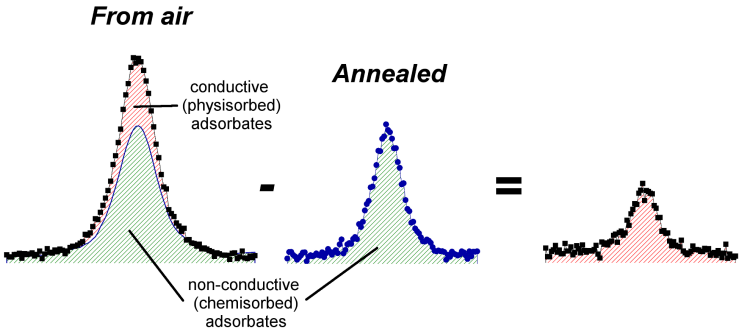

Figure 4.12: *To calculate the fraction of oxygen responsible of surface conduction in the conductive spectrum we subtract the contribute due to non-active oxygen (i.e. the area of oxygen in non-conductive spectrum). From calculation we found that 41±1% of the conductive spectrum is related to active oxygen, corresponding to a fraction coverage of the surface of 23±3%.*

the surface covered by active oxygen, and we found a coverage of 23±3%.
It is possible to correlate this value to previous hole sheet density measurements: in fact, with the strong hypothesis that every (physisorbed) oxygen atom bonded with the hydrogenated surface steals an electron from the diamond, and considering that only 23% of the surface can be considered active, we can estimate a surface density of the hole left in diamond of the order of 10^{14} cm^{-2}: this value is in good agreement with the ones reported in

literature[25, 82, 83].

The next step is then to individuate if there is a preferential way of bonding for the active oxygen. We start from the deconvolution of C1s and O1s level, presented in figg. 4.13 and 4.14: the deconvolution of C1s peak has taken into account a rigid shift in energy respect to the non-conductive case for all the components by an amount of 1.2 eV: the oxygen-related components appear to be increased respect to the non-conductive case. Also in the case of O1s we have taken into account the rigid shift for components in deconvolution and a general increase of components was seen, similar to the case of C1s.
Comparing the evolution of components in the O1s spectra of the conductive and the the non-conductive sample, we do not recognize a preferred way to bond for oxygen: the three principal components after annealing decrease roughly by the same amount; instead the peak related to H_2O almost disappear. The comparison is plotted in Fig. 4.15.

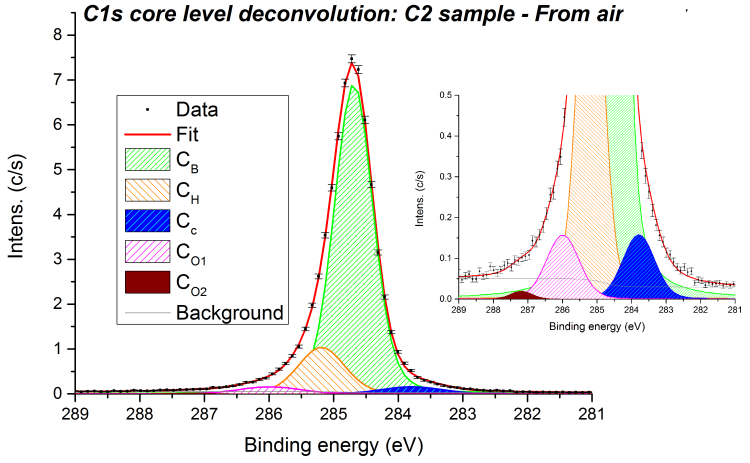

Figure 4.13: *Deconvolution of C1s core level spectra for the conductive (from air) sample. The components used are so assigned: C_b is relative to bulk component, C_c is due to surface carbon not bonded with hydrogen and defects, C_H has been assigned to carbon bonded with hydrogen both in the surface and in the subsurface region, C_{O1} and C_{O2} are due to oxygen-bonded carbon, where carbon has, respectively, single bond to oxygen or double bond to oxygen.*

Fit component	Posit.(eV)	Ampl.	GW	LW
C_b	284.7	5.65	0.62	0.15
C_H	285.2	1.00	0.76	0.15
C_c	283.8	0.19	1.01	0.15
C_{O1}	286.0	0.20	1.04	0.15
C_{O2}	287.2	0.02	0.66	0.15

Table 4.4: *Fit values of C1s core level spectra for the annealed (from air) sample. For every component the position in energy, the amplitude, the gaussian (GW) and the lorentzian (LW) parameter are shown. The lorentzian parameter was fixed at 0.15 eV according to ref.[37].*

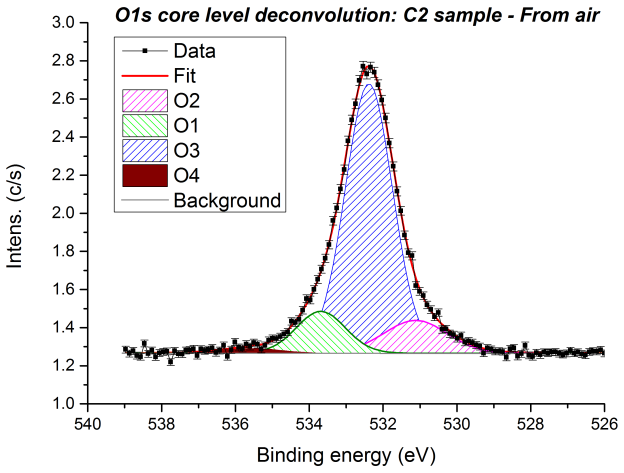

Figure 4.14: *Deconvolution of O1s core level spectra, for the conductive (from air) sample. The components used are so assigned: O1 is relative to Oxygen bonded with carbon as C-OH o as C-O; O2 and O3 are relative to oxygen from OH-C=O or O-C=O chains, with photoemission from single(double) bonded oxygen in the case of O2(O3) component; O4 is relative to oxygen in H_2O.*

Fit component	Posit.(eV)	Ampl.	GW	LW
O1	532.4	2.39	1.44	0.15
O2	531.1	0.38	1.95	0.15
O3	533.7	0.39	1.95	0.15
O4	533.5	0.05	1.81	0.15

Table 4.5: *Fit values of O1s core level spectra for the annealed sample. For every component the position in energy, the amplitude, the gaussian (GW) and the lorentzian (LW) parameter are shown. The lorenztian parameter was fixed at 0.15 eV according to ref.[37].*

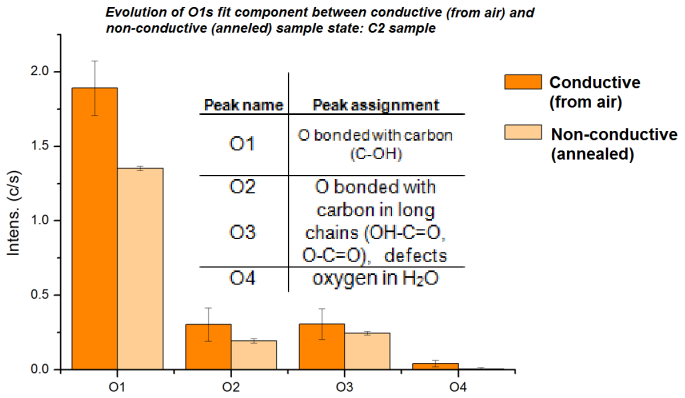

Figure 4.15: *Comparison of fit components used for O1s core level for conductive (i.e from air) and non-conductive (annealed) sample.*

4.1.4 Oxygen exposure

Finally, in this section we are going to show the data obtained during controlled oxygen exposure (with the setup described in previous chapter) of diamond surface.

Initially we started performing controlled exposure in step of 3000L (1L corresponds to an exposure of 10^{-6} Torr for one second) on an adsorbate-free (non-conductive) sample. The effect of the exposure are monitored by O1s core level evolution (as shown in Fig. 4.16): we can distinguish two effects: from the point of view of the energy position there is a significant shift towards lower binding energies after the first exposure of 3000L, with slight shifts after 6000L and 9000L exposures: after 9000L the shift of the O1s core level saturates to a value of 0.55eV respect to the non-conductive spectra. The second aspect is the amount of oxygen that increases during the exposures, saturating again at 9000L.
For both the two aspects oxygen exposure does not replicate the air-exposure behaviour; however, the energy shift of the oxygen peak could be explained in terms of band bending, as in the case of air exposed sample.
Then, we also performed annealing on oxygen-exposed sample with the same parameters used to remove airborne species from the sample. In this case we found the non-reversibility of oxygen-exposure: in fact, as depicted in Fig.4.17, in which the O1s peaks for non-conductive sample and for annealed sample

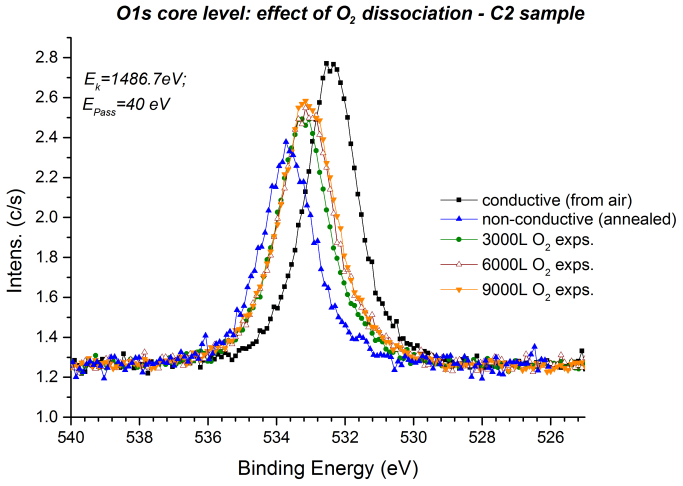

Figure 4.16: *Controlled oxygen exposure in step of 3000L (1L = 10^{-6} Torr/s). The exposure is monitored with O1s core level evolution, starting from non-conductive (annealed) sample (in blue). For comparison data for conductive (from air) phase (black) are shown. The compared spectra have been taken with a $Al_{k\alpha}$ source (1486.7eV) and a pass Energy of 40 eV. The resolution is 450meV.*

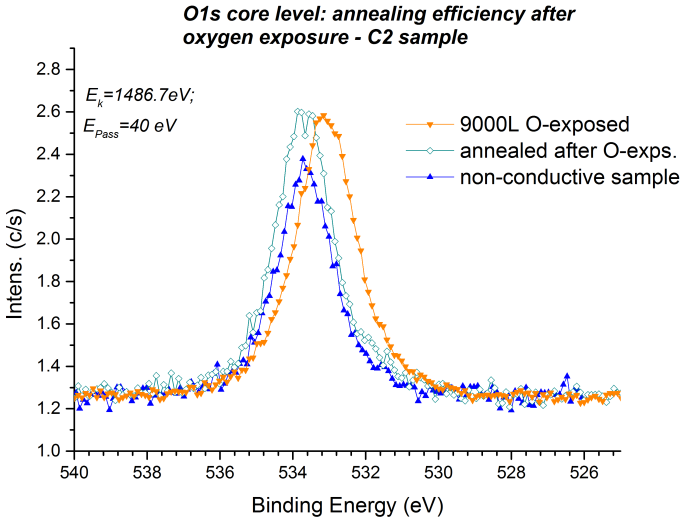

Figure 4.17: *Comparison of O1s core level spectra for O-treated sample before and after the annealing respect to the non-conductive sample. The compared spectra have been taken with a $Al_{k\alpha}$ source (1486.7eV) and a pass Energy of 40 eV. The resolution is 450meV.*

after the O-treatment, the quantity of oxygen after the annealing does not return to its initial value (remaining unchanged after the annealing) while the energy position of the annealed sample returns to the values found for the non-conductive sample.

In order to understand better the nature of the reaction behind this non-reversibility of the oxygen treatment and to overcome the difficulties in the deconvolution of O1s we compare the evolution of the sum of oxygen-related peaks in C1s and the area of O1s peak, for all the four cases studied (conductive, non-conductive, oxygen-exposed and annealed after oxygen exposure). The comparison is shown in Fig. 4.18: we normalized the two sets by the annealed sample value because it represents the reference value due to the absence in principle of physisorbed molecules on surface.

From the figure is evident that the evolution for the two curves is slightly different; starting from the components obtained from O1s deconvolution essentially we summarize what seen for O1s peak: it can be noticed that oxygen quantity significantly decreases passing from the conductive to the non-conductive phase; the oxygen quantity is partially restored by O-exposure and does not change after annealing the sample. Instead, focusing on the curve obtained from C1s, we see a decrease in the oxygen quantity passing from conductive to non-conductive phase but we do not see the partial restoring in the Oxygen-exposed phase. The restoring, in fact, occurs only after the annealing treatment.

We interpreted this particular behaviour in terms of different nature of the O-bonded species for the conductive and O-exposed case: the curves, in fact, suggest the possibility that, while in the airborne species oxygen atoms are principally bonded with carbon, this is not more true for oxygen (cracked by filament) which only with the thermal energy provided by annealing finally bonds with carbon, probably chemisorbing on diamond surface. This turns the question on what oxygen atoms are bonded with in the case of oxygen exposure. A possible interpretation of this behaviour can be found in literature, for similar system: recently [84] it has been discovered that UV oxidation (a technique in which sample is irradiated by UV source in pure O_2 atmosphere) leaves the surface of H-terminated diamond with a high density of OH^- fragments which bond electrostatically with the CH present at the surface. Similarly we can believe that O atoms produced by the O_2 thermal

cracking adsorb on the sample as a part of OH ions (hydrogen can be easily found on the surface of the sample). Then, the thermal activation produced by the annealing could transform the electrostatic bond between OH^- ion and surface CH into different covalent bonds principally encompassing hydroxyl, carbonyl and carboxyl bonds and ether-like bonds that are the typical final product of stronger treatments, such as Oxygen-plasma treatments [84].

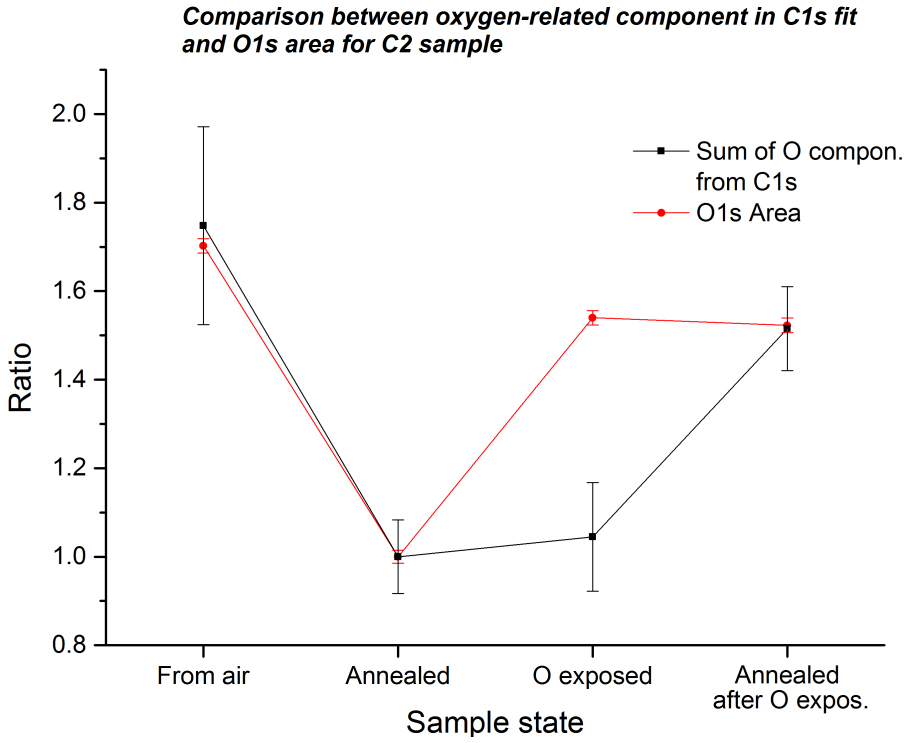

Figure 4.18: *Comparison of O1s core level spectra for O-treated sample before and after the annealing respect to the non-conductive sample.*

4.2 Investigation of C-H stretching mode

In this section we are going to discuss our investigation performed on C-H stretching mode, ν(C–H), done with the energy loss technique, focusing our attention on the evolution of the stretching mode intensity in different conductive states.
In figure 4.19 we compare the vibrational energy loss region for the conductive (air exposed) sample and the non-conductive sample. As in the case of XPS spectra, in order to have a non-conductive behaviour, we annealed the sample at 450°C for one hour.
From the spectra we can only recognize a small peak located at 360 meV, that

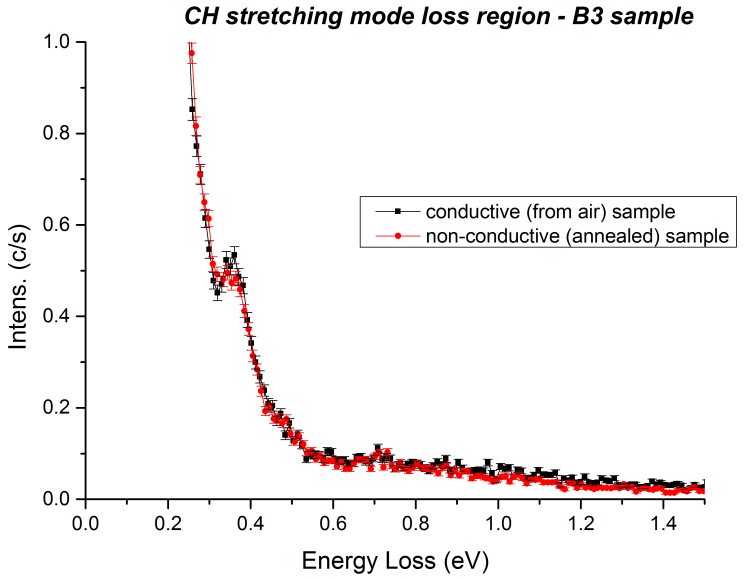

Figure 4.19: *Comparison CH stretching mode loss for conductive (from air) and non-conductive (annealed) sample .*

is just the loss related to ν(C–H); a repetition at 720 meV is poorly visible. As can be seen from the figure with our setup we are unable to distinguish any other vibrational mode.
To determine the exact energy position and intensity of CH stretching we performed a deconvolution in that loss region: in the deconvolution we considered also the presence of other vibrational modes, even not recognizable in the

spectra. An example of the deconvolution done is presented in Fig. 4.20: the example presented is relative to the conductive case; for the energy position of non-resolved vibrational modes, presented in the table below the figure, we referred to [26].

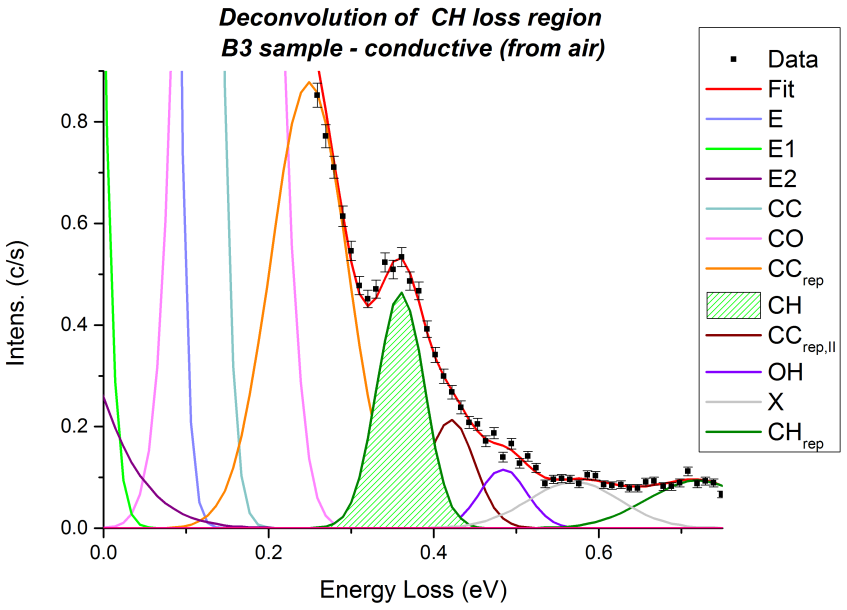

Fit component	Posit.(eV)	Assignation
E, E1, E2		Deconvolution of elastic peak
CC	0.151	combination of ν(C–C) and δ(C–H)
CO	0.243	ν(C–O)
CC_{rep}	0.302	ν(C–C) overtone
CH	**0.361**	**ν(C–H)**
$CC_{rep,II}$	0.2	second ν(C–C) overtone
OH	0.421	ν(O–H)
X	0.507	combination of ν(C–C) overtone and ν(H–H)
CH_{rep}	0.722	ν(C–H) overtone

Figure 4.20: *Deconvolution of energy loss spectra in the CH region, and assignation of the component used. For assignation we refer to [26].*

As can be seen from table 4.6, by the comparison of ν(C–H) amplitude for the two conductive states, we observed a slight decrease in the intensity of the signal after the annealing of the sample, that may be related to the desorption of hydrocarbons molecules from surface.

Conduction state of sample	CH stretching ampl.	Normalized CH stretching ampl. ($\times 10^{-10}$)
Conductive (from air)	0.034±0.002	4.4±0.3
Non-conductive (annealed)	0.029 ± 0.002	3.7±0.3

Table 4.6: *Comparison of CH stretching mode amplitudes for conductive (from air) and non-conductive (annealed) sample, as determined by a deconvolution of the CH stretching loss region. In the table the amplitudes normalized by elastic peak are also reported.*

Conclusions

The investigation performed on hydrogen-terminated diamond, described in previous chapters, has shown the limits of typical sample preparation for our purposes. Major issues have been found in terms of homogeneity of hydrogenation: an electron reflectivity pattern, taken for the sample studied, has shown the presence of two zones of reflectivity on the sample, with the number of electron reflected that was roughly the double in one zone of the sample with respect to the other; the zone characterized by higher reflectivity was also characterized by higher resistance: we ascribed these inhomogeneity effects to the relative position between the sample and the hydrogen plasma used to terminate the surface. The placement of the samples in the hydrogenation chamber, done manually, has its cost in terms of reproducibility of the sample produced and should be improved. However, we have showed how mapping the sample with resistance and/or spectroscopic measurements can be a significant but simple tool that has to be introduced in the preparation protocol, in order to evaluate sample homogeneity.

A second issue, related to sample preparation, has been found on non-conductive (adsorbate-free) sample: we observed that a significative portion of the sample, that we estimated to be 33±3 % is covered by chemisorbed oxygen. Possible sources of oxygen contaminants could be the acid treatments we performed prior to hydrogenation or a cleaning issue of the hydrogenation chamber. Actually, the acid treatments were performed on the samples with the idea that these, due to their commercial nature, might present residues of processing or unknown surface impurities and, therefore, terminating uniformly in oxygen, the problem was obviated. A possible solution in this case is to repeat the hydrogen treatment several times or, more drastically, to eliminate this passage and perform hydrogenation without any preliminary treatment. In the case of cleaning issue, instead, a more restrictive control of hydrogenation parameter

is clearly needed.
Despite these issues in sample preparation, we were able to perform a conductive test, measuring the resistance as a function of temperature and pressure: the measurements showed as the resistance for non-conductive state is eight order of magnitude higher than the resistance of conductive state, as the measurements of electronic grade sample showed (the obtained resistance values are, respectively, 10^{12} and 10^{6} Ω), consistently with similar works found in literature[8]: it may be interesting to study, once the homogeneity and impurity issues are resolved, if there is an improvement even in the conductive properties.

Interesting observation has been found studying the depth of the surface hydrogen layer: Montecarlo simulation, in fact, suggested the possibility that hydrogen may be present not only at the surface but even deeper, extending for several layers in the subsurface region. This observation helped us in the interpretation of C_H component used in C1s core level deconvolution: despite early interpretation[37] attributed to this component a pure surface behaviour, we believe that C_H may be reasonably related to hydrogen bonded with carbon (even forming hydrocarbon structures) in the subsurface zone and deeper. For what concern the surface, recent hypothesis[40], place a surface hydrogen related component at 0.16 eV towards lower binding energies respect to the bulk component: at this stage we are unable to resolve it and more investigation (especially as a function of temperature) are needed in that sense.
Regarding the elemental analysis and the nature of physisorbed species responsible of surface conductivity, spectra taken in the conductive case (i.e. in presence of airborne species adsorbed on hydrogen-terminated diamond surface) showed the increasing presence of carbon-oxygen related species (such as C–OH, C–O, C=O) respect to the non-conductive case: we estimated that a fraction of 23±3% of the conductive sample was covered by physisorbed oxygen-related species. This value can be related to a hole sheet density in agreement with the ones reported in literature[25, 82, 83]. For what concern the nature of oxygen-related species it seemed that there was not a preferred absorbed species compared to the others: a more detailed analysis, however, can be done with better prepared samples that do not present the oxygen impurities issue.

The comparison between the spectra for conductive sample showed also a rigid shift of 1.2 eV respect to the energy positions for non conductive sample: this shift it has been attributed to a band bending established with the adsorption of airborne species and represented a terms of comparison for controlled oxygen exposures. Spectra taken after oxygen exposure have shown a less pronounced energy shift (0.5 eV respect to non-conductive sample) suggesting that oxygen presence is a necessary but non-sufficient condition to replicate the conductivity of airborne species. Different is also the absorption mechanism, studied by the evolution of oxygen and C-O related species quantities upon different exposure and annealing treatment, that indicated the possible presence of oxygen non-bonded with carbon after oxygen exposures, that chemisorbed on the surface after an annealing treatment: it may be interesting studying if temperature is effective to induce different way of absorption.

Concluding, the scenario presented shows how the study of microscopic properties of hydrogen-terminated diamond requires a preparation of samples with more stronger constraints, in terms of homogeneity and presence of impurities, compared to the study of macroscopic properties. This is the starting point to get more and more completed information from elemental analysis of the surface; it can be interesting, however, study if the improvement in sample preparation to study microscopic properties may be a way to obtain more performing samples also from the electric point of view: in principle, in fact, avoid contaminants permits to have a larger active area though maintaining the same sample size. Moreover, a more detailed elemental analysis of the conductive samples can be helpful in the selection of the active species that have to be adsorbed on hydrogen-terminated diamond. In this sense the study of alternative methods to hydrogenate the diamond surface is needed: this can be done varying the parameters for the the plasma treatment (we have shown, for example, how temperature can improve the sample quality) or, even, using alternative approaches, such as hot filament hydrogenation[85]. Once the issues behind the sample preparation will be resolved it can be interesting, as a further topic, the comparison of macroscopic and microscopic effects on hydrogen-terminated diamond, exposing the samples to different active gases such as NO_2 and SO_2, that are known to be effective to increase the hole sheet density of hydrogen-terminated diamond as suggested by previous

measurements[25], and can help to highlight more clearly the relation between oxygen and the surface conduction of diamond.

Appendix A An alternative C1s deconvolution

In section 4.1.1 we discussed the model for C1s deconvolution: in the deconvolution presented we used a component, C_H, for which we estimated the coverage. As discussed previously, the coverages estimated for that component are higher than we expected.
We repeated the same test using in this case two peaks instead of only one, with the idea that overestimation in first case was due to a component related to oxygen-bonded carbon: in some works, in fact, the presence of a component shifted in a range between 0.6 and 1 eV respect to sp^3 carbon was correlated to carbon bonded with oxygen in a C-OH configuration [76–78]. The method used is the following:

1. A component of the fit, C_H, has been moved in the higher binding energy zone respect to the bulk component with a shift in the range between 0.36 eV and 0.65 eV from the bulk component (that is the region in which the chi-squared values in the first test were the lowest) with a step of 0.05 eV;

2. A second component of the fit, C_{OH}, has been moved in the higher binding energy zone respect to the bulk component with a shift in the range between 0.2 eV from C_H component (that is a limit related to resolution of our setup) and 1.05 eV from bulk component (higher values did not show a chi-squared value low enough) with a step of 0.05 eV.

3. for each step we calculate:

    - the coverage related to C_H component. For the estimation we used the Fadley model proposed in section 2.1.4, in which we use the C_H

component in the C1s spectra as overlayer signal and the C_b component as substrate signal; we refer to this as H-related coverage;

- the oxygen coverage. For the estimation we used the Fadley model proposed in chapter 3, in which we use the sum of oxygen-related component (included C_{OH}) in the C1s spectra as overlayer signal and the C_b component as substrate signal; we refer to this as O-related coverage;

4. the results have been compared on the basis of chi-squared test value, the oxygen estimated coverage (remembering that from the comparison of O1s and C1s peaks we found a fraction of diamond surface covered by oxygen of 33±3%) and the coverage estimated by the C_H component: depending on the model, we expect different values of coverage; for the model proposed by Grupner and coworkers[37], we in fact expect a coverage that has to be around 70%, considering that hydrogen is located only in the surface region and that a portion of the sample is covered by oxygen; differently for the model proposed by Schenk and coworkers[40] we expect a coverage around 100% because of the subsurface nature of the assignment.

The results for this second test are presented in table A.1.

As can be seen from the table, even with the introduction of a second component, the estimated hydrogen and oxygen coverages are both not compatible with the expected values: taking into account for example the case in which the C_H component is fixed at shift 0.36 eV, the shift proposed by Schenk and coworkers in their model, the estimated coverages for hydrogen and oxygen are both largely higher than the expected value, and this is true for each value of C_{OH} shift. Similar conclusion can be given for C_H shift fixed at 0.5 eV, the shift proposed by Graupner and coworkers, and, moreover, for all intermediate values.

C_H shift (eV)	C_{OH} shift (eV)	χ^2	Hydrogen coverage (%)	Oxygen coverage (%)	Oxygen coverage estim. from O1s (%)
0.360	0.550	1.133	147±67	164±37	33±3
	0.600	1.133	163±58	141±29	
	0.650	1.133	196±53	119±24	
	0.700	1.134	227±46	100±20	
	0.750	1.135	253±38	86±15	
	0.800	1.135	275±33	75±12	
	0.850	1.136	294±32	66±10	
	0.900	1.136	310±33	59±10	
	0.950	1.135	324±35	54±9	
	1.000	1.133	336±36	48±8	
	1.050	1.130	346±36	44±7	
0.400	0.600	1.115	83±25	150±17	
	0.650	1.116	109±26	128±15	
	0.700	1.118	142±26	108±13	
	0.750	1.120	176±26	92±11	
	0.800	1.123	204±25	79±10	
	0.850	1.125	226±25	69±9	
	0.900	1.126	245±26	61±8	
	0.950	1.126	261±28	55±7	
	1.000	1.126	275±29	49±7	
	1.050	1.124	285±30	45±6	
0.450	0.650	1.099	79±20	120±14	
	0.700	1.098	93±19	104±12	
	0.750	1.099	110±18	90±10	
	0.800	1.101	131±17	79±9	
	0.850	1.104	153±17	69±8	
	0.900	1.107	174±19	61±7	
	0.950	1.109	192±20	55±7	
	1.000	1.110	207±22	49±6	
	1.050	1.111	219±22	44±6	

C_H shift (eV)	C_{OH} shift (eV)	χ^2	Hydrogen coverage (%)	Oxygen coverage (%)	Oxygen coverage estim. from O1s (%)
0.500	0.700	1.102	75±10	96±11	33±3
	0.750	1.101	84±15	84±9	
	0.800	1.100	93±14	78±8	
	0.850	1.098	150±13	66±7	
	0.900	1.096	120±13	59±7	
	0.950	1.096	136±15	53±6	
	1.000	1.098	151±13	47±6	
	1.050	1.100	164±17	42±5	
0.550	0.750	1.138	68±13	75±9	
	0.800	1.138	76±12	69±8	
	0.850	1.136	81±11	62±7	
	0.900	1.129	87±10	55±6	
	0.950	1.119	97±14	50±6	
	1.000	1.111	110±12	45±5	
	1.050	1.108	121±13	41±5	
0.600	0.800	1.218	68±12	63±13	
	0.850	1.220	71±10	70±9	
	0.900	1.220	74±10	51±8	
	0.950	1.211	75±9	46±8	
	1.000	1.187	82±11	42±5	
	1.050	1.167	91±10	38±4	
0.650	1.000	1.356	72±9	37±6	
	1.050	1.313	71±8	35±4	

***Table A.1**: In table is represented the energy shift value between the bulk component in the fit, C_b, and the C_H component and between C_b and the C_{OH} component; for every value a chi-squared value, coverage of C_H component and oxygen coverage by O-related (included C_{OH}) components in C1s have been calculated. For comparison, we also estimated oxygen using O1s signal.*

The best compromise between calculated coverages and expected values seems to be obtained with the two components respectively at 0.6 eV and 0.95 eV from the bulk peak, where we found a hydrogen coverages of 75±9% and oxygen coverage of 46±8% (slightly out the compatibility range for the coverage estimated from O1s): even in this case, however, the chi-squared value obtained is greater than the values found using only C_H, giving poor support to the introduction of a second component.

Bibliography

[1] G. Davies, Basic properties of diamond: Phonon spectra, thermal properties, band structure, in: CVD Diamond for Electronic Devices and Sensors, Wiley, 2009.

[2] J. A. Carlisle, Diamond films: Precious biosensors, Nat. Mater. 3 (2004) 668–669.

[3] D. M. Trucchi, P. Allegrini, P. Calvani, A. Galbiati, K. Oliver, G. Conte, Very Fast and Primingless Single-Crystal-Diamond X-Ray Dosimeters, IEEE Electron Device Lett. 33 (2012) 615 – 617.

[4] H. Kawarada, M. Aoki, M. Ito, Enhancement mode metal-semiconductor field effect transistors using homoepitaxial diamonds., Appl. Phys. Lett. 65 (1994) 1563–1565.

[5] M. Kasu, K. Hirama, K. Harada, T. Oishi, Study on capacitance-voltage characteristic of diamond field-effect transistors with NO_2 hole doping and Al_2O_3 gate insulator layer, Jpn. J. Appl. Phys. 55 (2016) 041301.

[6] J. Ristein, W. Zhang, L. Ley, Hydrogen-terminated diamond electrodes. I. Charges, potentials, and energies, Phys. Rev. E 78 (2008) 041602.

[7] D. Moran, D. MacLaren, S. Porro, H. McLelland, P. John, J. Wilson, Processing of 50 nm gate-length hydrogen terminated diamond fets for high frequency and high power applications, Microelectron. Eng. 88.

[8] F. Maier, M. Riedel, B. Mantel, J. Ristein, L. Ley, Origin of surface conductivity in diamond, Phys. Rev. Lett. 85 (2000) 3472–3475.

[9] C. J. Wort, R. S. Balmer, Diamond as an electronic material, MaterialsToday 11 (2008) 22–28.

[10] H. Holloway, K. C. Hass, M. A. Tamor, T. R. Anthony, W. F. Banholzer, Isotopic dependence of the lattice constant of diamond, Phys. Rev. B 44 (1991) 7123–7126.

[11] L. R. Saravia, D. Burst, Band structure and interband optical absorption in diamond, Phys. Rev. 170 (1968) 683–686.

[12] A. Krueger, New carbon materials: Biological applications of functionalized nanodiamond materials, Chem. Eur. J. 14.

[13] C.-M. J. Sung, Optimised cell design for high-pressure synthesis of diamond, High Temp. High Press. 33 (2001) 489–501.

[14] J. E. Butler, H. Windischmann, Surface transfer doping of semiconductors, MRS Bulletin 23 (1998) 22–27.

[15] K. Landtrass, K. Ravi, Resistivity of chemical vapor deposited diamond film, Appl. Phys. Lett. 55 (1989) 975–977.

[16] K. Landtrass, K. Ravi, Hydrogen passivation of electrically active defects in diamond, Appl. Phys. Lett. 55 (1989) 1391–1393.

[17] S. Grot, G. S. Gildenblat, C. W. Hatfield, C. Wronski, A. R. Badzian, T. Badzian, R. Messier, The effect of surface treatment on electrical properties of metal contacts to boron doped homoepitaxial diamond films, IEEE Electron Device Letters 11 (1990) 100–102.

[18] G. S. Gildenblat, S. A. Grot, A. Badzian, The electrical properties and device applications of homoepitaxial and polycrystalline diamond films, Proceedings of the IEEE 79 (1991) 647–668.

[19] K. Hayashi, Y. Sadanori, H. Watanabe, T. Sekiguchi, H. Ojushi, K. Kajimura, Investigation of the effect of hydrogen on electrical and optical properties in chemical vapor deposited on homoepitaxial diamond films, J. Appl. Phys. 81 (1997) 744–753.

[20] J. Shirafuji, T. Sugino, Electrical properties of diamond surfaces, Dia. Relat. Mater. 5 (1996) 706–713.

[21] S. G. Ri, T. Mizumasa, et al., Formation mechanism of p-type surface conductive layer on deposited diamond films, Jpn. J. Appl. Phys. 34 (1995) 5550–5555.

[22] S. G. Ri, K. Tashiro, S. Tanaka, T. Fujisawa, H. Kimura, T. Kurosu, M. Iida, Hall effect measurements of surface conductive layer on undoped diamond films in NO_2 and NH_3 atmospheres, Jpn. J. Appl. Phys. Part 1 38 (1999) 3492–3496.

[23] M. Riedel, J. Ristein, L. Ley, The impact of ozone on the surface conductivity of single crystal diamond, Dia. Relat Mater. 13 (2004) 746–740.

[24] M. Kubovic, M. Kasu, Enhancement and stabilizatioin of hole concentration of hydrogen-terminated siamond using ozone adsorbates, Jpn. J. Appl. Phys. 49 (2010) 110208.

[25] H. Sato, M. Kasu, Electronic properties of H-terminated diamond during NO_2 and O_3 adsorption and desorption, Dia. Relat. Mater. 24 (2012) 99–103.

[26] P. E. Pehrsson, T. W. Mercer, Oxidation of the hydrogenated diamond (100) surface, Surf. Sci. 460 (2000) 49–66.

[27] S. Iacobucci, P. Alippi, P. Calvani, M. Girolami, F. Offi, L. Petaccia, D. M. Trucchi, Electronic structure of hydrogenated diamond: Microscopical insight into surface conductivity, Phys. Rev. B 94 (2016) 045307.

[28] L. Diederich, O. M. Küttel, E. a. S. L. Schaller, Photoemission from the negative electron affinity (100) natural hydrogen terminated diamond surface, Surf. Sci. 349 (1996) 176–184.

[29] Y. Wang, H. Chen, R. Hoffman, Structural analysis of hydrogenated diamond-like carbon films from electron energy loss spectroscopy, J. Mater. Res. 5 (1990) 2378–2386.

[30] E. A. Maydell, E. Dunlop, D. J. Fabian, J. Haupt, W. Gissler, Electron energy loss study of diamond-like and amorphous carbon films, Dia. Relat. Mater. 2 (1993) 873–878.

[31] B. D. Thoms, J. E. Butler, HREELS scattering mechanism from diamond surfaces, Phys. Rev. B 50 (1994) 17450–17455.

[32] H. Ibach, D. L. Mills, Electron energy loss spectroscopy and surface vibrations, Academic Press, 1982.

[33] B. B. Pate, M. Oshima, J. A. Silberman, G. Rossi, I. Lindau, W. E. Spicer, Carbon 1s studies of diamond(111): Surface shifts, hydrogenation, and electron escape lengths, J. Vac. Sci. Technol. A 2 (1984) 957–960.

[34] J. F. Morar, F. J. Himpsel, G. Hollinger, J. L. Jordan, G. Hughes, F. R. McFeely, C1s excitation studies of diamond (111). I. surface core levels, Phys. Rev. B 33 (1986) 1340–1345.

[35] R. Klauser, J.-M. Chen, T. Chuang, L. M. Chen, et al., The interaction of oxygen and hydrogen on a diamond C(111) surface: a synchrotron radiation photoemission, LEED and AES study, Surf. Sci. 356 (1996) L410 – L416.

[36] J. Wu, R. Cao, X. Yang, P. Pianetta, I. Lindau, Photoemission study of diamond (100) surface, J. Vac. Sci. Technol. A 11 (1993) 1048–1051.

[37] R. Graupner, F. Maier, J. Ristein, L. Ley, High-resolution surface-sensitive C1s core-level spectra of clean and hydrogen-terminated diamond (100) and (111) surfaces, Phys. Rev. B. 57 (1998) 12397 – 12409.

[38] K. Bobrov, G. Comtet, G. Dujardin, L. Hellner, P. Bergonzo, C. Mer, Surface electronic states of the partially hydrogenated diamond $C(100) - (2 \times 1) : H$ surface, Phys. Rev. B 63 (2001) 165421.

[39] M. T. Edmonds, M. Wanke, A. Tadich, H. M. Vulling, K. J. Rietwyk, P. L. Sharp, C. B. Stark, Y. Smets, A. Schenk, Q.-H. Wu, L. Ley, C. I. Pakes, Surface transfer doping of hydrogen-terminated diamond by $C_{60}F_{48}$: Energy level scheme and doping efficiency, Jour. Chem. Phys. 136 (12) (2012) 124701.

[40] A. K. Schenk, K. J. Rietwyk, A. Tadich, A. Stacey, L. Ley, C. I. Pakes, High resolution core level spectroscopy of hydrogen-terminated (100) diamond, J. Phys. Condens. Matter 28 (2016) 305001.

[41] W. Chen, D. Qi, X. Gao, A. T. S. Wee, Surface transfer doping of semiconductors, Prog. Surf. Sci. 84 (2009) 279–321.

[42] S. A. O. Russell, L. Cao, D. Qi, A. Tallaire, K. G. Crawford, A. T. S. Wee, D. A. J. Moran, Surface transfer doping of diamond by MoO_3: A combined spectroscopic and hall measurement study, Appl. Phys. Lett. 103 (2013) 202112.

[43] C. Fadley, Basic concepts of x-ray photoemission spectroscopy, in: C. Brundle, A. Baker (Eds.), Electron spectroscopy: theory, techniques and application, Vol. II, Pergamon Press, 1978.

[44] B. H. Bransden, C. J. Joachain, Physics of atoms and molecules, Second Edition, Prentice Hall, 1983.

[45] H. Lüth, Solid surfaces, Interfaces and thin films, Fifth Edition, Springer, 2010.

[46] N. W. Ashcroft, D. N. Mermin, Solid state physics, Saunders College, 1976.

[47] S. Hüfner, Photoelectron spectroscopy, Second Edition, Springer, 1996.

[48] K. Siegbahn, ESCA applied to free molecules, North Holland, 1969.

[49] J. Contour, A. Salesse, M. Froment, M. garreau, J. Thevenin, D. Warin, Scattering mechanism of electrons interacting with surfaces in specular reflection geometry: Graphite, J. Microsc. Spectrosc. Electron. 4 (1979) 483–491.

[50] M. Shek, J. Hrbek, T. Sham, G. Xu, A soft x-ray study of the interaction of Oxygen with Li, Surf. Sci. 234 (1990) 324–334.

[51] E. Evans, D. L. Mills, Interaction of slow electrons with the surface of a model dielectric: theory of surface polarons, Phys. Rev. B 8 (1973) 4004–4018.

[52] D. L. Mills, The scattering of low energy electrons by electric field fluctuations near crystal surfaces, Surf. Sci. 48 (1975) 59–79.

[53] D. K. Saldin, Angle-resolved electron-energy-loss spectroscopy: atomic-core excitations at adsorbates on surfaces, Phys Rev. Lett. 60 (1988) 1197–1200.

[54] A. Ruocco, M. Milani, S. Nannarone, G. Stefani, Scattering mechanism of electrons interacting with surfaces in specular reflection geometry: Graphite, Phys. Rev. B 59 (1999) 13359–13364.

[55] S. Iacobucci, P. Letardi, M. MOntagnoli, P. Nataletti, G. Stefani, An angular resolved electron energy loss investigation of highly oriented pyrolithic graphite electronic structure, J. Electron Spectrosc. 67 (1994) 479–488.

[56] D. K. Schroder, Semiconductor Material and Device Characterization, John Wiley & Sons, Inc., 2005.

[57] S. E. Swirhun, R. M. Swanson, Temperature dependence of specific contact resistivity, IEEE Electron Device Lett. 7 (1986) 155–157.

[58] K. Tsugawa, K. Kitatani, H. Noda, A. Hokazono, K. Hirose, M. Tajima, H. Kawarada, High-preformance diamond surface-channel field-effect transistors and their operation mechanism, Dia. Relat. Mater. 8 (1999) 927 – 933.

[59] J. H. Moore, C. C. Davis, M. A. Coplan, Building Scientific Apparatus, Cambridge University Press, 2009.

[60] J. L. Wiza, Microchannel plate detectors, Nucl. Instrum. Methods 162 (1979) 587–601.

[61] V. S. Smentkowski, J. T. Yates, Jr., Purity of atomic oxygen production from heated iridium surfaces, J. Vac. Sci. Technol., A 12 (1994) 219–223.

[62] V. S. Smentkowski, J. T. Yates Jr., Characterization of heated platinum filaments as a source of atomic oxygen, J. Vac. Sci. Technol., A 12 (1994) 224–227.

[63] B. D. Thoms, J. E. Butler, HREELS and LEED of HC(100): the 2×1 monohydride dimer row reconstruction, Surf. Sci 328 (1995) 291–301.

[64] H. Kawarada, Hydrogen-terminated diamond surfaces and interfaces, Surf. Sci. Rep. 26 (1996) 205–259.

[65] Y. M. Wang, K. W. Wong, S. T. Lee, M. Nishitami-Gamo, I. Sakaguchi, K. P. Loh, T. Ando, Surface structure of C(100)-(2×1)-H studied by quantitative LEED analysis, Phys. Rev. B 59 (1999) 10347–10350.

[66] P. G. Lurie, J. M. Wilson, The diamond surface. I. the structure of the clean surface and the interaction with gases and metal, Surf. Sci. 65 (1977) 453–477.

[67] V. Polyakov, A. Rukovishnikov, B. Garin, L. Avdeeva, R. Heidinger, V. Parshin, V. Ralchenko, Electrically active defects, conductivity, and millimeter wave dielectric 4loss in cvd diamonds, Dia. Relat. Mater. 10 (2005) 604 – 607.

[68] G. Davies, S. C. Lawson, A. T. Collins, A. Mainwood, S. J. Sharp, Vacancy-related centers in diamond, Phys. Rev. B 46 (1992) 13157–13170.

[69] P. E. Pehrsson, T. W. Mercer, Thermal oxidation of the hydrogenated diamond (100) surface, Surf. Sci. 497 (2002) 13–28.

[70] Y. Fan, A. G. Fitzgerald, P. John, C. E. Troupe, J. I. B. Wilson, X-ray photoelectron spectroscopy studies of CVD diamond films, Surf. Interface Anal. 34 (2002) 703–707.

[71] G. Francz, P. Oelhafer, Photoelectron spectroscopy of the annealed and deuterium-exposed natural diamond (100) surface, Surf. Sci. 329 (1995) 193–198.

[72] S. Tanuma, C. J. Powell, D. R. Penn, Calculations of electron inelastic mean free paths. IX. data for 41 elemental solids over the 50 ev to 30 kev range, Surf. Interface Anal. 43 (2011) 689–713.

[73] S. Petrick, C. Benndorf, Potassium adsorption on hydrogen- and oxygen-terminated diamond(100) surfaces, Dia. Relat. Mater. 10 (2001) 519 – 525.

[74] F. Klauser, S. Ghodbane, R. Boukherroub, S. Szunerits, D. Steinmüller-Nethl, E. Bertel, N. Memmel, Comparison of different oxidation techniques on single-crystal and nanocrystalline diamond surfaces, Dia. Relat. Mater. 19 (2010) 474 – 478.

[75] K. M. O'Donnell, M. T. Edmonds, J. Ristein, A. Tadich, L. Thomsen, Q.-H. Wu, C. I. Pakes, L. Ley, Diamond surfaces with air-stable negative electron affi ity and giant electron yield enhancement, Adv. Funct. Mater 23 (2013) 5608–5614.

[76] H. Notsu, I. Yagi, T. Tatsuma, D. A. Tryk, A. Fujishima, Introduction of oxygen-containing functional groups onto diamond electrode surfaces by oxygen plasma and anodic polarization, Electrochem. and Solid-State Lett. 2 (1999) 522–524.

[77] S. D. Gardner, C. S. Singamsetty, G. L. Booth, G.-R. He, C. U. Pittman, Jr., Surface characterization of carbon fibers using angle-resolved XPS and ISS, Carbon 33.

[78] L. Stobinski, B. Lesiak, A. Malolepszy, M. Mazurkiewicz, B. Mierzwa, J. Zemek, P. Jiricek, I. Bieloshapk, Graphene oxide and reduced graphene oxide studied by the XRD, TEM and electron spectroscopy methods, J. Electron. Spectrosc. Relat. Phenom. 195 (2014) 145–154.

[79] M. Moisan, M. R. Wertheimer, Comparison of microwave and r.f. plasmas: fundamental and applications, Surf. Coat. Technol. 59 (1993) 1–13.

[80] J. C. Vickerman, I. S. Gilmore (Eds.), Surface Analysis - The Principal Techniques (II edition), Wiley, 2009.

[81] N. W. Makau, T. E. Derry, Study of oxygen on the three low index diamond surfaces by XPS, Surf. Rev. Lett. 10 (2003) 295–301.

[82] M. Kubovic, M. Kasu, H. Kageshima, F. Maeda, Electronic and surface properties of H-terminated diamond surface affected by NO_2 gas, Dia. Relat. Mater. 19 (2010) 889–893.

[83] C. E. Nebel, C. Sauerer, F. Ertl, M. Stutzmann, C. F. O. Graeff, P. Bergonzo, O. A. Williams, R. Jackman, Hydrogen-induced transport

properties of holes in diamond surface layers, Appl. Phys. Lett. 79 (2001) 4541–4543.

[84] S. Torrengo, R. Canteri, R. Dell'Anna, L. Minati, A. Pasquarelli, S. G., XPS and ToF-SIMS investigation of nanocrystalline diamond oxidized surfaces, Appl. Surf. Sci 276 (2013) 101 – 111.

[85] A. Plesanovas, A. Castellani Tarabini, I. Abbati, A. Kaciulis, G. Paolicelli, L. Pasquali, A. Ruocco, S. Nannarone, Valence band states of H:GaAs(110), Surf. Sci. 307-309 (1994) 890 – 895.